UNIVERSITY OF CALIFORNIA SAN DIEGO

Flat Composite Panel Impact Testing and Characterization by Ultrasonic Non-Destructive Evaluation

A Thesis submitted in partial satisfaction of the requirements
for the degree Master of Science

in

Structural Engineering

by

Barrett W. Romasko

Committee in charge:

Professor Hyonny Kim, Chair
Professor Ken Loh
Professor Machel Morrison

2022

The Thesis of Barrett W. Romasko is approved, and it is acceptable in quality and form for publication on microfilm and electronically.

University of California San Diego

2022

TABLE OF CONTENTS

THESIS APPROVAL PAGE iii

TABLE OF CONTENTS iv

LIST OF FIGURES vi

LIST OF TABLES ix

LIST OF ABBREVIATIONS x

ACKNOWLEDGEMENTS xi

ABSTRACT OF THE THESIS xii

CHAPTER 1: INTRODUCTION 1

1.1 SCOPE 1
1.2 MOTIVATION 1
1.3 LITERATURE REVIEW 2
1.3.1 Low Velocity Impact Damage on Composite Laminates 2
1.3.2 Ultrasound Measurement of Impact Damage 3

CHAPTER 2: EXPERIMENTAL SETUP 7

2.1 PENDULUM IMPACT SYSTEM SET-UP 7
2.2 MATERIAL PROPERTIES AND SPECIMEN CUT-OUT PROCEDURE 9
2.3 EXPERIMENTAL PROCEDURE 13
2.3.1 Energy Level Range Preliminary Tests 13
2.3.2 Ultrasonic Non-Destructive Evaluation Methods 16

CHAPTER 3: RESULTS AND DISCUSSION 28

3.1 IMPACT EVENT 28
3.1.1 Force Versus Time Plot Error 38
3.2 NON-DESTRUCTIVE EVALUATION RESULTS 42
3.3 SHADOW DELAMINATION INVESTIGATION – BACKSIDE SCAN COMPARISON 52

CHAPTER 4: CONCLUSION AND FUTURE WORKS 56

4.1 FUTURE WORKS 57

REFERENCES 59

APPENDIX I: PENDULUM IMPACTOR PROCEDURE 61

APPENDIX II: ULTRASONIC SCANNING PROCEDURE 65

APPENDIX III: CALCULATIONS FROM IMPACT EVENT DATA 69

APPENDIX IV: FORCE AND C-SCAN DATA 73

LIST OF FIGURES

Figure 2.1: Schematic Drawing of Pendulum Impactor Constraints, all dimensions in mm.... 8

Figure 2.2: Pendulum Impactor System Set-up..... 9

Figure 2.3: Manufactured IM7/977-3 Panel..... 11

Figure 2.4: Test Specimen Cut to 100 mm by 150 mm Nominal Size..... 12

Figure 2.5: Preliminary Impact Damage Size (via A-Scan) for Range of Energy (10 J top, 20 J middle, 40 J bottom)..... 14

Figure 2.6: Impact Damage Size (via A-Scan) for Range of Energy (10- 40 J, left to right)... 15

Figure 2.7: Reference Waveform from A-scan, the gate alerts the user (and the software) if there is a significant (>50%) signal return earlier than the reference return peak. If a reflection returns within the orange boxed area, then this is a location of damage..... 17

Figure 2.8: Hand-mapped A-scan of a 20 J Hard Laminate Impact Specimen. The red dots indicate the location where the A-scan found a delamination perimeter zone. Lines were drawn to connect the dots once enough dots had been placed for the delamination shape to be properly shown..... 18

Figure 2.9: C-scan Immersion Tank Setup with Specimen in Place..... 19

Figure 2.10: Specimen Used for Scan Resolution and Speed Tests (10 J impact, Medium Laminate, A-scanned)..... 21

Figure 2.11: C-Scan Resolution and Speed Test 1 (1 mm by 1 mm Resolution, 25 mm/s Speed)..... 21

Figure 2.12: C-Scan Resolution and Speed Test 2 (0.5 mm by 0.5 mm Resolution, 25 mm/s Speed)..... 22

Figure 2.13: C-Scan Resolution and Speed Test 3 (0.25 mm by 0.25 mm Resolution, 25 mm/s Speed)..... 22

Figure 2.14: C-Scan Resolution and Speed Test 4 (0.25 mm by 0.25 mm Resolution, 15 mm/s Speed)..... 23

Figure 2.15: C-Scan Resolution and Speed Test 5 (0.25 mm by 0.25 mm Resolution, 50 mm/s Speed)..... 23

Figure 2.16: C-Scan Resolution and Speed Test 6 (0.2 mm by 0.2 mm Resolution, 50

mm/s Speed)..... 24

Figure 2.17: C-Scan Image of a 20 J Impacted Hard Laminate..... 27

Figure 3.1: Location of Damage Initiation Force and Peak Impact Force Magnitude..... 29

Figure 3.2: Impact Force Versus Time for 10 J Impacts for all Panel Types 30

Figure 3.3: Impact Force Versus Time for 15 J Impacts for all Panel Types..... 30

Figure 3.4: Impact Force Versus Time for 20 J Impacts for all Panel Types..... 31

Figure 3.5: Impact Force Versus Time for Panel H Impacts (10 J, 15 J, and 20 J Impacts).... 31

Figure 3.6: Impact Force Versus Time for Panel M Impacts (10 J, 15 J, and 20 J Impacts).... 32

Figure 3.7: Impact Force Versus Time for Panel S Impacts (10 J, 15 J, and 20 J Impacts)..... 32

Figure 3.8: Damage Initiation Force Versus Impact Energy Level for all Specimens..... 34

Figure 3.9: Delamination Size Versus Impact Energy Level for all Specimens..... 36

Figure 3.10: Normalized Energy Absorption Versus Impact Energy Level for all Specimens..... 37

Figure 3.11: Peak Impact Force versus Impact Energy Level for all Specimens..... 38

Figure 3.12: CSAI-BL-H-15J-1 Inaccurate Data Collection Plot with Reference Curve..... 39

Figure 3.13: CSAI-BL-H-15J-2 Inaccurate Data Collection Plot with Reference Curve..... 39

Figure 3.14: CSAI-BL-H-15J-3 Inaccurate Data Collection Plot with Reference Curve..... 40

Figure 3.15: CSAI-RPR-H-15J-1 Inaccurate Data Collection Plot with Reference Curve..... 40

Figure 3.16: CSAI-RPR-H-15J-2 Inaccurate Data Collection Plot with Reference Curve..... 41

Figure 3.17: CSAI-RPR-H-15J-3 Inaccurate Data Collection Plot with Reference Curve..... 41

Figure 3.18: A-Scan and C-Scan Images of a 10 J Panel H Specimen..... 43

Figure 3.19: A-Scan and C-Scan Images of a 10 J Panel M Specimen..... 44

Figure 3.20: A-Scan and C-Scan Images of a 10 J Panel S Specimen..... 45

Figure 3.21: A-Scan and C-Scan Images of a 15 J Panel H Specimen..... 46

Figure 3.22: A-Scan and C-Scan Images of a 15 J Panel M Specimen..... 47

Figure 3.23: A-Scan and C-Scan Images of a 15 J Panel S Specimen..... 48

Figure 3.24: A-Scan and C-Scan Images of a 20 J Panel H Specimen.....49

Figure 3.25 A-Scan and C-Scan Images of a 20 J Panel M Specimen..... 50

Figure 3.26: A-Scan and C-Scan Images of a 20 J Panel S Specimen..... 51

Figure 3.27: Front and Backside C-Scan Images of a 10 J Panel S Specimen..... 53

Figure 3.28: Front and Backside C-Scan Images of a 15 J Panel S Specimen..... 54

Figure 3.29: Front and Backside C-Scan Images of a 20 J Panel S Specimen..... 55

Figure 4.1: CSAI Testing of Unrepaired Panel M 15J Specimen Showing DIC Strain Contour..... 58
.

LIST OF TABLES

Table 2.1: IM7/977-3 Carbon/Epoxy Composite Panel Properties..... 10

Table 2.2: C-Scan Resolution Investigation Scan Time per Resolution and Speed Pairing... 20

LIST OF ABBREVIATIONS

CFRP	Carbon Fiber Reinforced Polymer
CSAI	Compressive Strength After Impact
DAQ	Data Acquisition
DIC	Digital Image Correlation
FAA	Federal Aviation Administration
FRCSW	Fleet Readiness Center Southwest
ILSS	Interlaminate Shear Strength
NDE	Non-Destructive Evaluation
TOF	Time of Flight

ACKNOWLEDGEMENTS

I would like to thank my thesis advisor, Professor Hyonny Kim, for allowing me to perform research in his lab group. His assistance with issues and questions I developed throughout my research was extremely helpful. I would also like to thank him for the care and passion he put into the multiple classes he taught, they were not only taught incredibly well, but in a way that inspired me and other students to pursue aerospace structural engineering for future careers.

I would also like to thank Justin Massey for allowing me to join his research team to assist with a portion of his dissertation project for my thesis. His assistance with aspects of my research, as well as his career advice and friendship, have been very supportive throughout the duration of my masters.

Thank you to the other members of Professor Hyonny Kim's lab group, they have helped me with conceptual and experimental questions and problems. A special thank you to Eric Kim for teaching me how to perform A and C-scanning methods, as well as to Konstantinos Anagnostopoulos for teaching me how to perform impact studies with the pendulum impact system as well as how to cut composite panels.

Thank you to Professor Ken Loh and Professor Machel Morrison for their willingness to be a part of my thesis defense committee.

Finally, thank you to my family and my friends for their support and encouragement throughout this thesis, as well as throughout my entire time at the University of California, San Diego.

ABSTRACT OF THE THESIS

Flat Composite Panel Impact Testing and Characterization by Ultrasonic Non-Destructive Evaluation

by

Barrett W. Romasko

Master of Science in Structural Engineering

University of California San Diego, 2022

Professor Hyonny Kim, Chair

Low velocity impact damage to laminated composite structures can cause a range of damage modes. Of interest is small damage composed of delamination (i.e. separation of plies) that is less than 50 mm in size, with barely visible impact-side damage. Formation of actual impact-induced damage, mainly multiple planes of delamination that are interconnected via matrix cracks, is the main goal of this study, which supports a larger project where injection repair of the damage is being investigated. Three 25-ply composite panel types having varying percentages of 0° fiber content have been low velocity impacted at 10, 15, and

20 Joule energy levels. 81 total impact studies were performed using a pendulum impact system with the composite panels clamped on all edges. Multiplanar internal delamination regions with barely visible impact damage on the impacted surface were created. In addition to measuring the force history during the impacts event, the internal damage is investigated and characterized using ultrasonic pulse-echo scanning methods. The perimeter of damaged regions is determined using gel-coupled hand-mapped A-scan methods, while an extensive investigation of the multiple planes of delamination damage is investigated using C-scanning methods where the specimen is immersed in de-ionized water. Results show that the panel type with the least amount of 0° plies has the largest internal delamination damage, but this panel type also requires the highest impact force for damage to occur. In addition to impact-side C-scans, nine specimens are back side C-scanned to investigate the pulse-echo shadowing effect which commonly hides lower-depth delaminations.

CHAPTER 1: INTRODUCTION

1.1 Scope

The scope of this research is to create barely visible impact damage (BVID) on composite laminates that are commonly used in aircraft structures. The goal is to obtain a dataset of damaged carbon fiber reinforced polymer (CFRP) panels that have internal delamination damage for specific laminate configurations of interest, with a maximum overall damage size of 50 mm or less. These damaged panels are then investigated further using Non-destructive evaluation (NDE) to better understand the damage profile created by the low velocity impact events that the panels are subjected to. The dataset created from this thesis will be used in a future project to determine a novel procedure that provides a strength restoring injection repair for composite aircraft.

1.2 Motivation

This thesis will investigate a series of impact events on specimens comprised of three differing 25-ply composite panels, each of which varying in the percent of 0° plies they are comprised of. Following the damage creation, ultrasonic A-scan and C-scan methods will be employed to understand the internal damage in the impacted specimens. The motivation behind these tests are to create and investigate damage for subsequent further work. This further work is being completed by a separate researcher and involves novel injection repair procedures for repairing delamination regions. The intent is to restore laminate strength for IM7/977-3 composite material.

1.3 Literature Review

1.3.1 Low Velocity Impact Damage on Composite Laminates

Carbon Fiber Reinforced Polymer (CFRP) laminates have garnered increased use in aerospace applications due to their high strength to weight ratio, as well as high stiffness to weight ratios. However, these materials are often very brittle and are susceptible to internal damage [1]. A major concern with composite structures is their vulnerability to BVID. Composite laminates can succumb to BVID through tool drops during maintenance, hail stone impacts on the runway, and more. The internal damage created from these impacts can grow during service, which can eventually cause a catastrophic failure if not caught [2]. The specifications for what is considered BVID differs from manufacturer to manufacturer, and agency to agency. However, the main characteristic of BVID is that it is damage that has low visibility on the surface of a composite, but internal damage and back side damage is prevalent. In most cases of BVID, there is a small dent on the impacted surface of the laminate, this dent is usually between 0.25-0.50 mm [3].

Small surface indentations that are considered BVID can be created through low velocity impacts. A low velocity impact is defined as an impact with a velocity in the range of 1 to 10 m/s [4]. These impact events result in the entire structure responding to the loading due to the contact period being long enough. Thus, the structure is in danger of damage modes ranging from matrix cracking, delamination, fiber failure, and penetration [4]. In low velocity impacts, delamination paired with matrix cracking has been attributed as the major damage mode in composite structures [5]. Delamination and matrix cracking differ in one major way, matrix cracking, along with fiber breakage, are failures within a single ply of the laminate, while a delamination is a failure between the interface of two plies [5]. Delamination damage is the most critical failure

mode in CFRP laminates due to unstable crack growth formation that can lead to catastrophic failure due to weakening the other failure modes that a composite structure has [6]. Therefore, this thesis focuses on delamination damage, which is defined as a crack that runs in the resin rich area between plies of different fiber orientation [4].

The Federal Aviation Administration (FAA) requires that all composite parts with BVID must survive the ultimate load of the structures loading scenario [7]. Due to this requirement, it is important to understand how delamination damage forms under certain impact conditions. In a series of tests to study the relationship of impact damage to panel size and boundary conditions, NASA researchers Jackson and Poe concluded that as panel size increases, the peak contact force decreases, similarly, simply supported constraints had a lower impact force than clamped constraints [7]. From these studies, it is found that a smaller plate with clamped conditions is the worst-case scenario for BVID damage to occur. A separate test, performed by Liu, consisted of clamping the four edges of a glass/epoxy laminate and was impacted by a blunt cylinder shot out of an air gun. From these impact studies, Liu found that there is a relationship between delamination damage and matrix cracks, the larger the delamination, the larger the matrix crack [5].

1.3.2 Ultrasound Measurement of Impact Damage

The main reason that low velocity impact damage is so dangerous is the ability for the damage to go undetected. Since most low velocity impacts leave BVID, there's a chance that the damage is never noticed before an aircraft is flown again, which could lead to catastrophe. The issue is that there can be a substantial decrease in residual strength properties from impacts at velocities lower than where visible damage is created [8]. In order to reduce the risk of structural failure due to BVID, Non-destructive evaluation (NDE) methods have been implemented to

inspect for internal damage in high-risk regions. A commonly used form of NDE, and the form used in this thesis, is the use of ultrasound measurement of impact damage. There are two conventional methods of ultrasonic testing that are used heavily in damage investigation, pulse-echo and through-transmission techniques. Pulse-echo is also referred to as the reflection method and consists of utilizing a single transducer for transmitting and receiving the ultrasonic wave [9]. When a transmitted ultrasonic wave encounters a damage interface, the amplitude of the reflected energy is distinct from a pristine reflection from the back surface of the scanned laminate. An issue with the pulse-echo method of determining damage on layer-by-layer level is that the results can have superimposed defects due to range resolution issues, these can cause the scans to have poor resolution and can cause confusion to the investigator [9]. In order to mitigate these issues, the time of flight (TOF) scan method has been utilized with pulse-echo scans to allow delamination or crack damage to be determined with improved accuracy [9]. The method of determining the depth of damage in a laminate is determined using Equation (1):

$$d = \frac{c * TOF}{2} \tag{1}$$

where d refers to the depth of the damage, and c refers to the sound velocity [9]. The product of the time of flight and the sound velocity are divided by two due to the transmission travelling through the thickness of the laminate twice due to the ultrasonic wave reflecting off of the back surface (or damage interface) before returning to the transducer.

Through-transmission ultrasonic scanning differs from pulse-echo ultrasonic scanning due to through-transmission scans employing the use of two transducers instead of one. This allows one transducer to send out the ultrasonic wave while the second transducer catches the wave, this is referred to as “pitch-catch” [9]. This method allows for the wave attenuation to be less than what is found in pulse-echo transmission due to the wave only travelling one direction,

allowing through transmission to be more useful on thicker composite laminates. However, a significant issue with through transmission scanning is the requirement for the backside of the laminate to be accessible. In most aerospace structures, the backside of laminates is not accessible. This limits the use of through-transmission in most on-site inspections in the aerospace industry [9]. Due to this limitation, this thesis employs the use of the pulse-echo scanning method.

There are three methods of utilizing pulse-echo ultrasonic testing, they are A, B, and C-scans. A-scans refer to a 1-D waveform scanning through a single point in a laminate. This scan requires the use of a couplant material (in the case of this thesis it was gel) to ensure that there was good contact between the transducer and the top surface of the panel [10]. B-scans are a series of A-scans taken in a line. The result is a cross sectional view of the scanned laminate in the location where the line was taken [10]. This allows for damage to be seen as if the laminate was cut on that line, allowing multiple planes of delamination to be seen. Finally, C-scans represent the entire top surface of the scan surface. Usually, the transducer is a set distance from the surface and the panel and transducer are immersed in a tank of liquid, such as de-ionized water [10]. A piezoelectric transducer is driven by a high-voltage pulse to send out an ultrasonic wave. The return signal amplitude data is then collected and digitally plotted on a 2-D grid while a raster scan (or rectangular scanning path) is employed across the scanning surface [11]. The resulting scan is a 2-D contour plot that covers the entire scanned surface. The damage interfaces are plotted on this scan with a color index so that the depth of the damage can be interpreted in reference to the total thickness of the scanned item. In this thesis, A-scan and C-scan techniques were utilized to inspect damaged regions in impact damaged composite specimens.

A limitation of ultrasonic testing is the shadow effect. This refers to the delaminations that occur closer to the backside of the scanned specimen are obscured by the delaminations that are closer to the scanned surface [12]. This effect creates the necessity to scan from both sides to properly characterize the full damage extent. However, as discussed previously, it is difficult to scan the backside of composites in many aerospace structures.

CHAPTER 2: EXPERIMENTAL SETUP

2.1 Pendulum Impact System Set-up

In order to investigate the delamination damage in the carbon fiber panels, impact tests were conducted on a multitude of specimens with a varying range of impact energy. The impact events were conducted using a pendulum impactor system following a modified ASTM D7136 standard [13]. The drop weight impactor from ASTM D7136 was replaced by the pendulum impactor system to allow for lower energy impacts with a lower probability of the weight bouncing back onto the specimen and a second impact event occurring.

The impact setup, as shown in Figure 1.1, included a tip mass of 4.6 kg and an arm mass of 0.7 kg. The arm length was 1.4 m and consisted of a stiff, hollow, fiberglass rod with a square cross-section that was further stiffened with an aluminum bar with a L-shaped cross-section. The tip of the impactor was made out of hardened steel and had a 25.4 mm diameter spherical tip with a force sensor (Dytran 1050V6) attached to it. As the pendulum arm and tip mass swings, it passes through a laser photogate to record the time history of the impact event, after the impact, the arm and tip mass bounce back through the laser photogate again. The photogate data was used to calculate the incoming velocity, as well as the outgoing (rebounding) velocity in order to determine the incoming impact energy and the energy lost in the impact event. The force sensor data was used to determine the peak force in the impact event, as well as to plot the force versus time history of the impact event in order to visualize the region where the damage starts to occur in the specimen. Both the time and force history data acquisition was performed using a Picoscope Model 3424 oscilloscope data acquisition system and software.

For each impact study, the specimen was clamped to the pendulum impactor frame along all edges using two 12 mm thick A36 steel fixture plates. The steel plates each had a 128 x 77

mm window to allow the pendulum tip to impact the center of the specimen and allow deflection on the backside of the specimen. The plates were clamped together using a 5/16-18 UNC bolt in each corner, with the carbon fiber specimen in between the two plates. Figure 2.1 shows a detailed schematic of the constraints for the pendulum impact events.

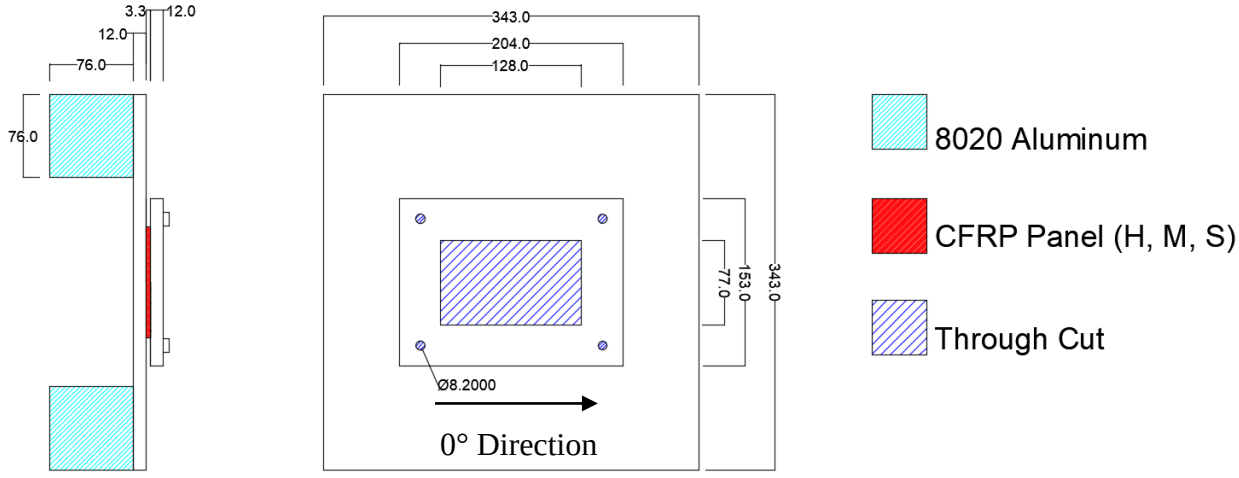

Figure 2.1: Schematic Drawing of Pendulum Impactor Constraints, all dimensions in mm

To conduct an impact test, the tip mass is raised by setting the angle of the arm to a specified angle depending on the impact energy desired for the experiment. The arm was able to be set at differing angles due to a cable being attached to the end of the pendulum arm with a pneumatic latching release system. The cable is attached to a winch that allows the arm to be raised or lowered by the user. The angle of the arm is able to be consistently set using a digital readout from a US Digital A-2 absolute encoder wheel that is located at the arms pivot. This encoder wheel has 3600 incremented steps which allows the angle of the arm to be set up to a tenth of a degree. When the user sets the arm set to a desired angle, the arm could be released by pressing a button that released the pneumatic latching system which cleanly releases the

impacting mass. The fixture plates, as well as the laser photogate, pendulum tip mass, and the end of the pendulum arm can be seen in Figure 2.2.

Figure 2.2: Pendulum Impactor System Set-up

2.2 Material Properties and Specimen Cut-out Procedure

The specimens that were impacted by the pendulum impactor system consisted of carbon fiber panels with three different ply layups. The three panels consisted of the layups shown in Table 2.1. The panels were each manufactured by NAVAIR Fleet Readiness Center Southwest (FRCSW) using unidirectional plies of IM7/977-3 pre-impregnated carbon fiber/epoxy and cured in an autoclave. Each panel consists of 25 plies stacked in orientations that give differing stiffness characteristics, the three panel types are consistent with layups commonly used in Naval

aircraft. The panels were named in order from stiffest to most compliant: panels H, M, and S (standing for Hard, Medium, and Soft). A manufactured panel before being cut into specimens can be seen in Figure 2.3.

Table 2.1: IM7/977-3 Carbon/Epoxy Composite Panel Properties

Panel Type	Layup	Effective Modulus (GPa)	Overall Dimensions (mm)		
			Width	Length	Avg. Thickness
H	$[45/-45/0/0/45/-45/0/0/45/-45/0/0/\underline{90}]_S$	114	610	711	3.3
M	$[45/-45/0/0/45/-45/0/45/-45/0/45/-45/\underline{90}]_s$	79.2	610	711	3.3
S	$[45/-45/0/45/-45/90/45/-45/0/45/-45/90/\underline{90}]_s$	58.6	610	711	3.3

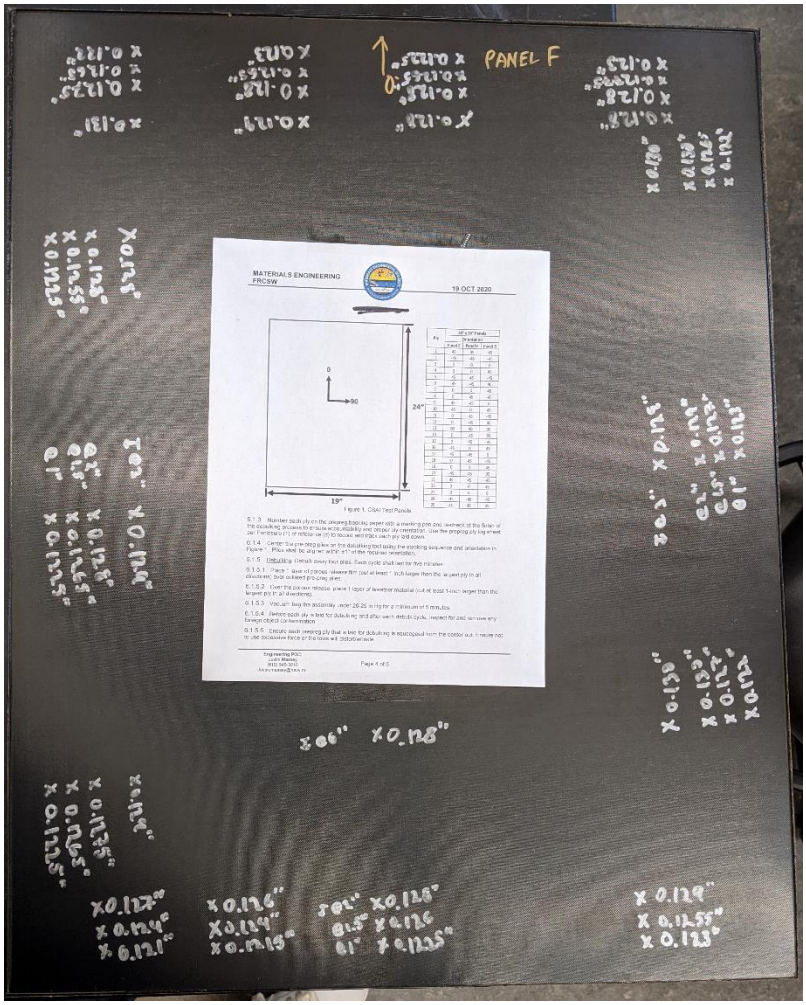

Figure 2.3: Manufactured IM7/977-3 Panel.

Each of the panel types were machined into specimens with nominal dimensions of 100 mm by 150 mm with the 0° direction aligned with the long side of the specimens. These specimens were cut out of the panels with a wet diamond blade tile saw. The specimen size was determined according to the ASTM D7136 [1] test method, examples of cut out specimens can be seen in Figure 2.4.

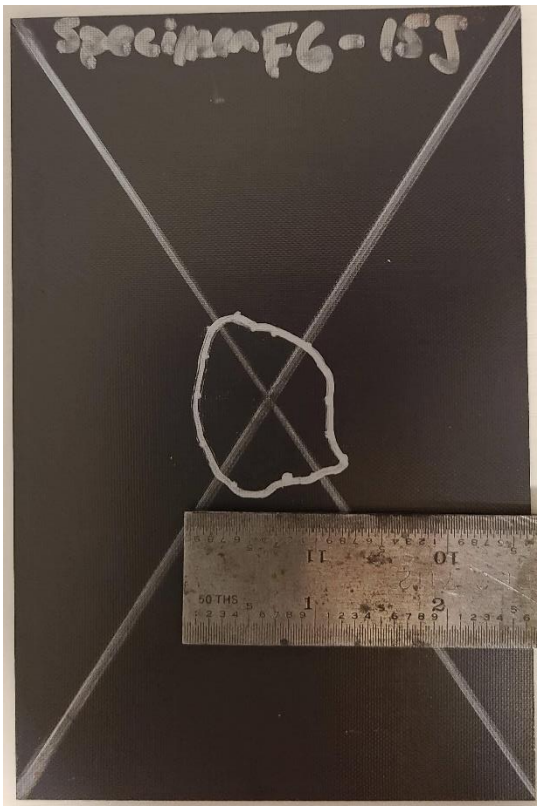

Figure 2.4: Test Specimen Cut to 100 mm by 150 mm Nominal Size.

For this project, 81 specimens were created and damaged using the pendulum impactor. The specimens were grouped using three separate categories: panel type, condition, and impact energy level. The panel type refers to the H, M, and S panel names as discussed previously. The condition category refers to the process that will be taken regarding the specimen when it comes to the repair process that is outside of the scope of this paper. However, since the specimens in this paper follow that naming convention, an explanation of what they represent is needed. The three condition categories are: BL (baseline, unrepaired), RPR (surface prepped and repaired), and CONT (contaminated, surface prepped, and repaired). The repair and contamination of the specimens is a future work project that is not a part of this thesis. The next category is the impact energy, which will be discussed in the next section as the impact energy that was considered for this project had to be narrowed down to a select range. Finally, the last naming convention

category is the specimen number within each of the previous three category pairings, there are three specimens per pairing of panel type, condition, and energy level. From these four categories, the naming convention for all specimens was determined in a way that can be seen in the following formula.

CSAI-**A**-**B**-**C**-**D**, where

A: BL, RPR, or CONT condition

B: H, M, or S panel type

C: Impact Energy Level (in Joules)

D: Specimen number (1-3)

Example: CSAI-BL-H-10J-1

2.3 Experimental Procedure

2.3.1 Energy Level Range Preliminary Tests

Once the specimens have been cut out from their respective panels, two diagonal lines are drawn from one corner to the opposite corner of the specimen to create an X (see Figure 2.4). This allows the researcher to locate the center of the specimen in order to impact the specimen directly at the center. The specimen to be impacted is then inserted into the frame and the bolts are tightened with a wrench (no torque value set, just until the bolts were tightened as tight as they could be) once the impactor tip has been lined up with the center of the specimen. Before the 81 impact tests were conducted, an energy range needed to be determined that created delamination zones that were between 6 to 50 mm in diameter. It was determined to conduct five initial impact tests on the hard laminate (H) to determine the size of delaminations that were

created due to the energy level of the impacts. Of the five tests, one impact was conducted at 10 J, two were conducted at 20 J, and two were conducted at 40 J. This provided a 10-40 J range to investigate the energy level range to pursue for the entirety of the project. The specimens from each of these preliminary energy level impacts can be seen in Figure 2.5 after having the damage perimeter of the delamination hand-mapped using ultrasonic A-scan methods.

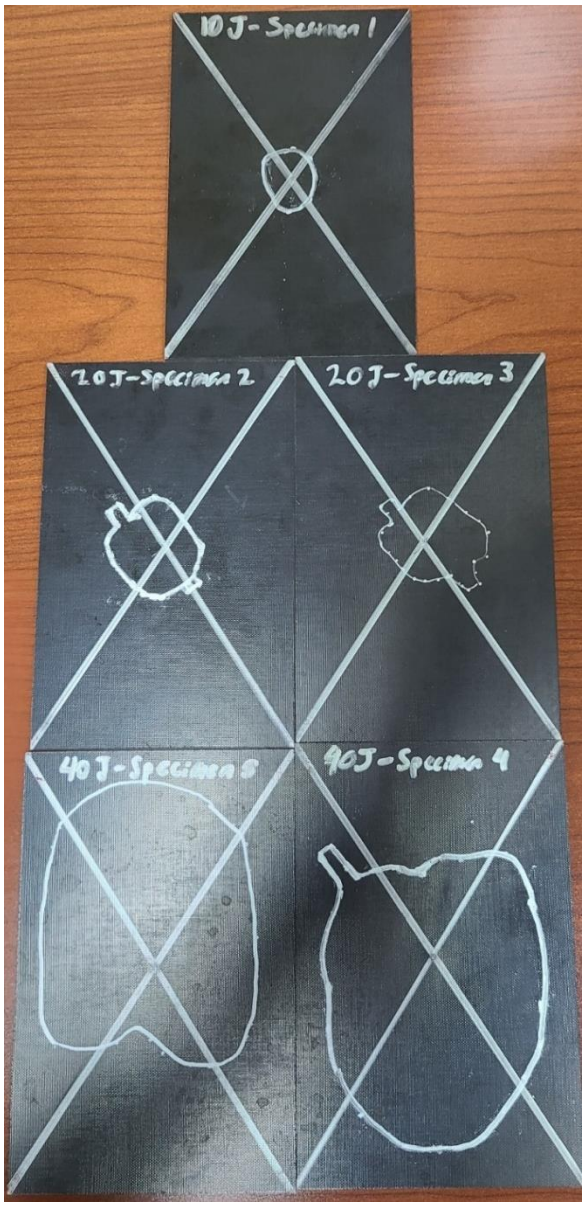

Figure 2.5: Preliminary Impact Damage Size (via A-Scan) for Range of Energy (10 J top, 20 J middle, 40 J bottom).

From the damage profiles shown in Figure 2.5, it is seen that the 40 J impacts greatly exceed the 50 mm diameter maximum damage threshold. However, the 10 J and 20 J impacts had delamination zones within the specified damage threshold, with 20 J nearing the 50 mm maximum desired damage size. From these preliminary impact level studies, it was determined that the 81 impacts that were to be conducted for the damage creation and investigation study needed to be impacted in a 10-20 J energy range. Therefore, a third impact energy level was added in between the minimum (10 J) and maximum (20 J) impact energy levels, this third impact energy was chosen to be 15 J. Figure 2.6 shows a progressive increase in damage size as the energy level is increased from 10 J, 15 J, 20 J, and 40 J.

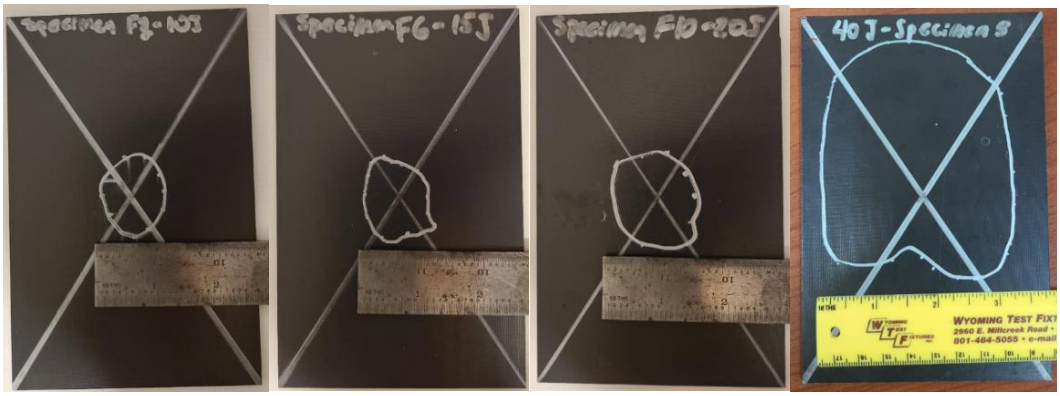

Figure 2.6: Impact Damage Size (via A-Scan) for Range of Energy (10- 40 J, left to right).

Once the desired impact range was determined, 27 specimens per material type were machined as defined in Section 2.2. For each material type, 9 specimens were impacted at each of the three energy levels to be further studied. The impacts took place following the guidelines outlined in Section 2.1 using the Pendulum impact system.

2.3.2 Ultrasonic Non-Destructive Evaluation Methods

Once a specimen had been impacted, the extent of the internal damage would be investigated using hand-mapped ultrasonic A-scan methods. This was used in order to allow the researchers to know the extent of the damage on a physical specimen, which would be useful for future studies using these specimens in terms of repair methods to be tested on them. The Non-destructive Inspection of the damaged specimens was performed using ultrasonic pulse-echo methods to map the location of delamination boundaries using hand-held A-scan with couplant gel. The hand-held 3.5 MHz transducer (NDTA CMD3-1) was used with a NDT Automation PocketUT device to give a real time visual of the waveform as the transducer was sending pulses into the specimen at different locations. By moving the transducer to different spots around the outer edges of the specimen at locations known to have no damage (i.e. baseline regions), and then sliding the transducer on the gel couplant towards the epicenter of the impact, the researcher could detect where the perimeter of damage is located. A reference waveform was used to assist in finding these damaged zones, this consisted of a pristine region having its waveform captured in the interface of the PocketUT system, and then that waveform was saved as a reference waveform, allowing the user to see the pristine regions return signal while scanning other regions of the specimen. In Figure 2.7 a reference A-scan waveform can be seen. The method for determining regions of delamination perimeters used in this project required the reference return signal from a pristine region to have a 50% decrease in amplitude while there was a 50% increase in amplitude of a return signal at an earlier TOF than the reference return signal.

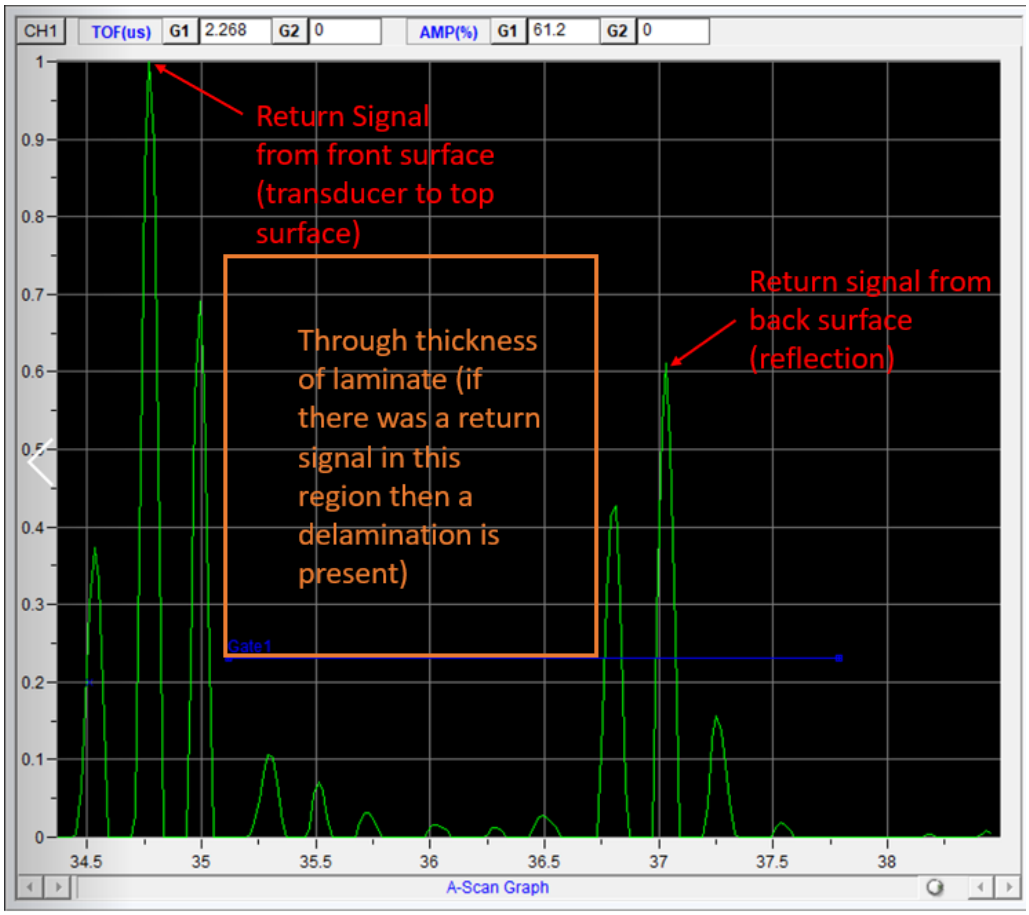

Figure 2.7: Reference Waveform from A-scan, the gate alerts the user (and the software) if there is a significant (>50%) signal return earlier than the reference return peak. If a reflection returns within the orange boxed area and has an amplitude greater than 50% of the pristine region reflection, then this is a location of damage.

The ability to detect the damage perimeter was due to the signal from the transducer returning at an earlier time of flight (TOF) than in the reference waveform. The user would mark the point on the specimen where this damage perimeter was observed and then shift to a different section of the specimen to characterize the shape of the damage. Once enough damage perimeter dots had been marked onto a single specimen to properly identify the overall shape of the delamination zone, the dots were connected. Figure 2.8 shows an example of a specimen that had been A-scanned with the method described. The in depth A-scan procedure can be found in the Appendix II.

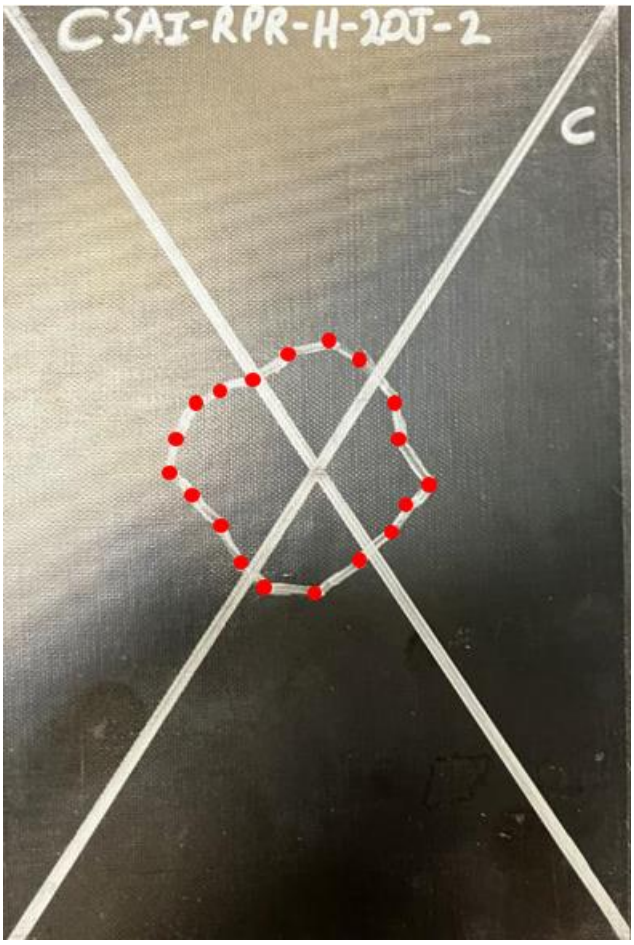

Figure 2.8: Hand-mapped A-scan of a 20 J Hard Laminate Impact Specimen. The red dots indicate the location where the A-scan found a delamination perimeter zone. Lines were drawn to connect the dots once enough dots had been placed for the delamination shape to be properly shown.

Following the A-scan procedure, the specimens were further investigated to get a graphical representation of the delamination through the depth of the laminate. This investigation was carried out using ultrasonic pulse-echo C-scans with a 5 MHz transducer (NDT Systems IAHG052) in a de-ionized water immersion tank. C-scans utilize multiple A-scans at a set resolution and then plots the return signal depth over the are scanned to graphically represent the specimens scan surface while showing a contour image where the depths of damage regions can be used to garner greater understanding of the damage created from the low velocity impacts that

the specimens underwent. Each specimen was placed on 200 mm long stainless-steel standoffs to keep it off of the bottom of the tank. The transducer was placed 25 mm from the top surface of the specimen and was manipulated by a mechanical arm that allowed the arm to translate along the length and width of the panel using a Mistras/NDT Automation 1682 control box that plugged into the PocketUT system. By C-scanning the specimens the extent of the damage would be more accurately investigated and the depths of the delaminated plies could be mapped via contour plot. An image showing the immersion tank that the C-scans were taken inside of can be seen in Figure 2.9.

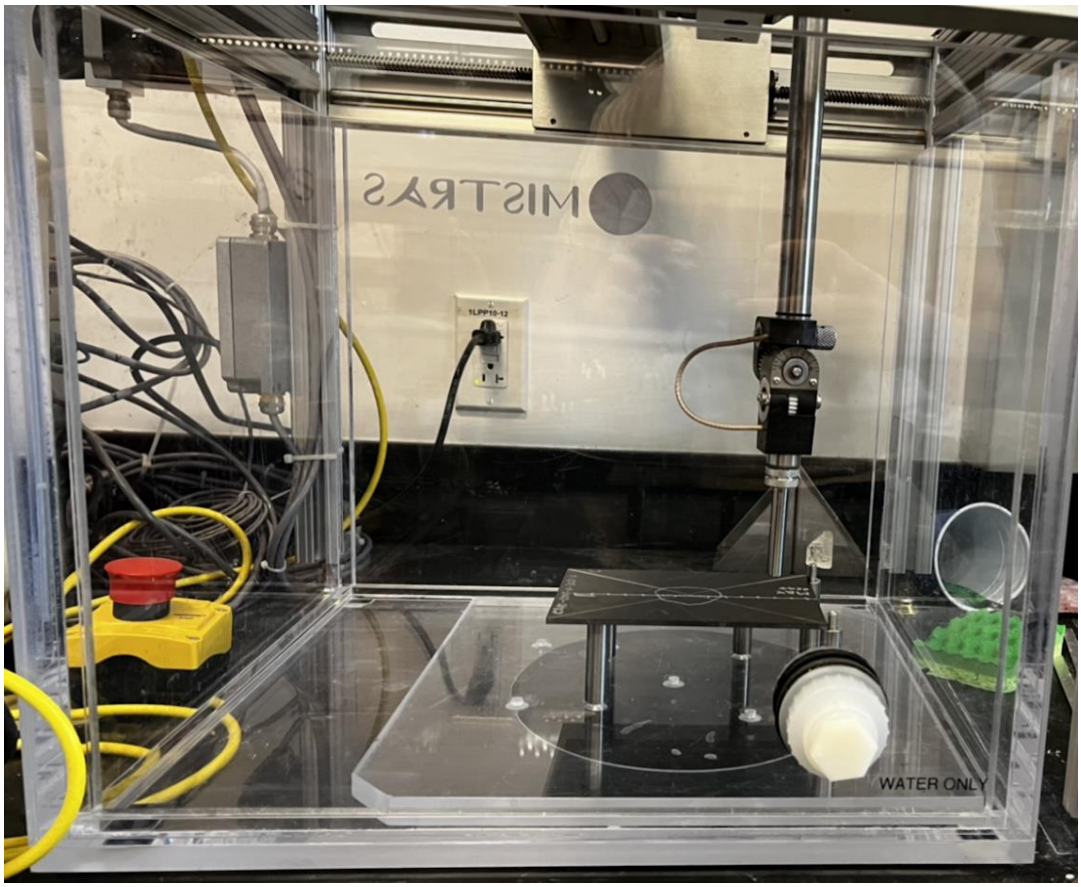

Figure 2.9: C-scan Immersion Tank Setup with Specimen in Place.

Before all of the specimens could be C-scanned, a resolution study was needed to determine how many A-scans were wanted in order to properly capture the damage. Resolution and scan speed needed to be determined so that the best scan quality to scan time pairing could be achieved. A series of six tests were conducted with scan resolutions varying from 1 x 1 mm to 0.2 x 0.2 mm, similarly, the scan speed in these six tests varied from 15 mm/s up to 50 mm/s. For all six test scans the same specimen was scanned (shown in Figure 2.6). For purposes of these resolution tests, a smaller region was scanned in order to save time, instead of the entire specimen area which includes mostly undamaged regions. The scan resolution, scan speed, and scan time for each of the six tests are shown in Table 2.2. The scan images for tests 1 through 6 can be seen in Figures 2.10 through 2.16, respectively.

Table 2.2: C-Scan Resolution Investigation Scan Time per Resolution and Speed Pairing.

Test Number	Scan Resolution (mm)	Scan Speed (mm/s)	Scan Time (min:sec)
1	1 x 1	25	5:00
2	0.5 x 0.5	25	8:40
3	0.25 x 0.25	25	17:13
4	0.25 x 0.25	15	30:00
5	0.25 x 0.25	50	8:20
6	0.2 x 0.2	50	9:58

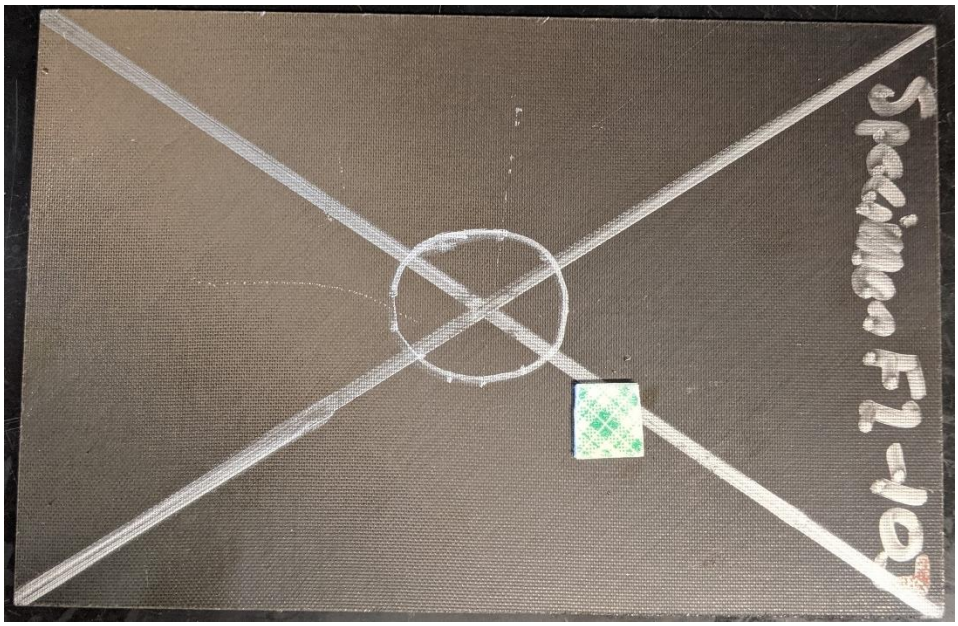

Figure 2.10: Specimen Used for Scan Resolution and Speed Tests (10 J impact, Medium Laminate, A-scanned).

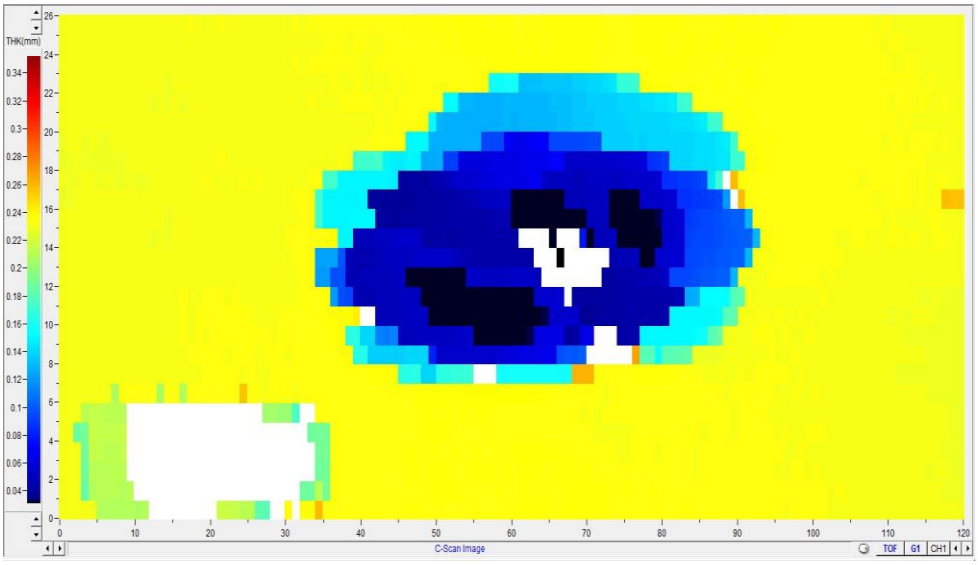

Figure 2.11: C-Scan Resolution and Speed Test 1 (1 mm by 1 mm Resolution, 25 mm/s Speed).

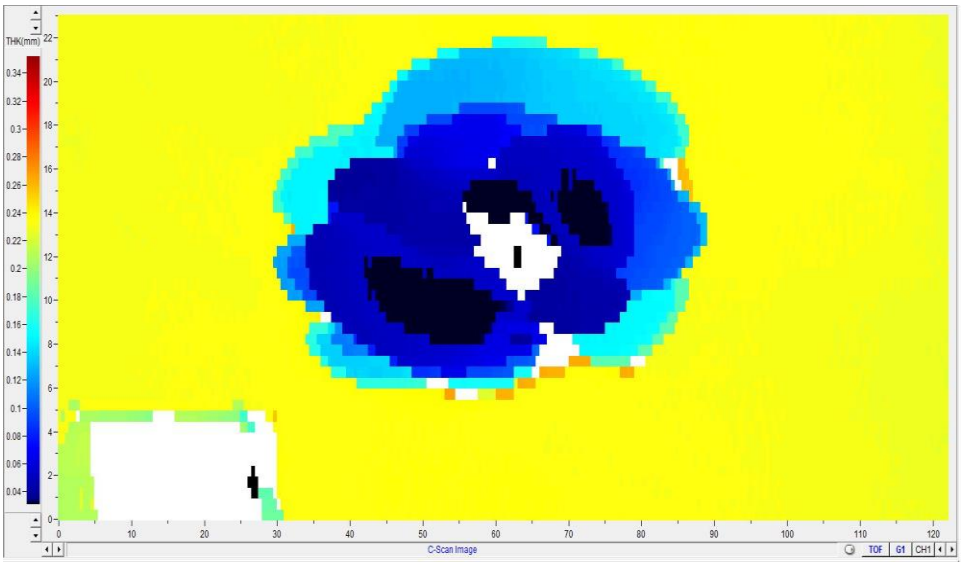

Figure 2.12: C-Scan Resolution and Speed Test 2 (0.5 mm by 0.5 mm Resolution, 25 mm/s Speed).

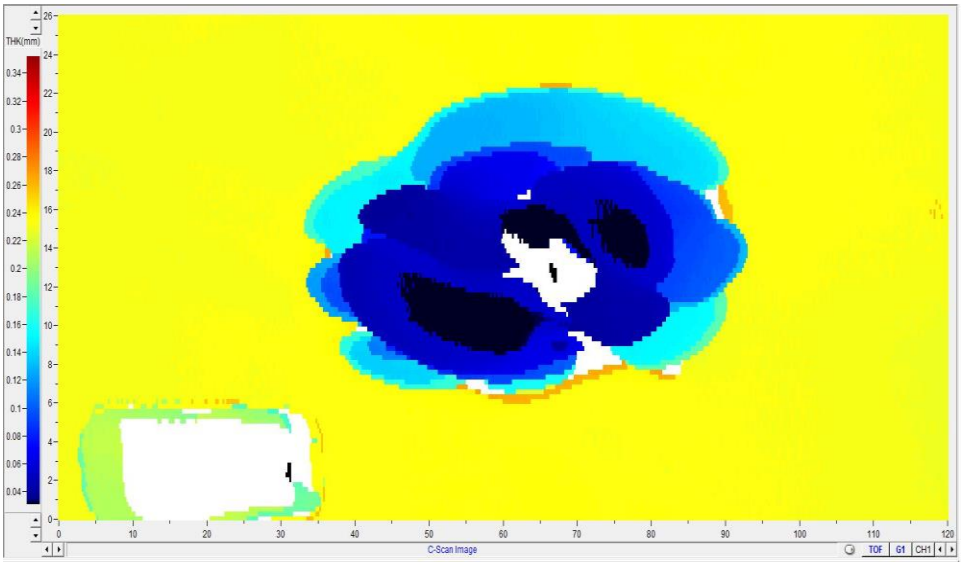

Figure 2.13: C-Scan Resolution and Speed Test 3 (0.25 mm by 0.25 mm Resolution, 25 mm/s Speed).

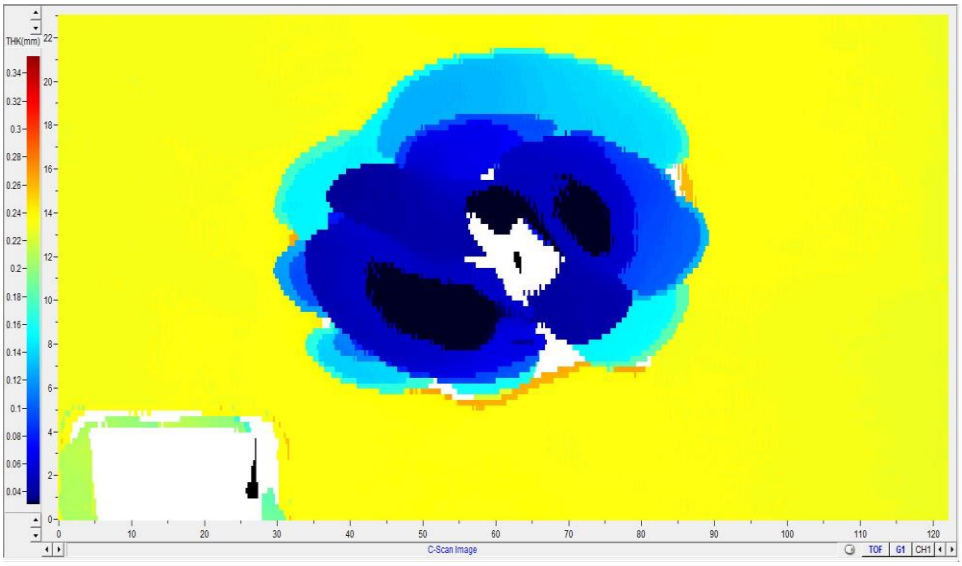

Figure 2.14: C-Scan Resolution and Speed Test 4 (0.25 mm by 0.25 mm Resolution, 15 mm/s Speed).

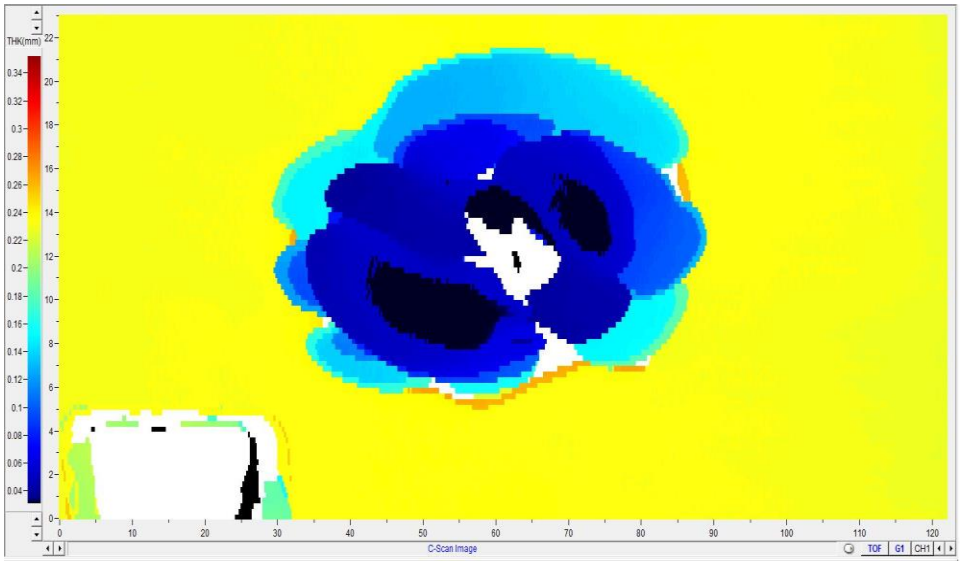

Figure 2.15: C-Scan Resolution and Speed Test 5 (0.25 mm by 0.25 mm Resolution, 50 mm/s Speed).

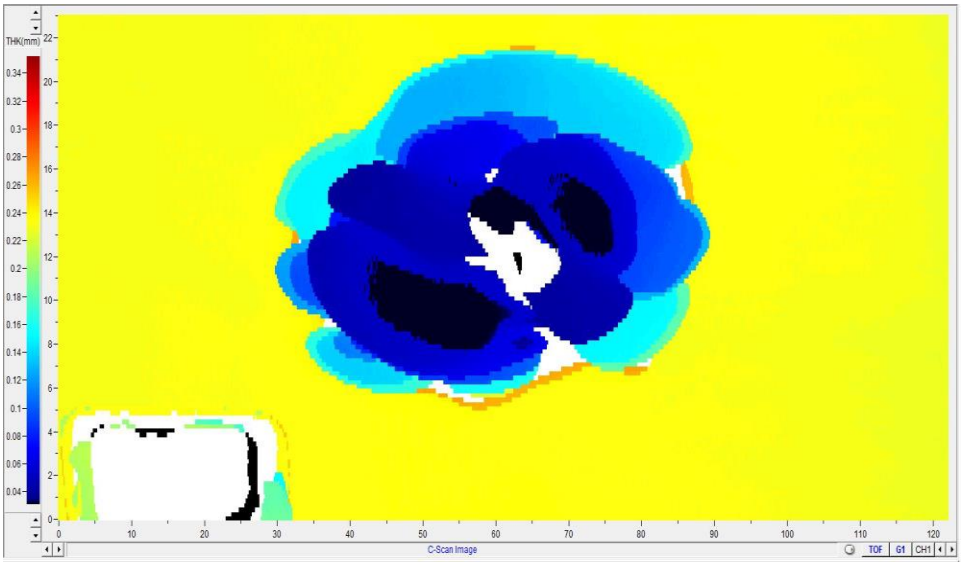

Figure 2.16: C-Scan Resolution and Speed Test 6 (0.2 mm by 0.2 mm Resolution, 50 mm/s Speed).

From Figure 2.11 and Figure 2.12, it is seen that a scan resolution of 1 mm by 1 mm and 0.5 mm by 0.5 mm is too coarse to produce high quality scans, therefore, those resolutions were both removed from consideration. For Figure 2.13 through Figure 2.15, the scan resolution was considered adequate for high quality scans. Since scan speed was the varying parameter among these tests, it was found that between the three different scan speeds, 15, 25, and 50 mm/s, there was not any significant difference in the scan quality. Therefore, to efficiently scan the damage zones in the future tests, the 50 mm/s scan speed was chosen to reduce the time per scan. Since the scan speed was chosen and the first two test resolutions were removed from consideration, the choice was between the scan resolutions used in test 5 and test 6. The scan produced in test 6 (Figure 2.16) was significantly higher quality than that of test 5 and with the scan time only increasing by 1.5 minutes. Therefore, it was decided to scan all specimens at a scan resolution of 0.2 x 0.2 mm at a scan speed of 50 mm/s.

Once the scan resolution and speed were chosen, the 81 specimens were all scanned using those same resolutions and speeds. The size of the scans were also consistent throughout differing specimens due to the start and end point of the scans being programmed into the PocketUT system and used in each scan. When a specimen was to be scanned, a square piece of 1.5 mm thick double sided 3M Foam Tape marker was stuck to the bottom right corner of the specimen. This marker allowed for the scan and specimen to be compared in the correct orientation by making sure that the foam tape is in the same spot when comparing the scan to a physical specimen or an image of a specimen. After being taped, the specimen is rinsed in deionized water to wash off any dust or other contaminants so that the scan quality can be ensured by keeping the deionized water in the immersion tank clean. Additionally, it was found that by rinsing the specimens prior to immersing them into the water of the tank there was less chance of bubbles forming on the bottom surface of the specimen, which could lead to visual errors in the scans. Once the specimen was inserted into the immersion tank, the bottom of the specimen and the tip of the transducer were checked to make sure there were no bubbles on those surfaces, and then the Mistras controller would be used to position the transducer at the bottom left corner of the specimen, where the marker was placed. From that location, called the “home location” and zeroed out on the numerical position of the arm, each specimen had a set point where the scan would end. This point encompassed the entire specimen and by making it the same location for all specimens, all scans were the same size which saved time in setting up where the scan was to go to. The scan was then ready to run, with the set scan resolution and scan speed from the resolution tests, it was found that a single specimen being scanned would take approximately 1 hour and 8 minutes to run.

In order for the scan images to correctly show the damaged region, the through-thickness wave speed of the specimen needed to be set in the PocketUT system. To set this value, an A-scan was performed on a pristine section of each panel type. From these A-scans, the time of flight (TOF) for a wave to travel from the front surface to the back surface and return to the front was recorded from a pristine region. The different panel types exhibited the same TOF in the pristine regions. Each had a pristine region return signal TOF of 2.05 μs. From this, Equation (2) was used to calculate the through-thickness wave speed of the panels. Since the panel thickness, t, was nominally 3.3 mm and the A-scan was pulse-echo, the signal travelled through the thickness to the backside and returned to the transducer, meaning that it travelled double the thickness of the panel.

$$v = \frac{2t}{TOF} = \frac{2(3.3\ mm)}{2.05\ \mu s} = 3.22\ mm/\mu s = 3{,}220\ m/s \qquad (2)$$

With the material velocity known, and the scan set up completed, a C-scan like that seen in Figure 2.17 could be obtained for each specimen. Figure 2.17 shows the C-scan of the specimen shown in Figure 2.8, the A-scan and C-scan can be seen to have similar characteristics on the perimeter, but with the C-scan contour plot is much more useful for understanding the extent of the damage through the thickness of the specimen since the color scale shown provides information about the depth of the delaminations (note: background dark red is 3.3 mm panel thickness in undamaged zones).

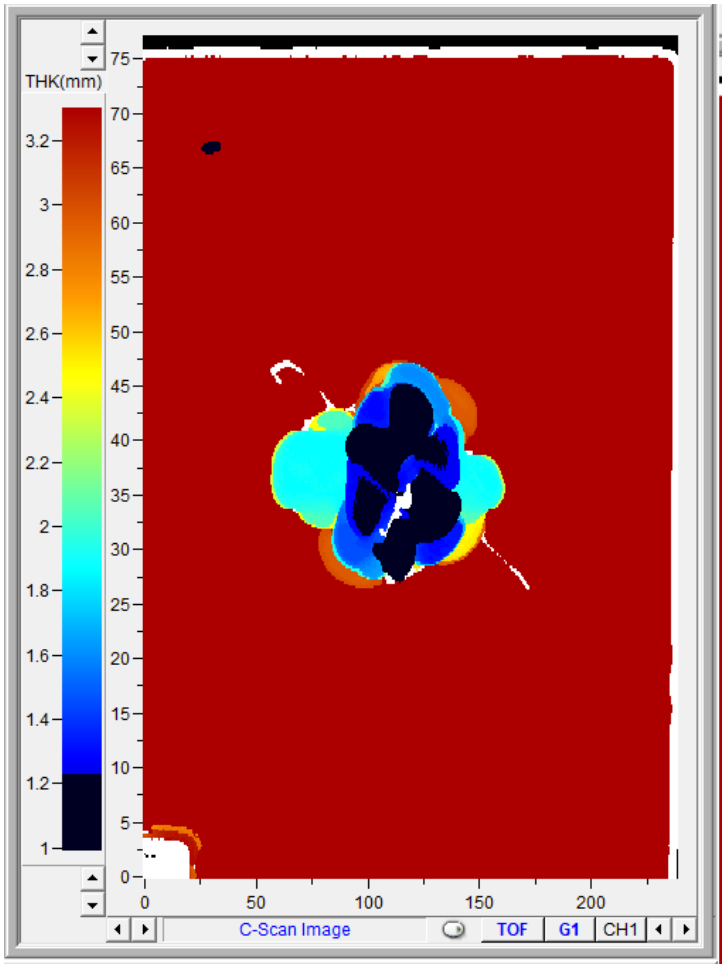

Figure 2.17: C-Scan Image of a 20 J Impacted Hard Laminate.

CHAPTER 3: RESULTS AND DISCUSSION

There were 81 impacts performed for this study. 9 impacts were conducted per energy level and panel type pairing. For each impacted specimen, the following data was collected: force versus time data from the impact, A-scan hand-mapping of the damage perimeter, and C-scan imaging of the entire specimen.

3.1 Impact Event

As discussed in Section 2.1, the 81 specimens were impacted at varying energy levels using a pendulum impactor system. The data from the impact event was recorded with a Picoscope data acquisition system (DAQ). The data that the Picoscope DAQ collected included the impact force data from a force sensor equipped on the pendulum arm tip mass, as well as the time data of the impact event from a laser photogate that recorded the pendulum arm swinging into and bouncing back from the impact event. From this data, force versus time plots were created for each impact event. Figure 3.1 shows the force versus time plot for one of the specimens. This plot has been annotated to call out the location where damage is initiated in the specimen, as well as the peak impact force. The damage initiation is identified as the highest force value developed before a major drop in the force magnitude occurs, which is then followed by significant oscillations (noise/ringing of the sensor). This drop is due to the specimen becoming damaged (delamination, cracking, etc.) which causes a loss in force magnitude as the specimen deforms locally and complies with the impactor.

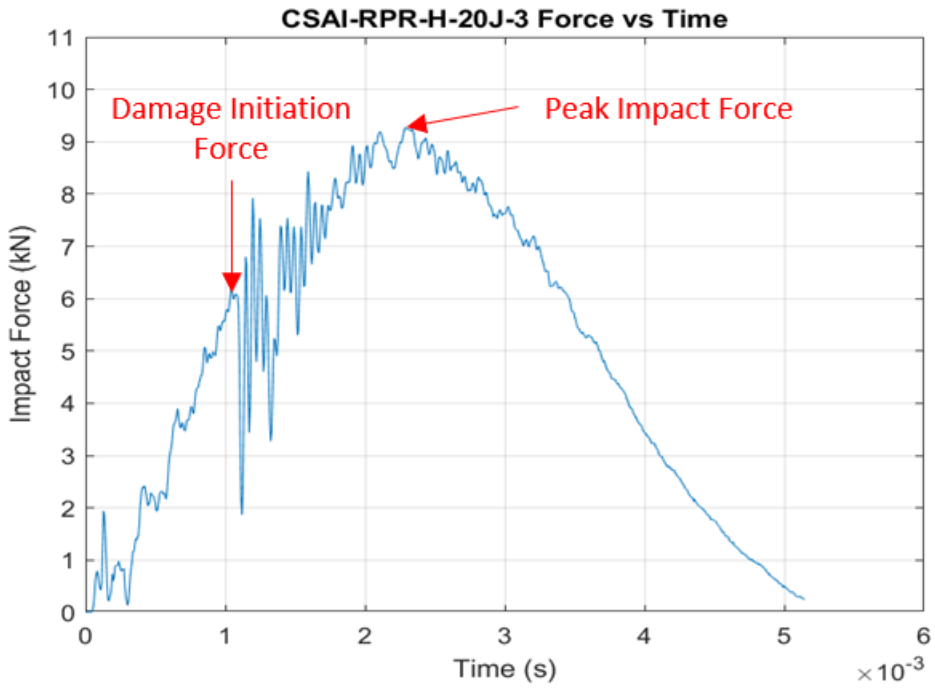

Figure 3.1: Location of Damage Initiation Force and Peak Impact Force Magnitude.

The 81 force versus time plots are summarized by six figures which group results based on same energy level with different panel types (Figures 3.2 to 3.4) or same panel types with different energy level (Figures 3.5 to 3.7). These force versus time curves plotted on top of one another to show the distinctions in the result due to differing impact energy level or panel type. In each of the plots from Figure 3.2 to Figure 3.7 a representative curve from each panel type and energy level combination was chosen to represent that grouping, this chosen curve was the best representation of the population of curves for the nine specimens in each of those groups. In Figure 3.2 there are three 10 J impact event Force versus Time curves plotted, one for each panel type. Similarly, Figure 3.3 plots three 15 J impact event Force versus Time curves, and Figure 3.4 plots three 20 J Force versus time curves, each of the plotted curves is representative of one of the panel types. On the other hand, Figure 3.5, Figure 3.6, and Figure 3.7 plot three Force

versus Time curves that are representative of a singular panel type with curves from each of the three energy levels, the panels plotted by figure are H, M, and S, respectively.

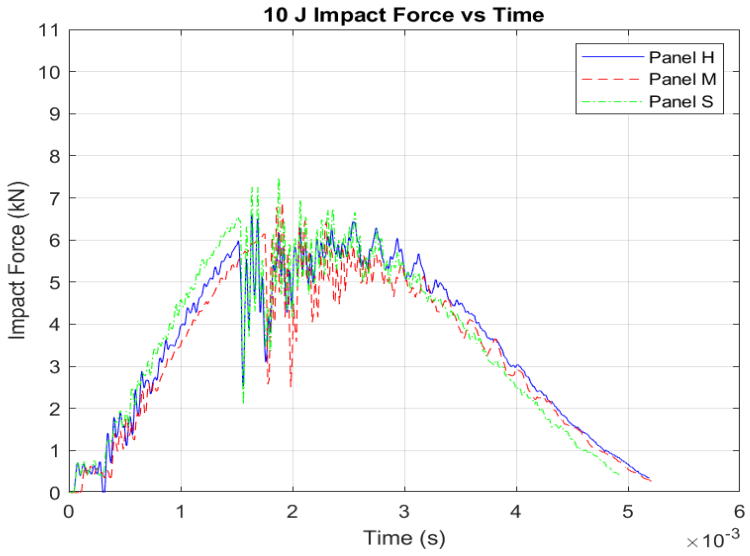

Figure 3.2: Impact Force Versus Time for 10 J Impacts for all Panel Types.

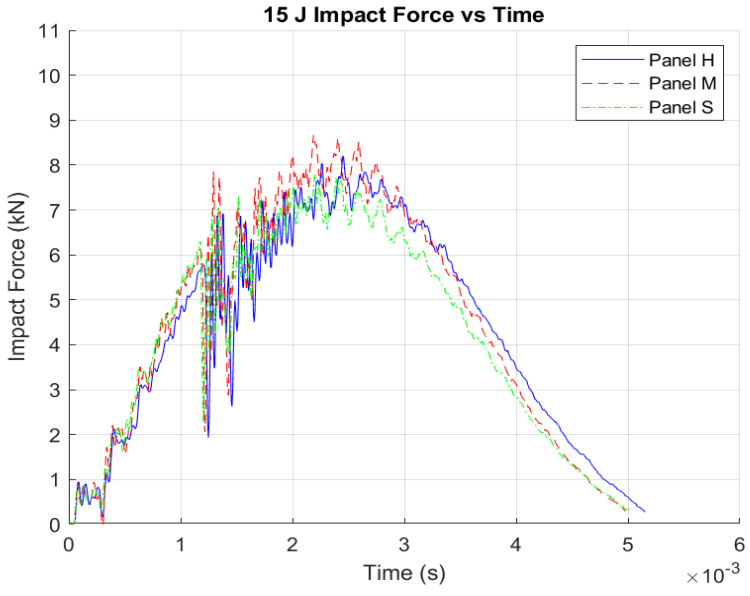

Figure 3.3: Impact Force Versus Time for 15 J Impacts for all Panel Types.

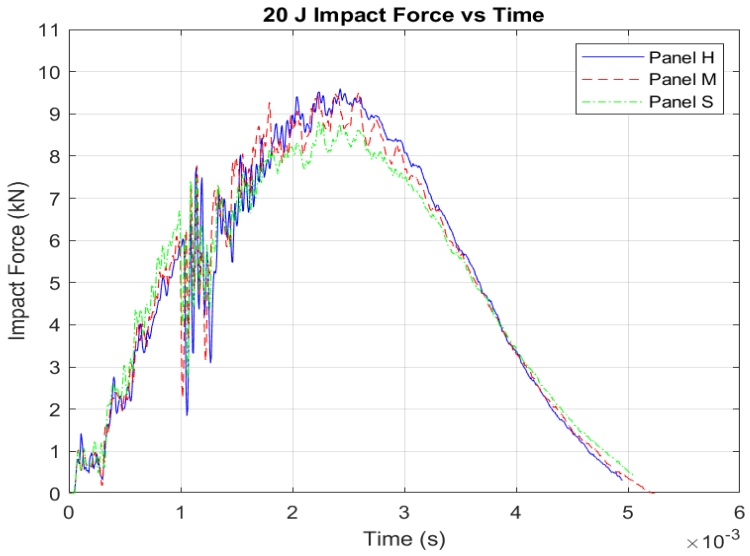

Figure 3.4: Impact Force Versus Time for 20 J Impacts for all Panel Types.

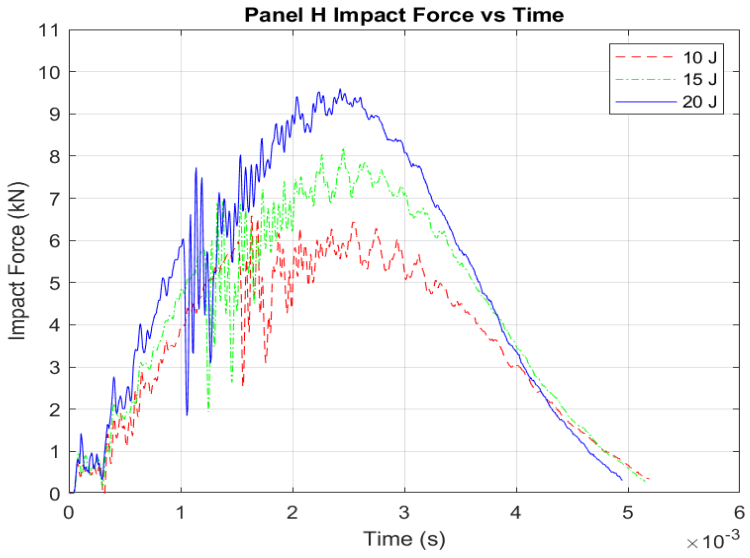

Figure 3.5: Impact Force Versus Time for Panel H Impacts (10 J, 15 J, and 20 J Impacts).

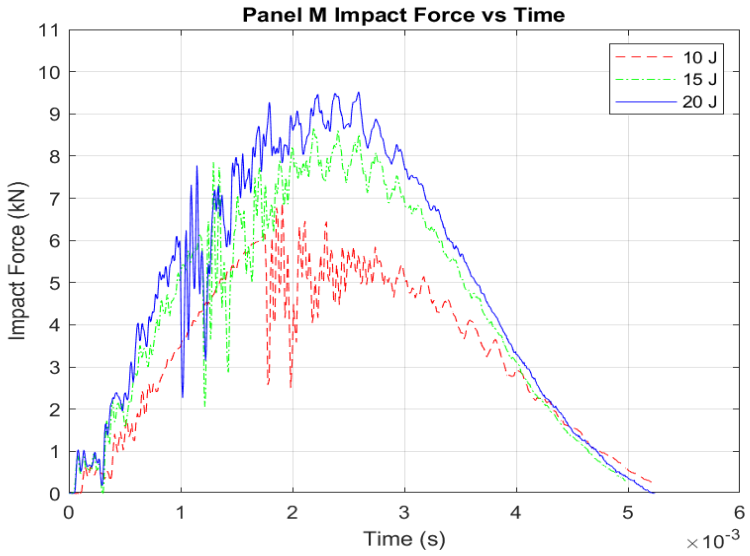

Figure 3.6: Impact Force Versus Time for Panel M Impacts (10 J, 15 J, and 20 J Impacts).

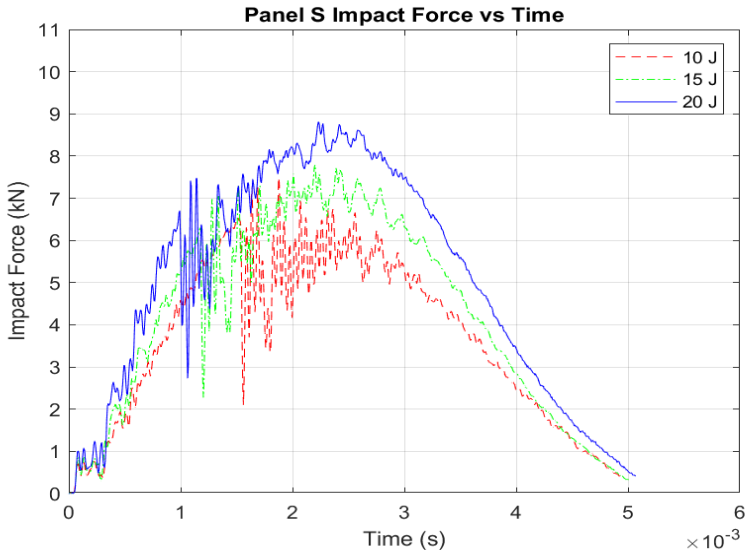

Figure 3.7: Impact Force Versus Time for Panel S Impacts (10 J, 15 J, and 20 J Impacts).

From Figures 3.2 to 3.4 it is seen that the Panel S Force versus Time curves have lower peak force magnitudes across all three impact energy levels when compared to the same impact energy levels in panels M and H. However, the force where damage to the panel is initiated is

higher in Panel S than it is in panels M and H. Interestingly, it can be seen that there is an inverse relationship between damage initiation force and peak impact force for Panel S. Panel S, as previously stated, has a higher damage initiation force when compared to the other panel types. The difference in damage initiation force can be attributed to the difference in fiber orientation that the panel types have. Panel S is comprised of 16% 0° plies, 64% ±45° plies, and 20% 90° plies. The amount of 90° plies present in the Panel S layup greatly exceeds those found in the Panel H and Panel M layups (both contain only 4% 90° plies). This large difference in 90° plies is the main driver in why Panel S has a higher damage initiation force. Since the impact event occurs in the center of the specimen, and the specimen is constrained along each edge, the increase in 90° plies gives Panel S increased stiffness in the short direction of the specimen (the long edge of each specimen is the 0° direction). By having 16% more 90° plies, the loading from the impact event is able to transfer to the clamped constraints that are on the short edge following the load path of the 90° plies, thus Panel S has the advantage of utilizing the boundary conditions that are closer to the impact epicenter more effectively than Panel M and Panel H. The average damage initiation force with error bars for each panel and impact energy are plotted in Figure 3.8. The damage initiation force is found to be mostly insensitive to impact energy, as the forces developed during the impact event reaches the critical level for all energies investigated. This figure further shows that Panel S has the highest damage initiation force across all 27 specimens at each energy level. The plot also shows that Panels H and M are very similar but Panel H has slightly lower damage initiation forces than Panel M.

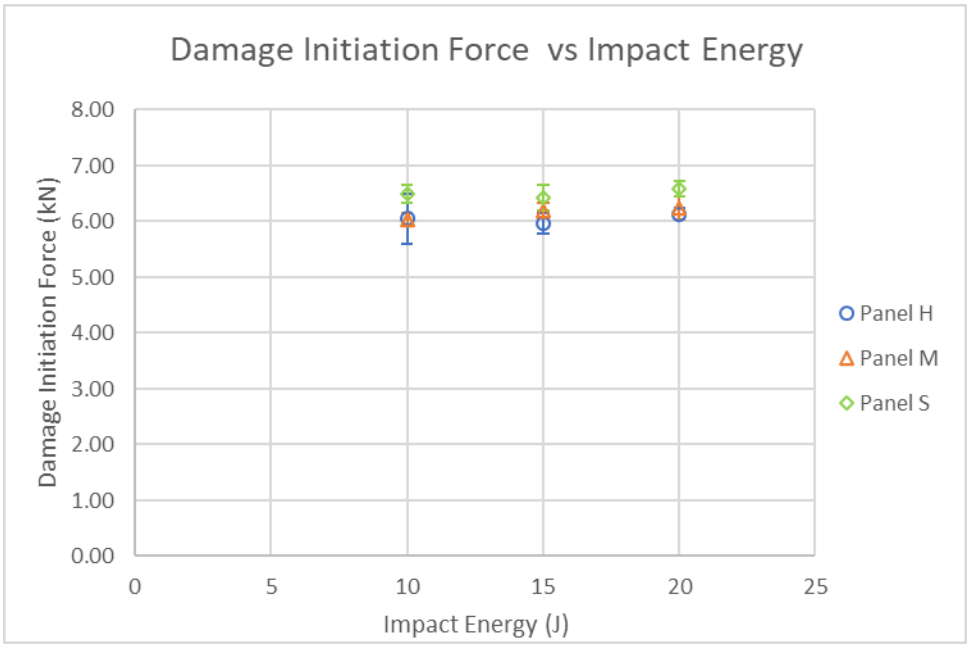

Figure 3.8: Damage Initiation Force Versus Impact Energy Level for all Specimens.

An additional reason for the higher damage initiation force in Panel S is that the interlaminate shear strength (ILSS) of Panel S is higher than that of Panel H and Panel M due to the stacking sequence of the plies around the midplane of the laminate. It has been found that as the fiber orientation directly surrounding the midplane of the laminate varies from 0° to 90° there is a decrease in ILSS in the laminate [14]. In all three panel types, the midplane ply has a fiber orientation of 90°. The midplane is the location of maximum shear stress in the laminate, since the midplane fiber direction is 90° and that corresponds with the shortest path to the edge constraints, this 90° direction can be characterized as our primary load path in the laminates during impact. The midplane ply as well as the plies directly above and below that ply, are the critical plies in the laminate for shear stress related failures. Looking at the fiber orientations of the ply at the midplane of the laminate, as well as the plies above and below it, the following three-ply stack sequences are attained for each panel (H, M, and S): [0/90/0], [-45/90/-45], and [90/90/90], respectively. Panel S has a 0° change in fiber orientation from midplane to the

surrounding plies, allowing the shear stress to follow the load path to the short edge boundary conditions using the three 90° plies. On the other hand, since the midplane of Panel H has a fiber orientation change of 90° from midplane ply to the next plies above and below, the ILSS is expected to be lower since only that midplane ply will transfer load from the impact towards the short edge. Panel M has a 45° change between plies which allows some of the load to be transitioned from the 90° ply to the -45° plies, a less drastic transition than from the 90° to 0° plies of Panel H. This is showcased in Figure 3.8 as there is a noticeable decrease in damage initiation force from Panel S to Panel M and Panel H due in part to the decrease in ILSS. Additionally, it is seen that the damage initiation force in Panel M is marginally higher than that of Panel H, which confirms that the -45° plies by the midplane provide more assistance with the impact load transfer than the 0° plies do.

The force required to initiate damage was highest in Panel S, due to this the damage size of the internal delaminations were also largest in Panel S. As seen in Figure 3.9, across the three impact energy levels Panel S has the largest damage sizes, with Panel M and Panel H competing for smallest delamination size. The delamination size of each specimen was determined by measuring the longest length between edges of the delamination perimeter per the hand-mapped ultrasonic A-scan, as discussed in Chapter 2.

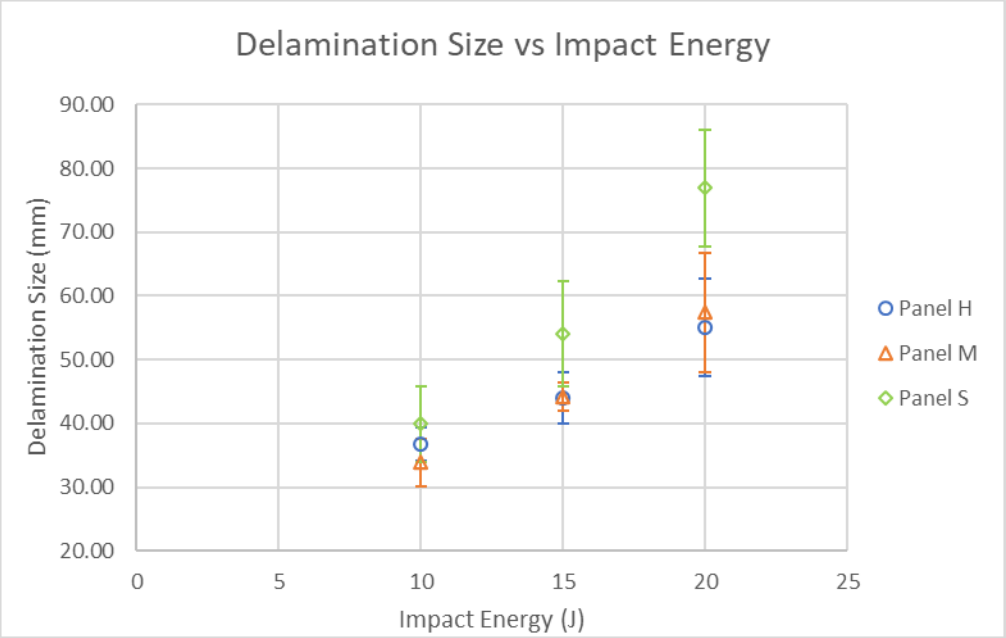

Figure 3.9: Delamination Size Versus Impact Energy Level for all Specimens.

The delamination sizes of Panels H, M, and S seem to follow a similar trend as the damage initiation for each, the damage size is related to the damage initiation force magnitude. Panel S has the largest delamination sizes because of the damage initiation force being larger in that Panel than the other panels. This causes larger delaminations because there is more strain energy stored in the panel before damage occurs which causes a more catastrophic delamination once damage is initiated because there is more strain energy in the system to be released. The normalized amount of energy absorbed in the three panels across the three energy levels can be seen in Figure 3.10. Normalization is done by dividing the absorbed energy by the incoming projectile impact energy. It can be seen for all three impact energies that the amount of energy absorbed from the impact is about half of the incoming energy. This energy is absorbed into the panel via the damage spreading through the specimen during impact. Similar to the delamination size plot, Panel S has the most energy absorbed in the impact event, with panel M and Panel H once again having very similar results.

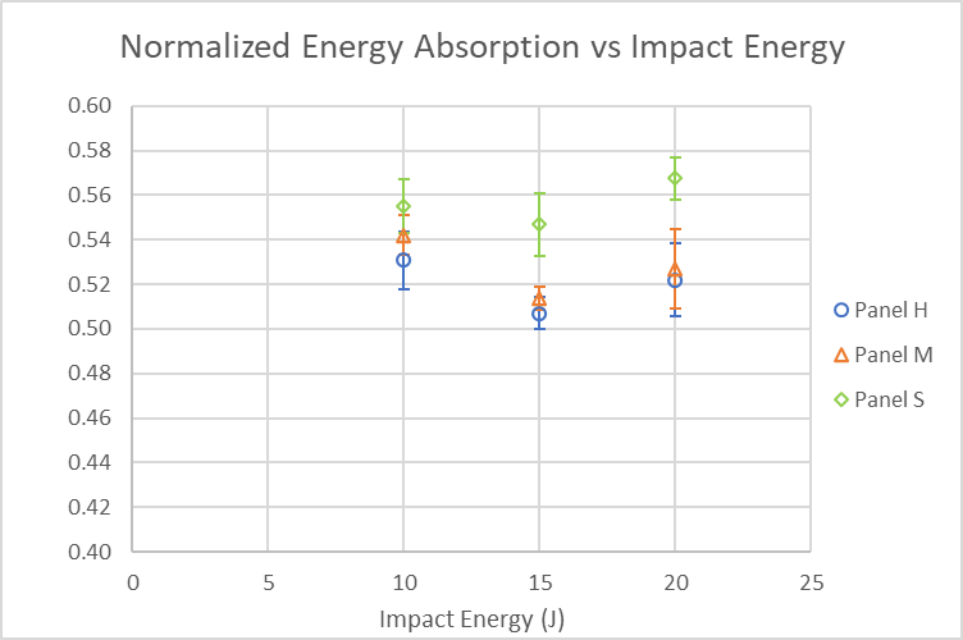

Figure 3.10: Normalized Energy Absorption Versus Impact Energy Level for all Specimens.

Along with the force magnitude at the point of damage initiation being recorded, the peak impact force for each specimen was also recorded. Surprisingly, Panel S had the lowest peak impact force of the three panels in the 15 and 20 J impacts. While this seems unanticipated since Panel S had the highest damage initiation force across all panel types, as well as the largest delamination sizes and most energy absorption, it actually makes sense that the peak force drops when compared to Panels M and H. The peak force in Panel S drops in the 15 and 20 J impacts because once the damage is initiated the laminate experiences more extensive damage than the other two panel types, this extensive spread of damage does not allow the force to climb as high as is seen in Panels M and H.

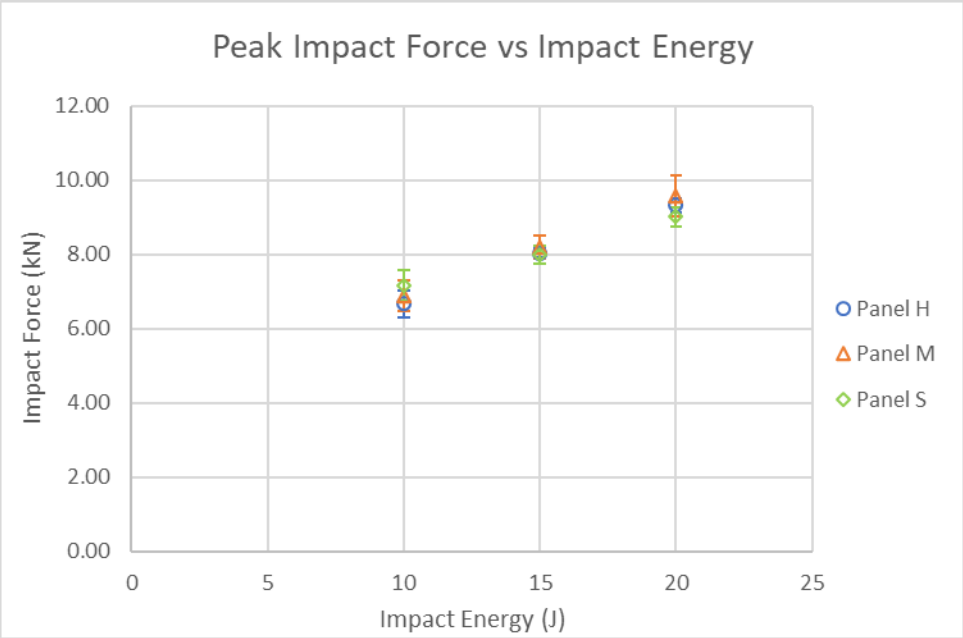

Figure 3.11: Peak Impact Force Versus Impact Energy Level for all Specimens.

3.1.1 Force Versus Time Plot Error

During the process of collecting the force versus time data from the impact events there was an unforeseen error that effected the data acquisition from the force sensor in six of the impact event recordings. For six 15 J impacts on Panel M specimens the battery in the force sensor was dying. Due to this, the force sensor was reading data from the impact, but once the voltage readout from the sensor reached a level that required more energy to capture than the battery had charge to handle, the sensor would plateau at that level for the rest of the impact until the voltage dropped back down to levels it had enough energy to read. These six incorrect readings are shown from Figure 3.12 to Figure 3.17. To recognize what the force versus time plot would look closer to if the battery had been charged, one of the impact events from this same energy level and panel type that did not suffer from the dying battery in the force sensor data acquisition was plotted on top of the inaccurate data. For each of the six plots, the initial data acquired by the force sensor is seen to match very well with the accurate reference curves event up until the point where the force sensor is unable to accurately collect the force data and the plot begins to

plateau. The force data collection was the only part of these specimens that had errors, therefore these specimens were still used in the damage detection and characterization investigation that was done after the impacting of specimens.

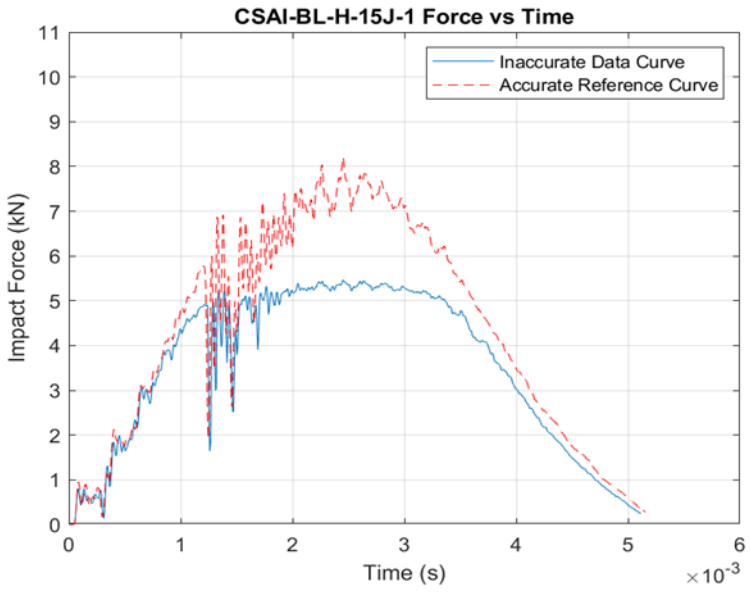

Figure 3.12: CSAI-BL-H-15J-1 Inaccurate Data Collection Plot with Reference Curve.

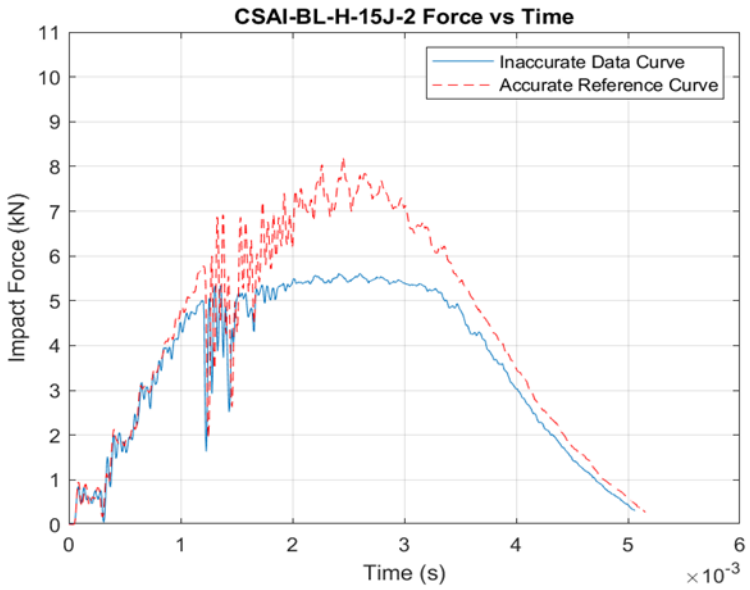

Figure 3.13: CSAI-BL-H-15J-2 Inaccurate Data Collection Plot with Reference Curve.

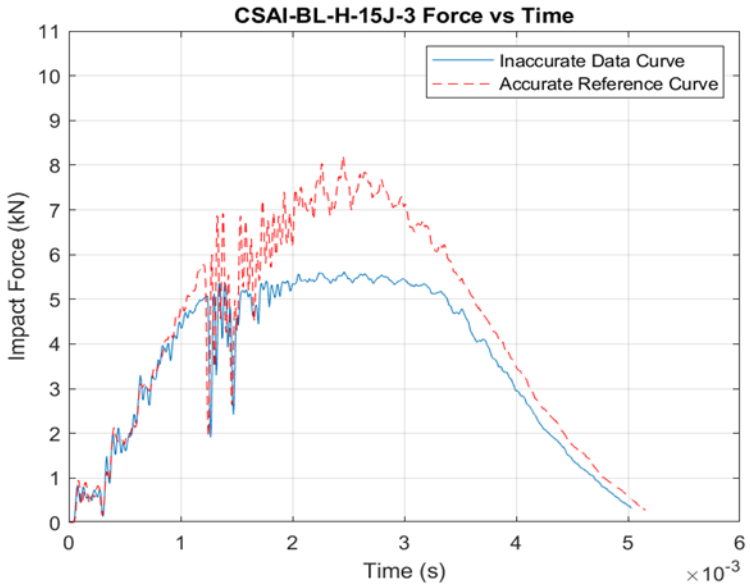

Figure 3.14: CSAI-BL-H-15J-3 Inaccurate Data Collection Plot with Reference Curve.

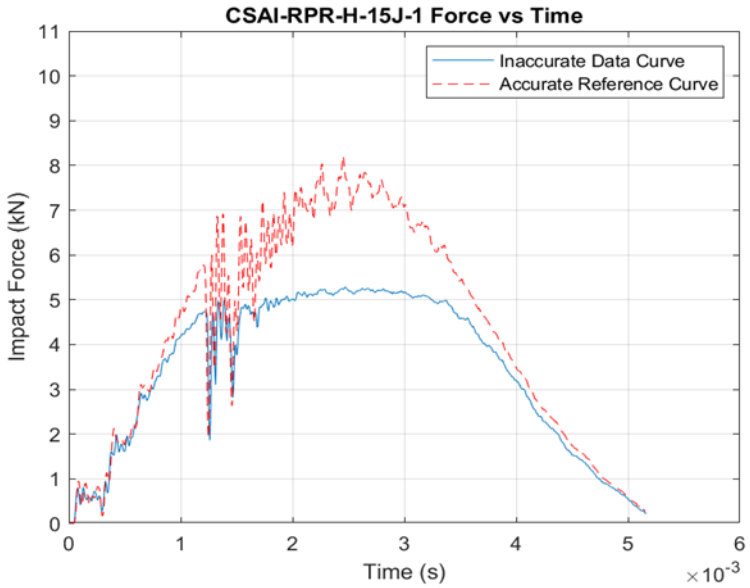

Figure 3.15: CSAI-RPR-H-15J-1 Inaccurate Data Collection Plot with Reference Curve.

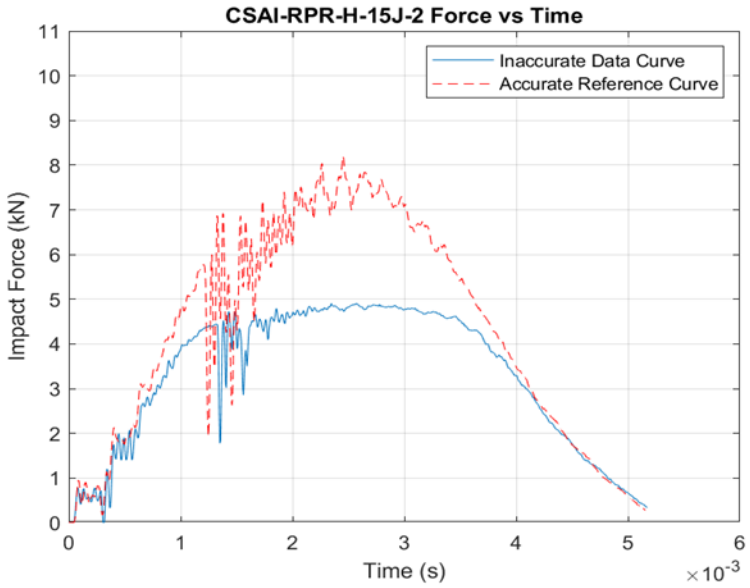

Figure 3.16: CSAI-RPR-H-15J-2 Inaccurate Data Collection Plot with Reference Curve.

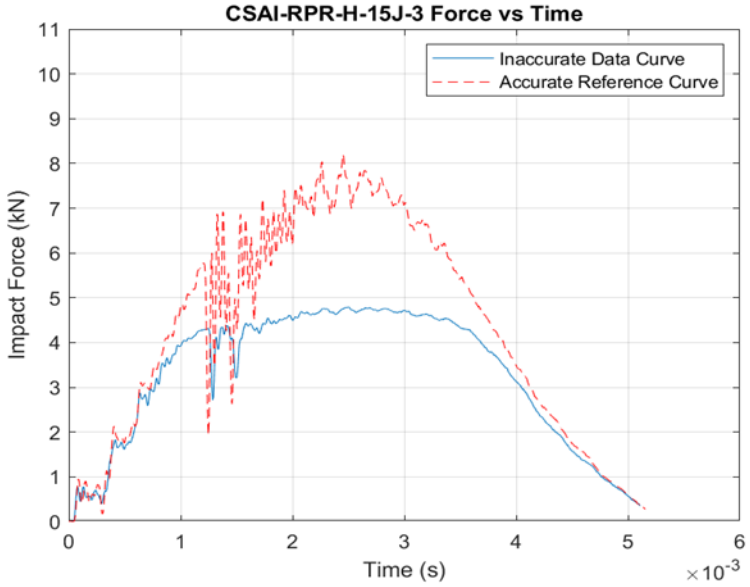

Figure 3.17: CSAI-RPR-H-15J-3 Inaccurate Data Collection Plot with Reference Curve.

3.2 Non-Destructive Evaluation Results

Once the impact experiments had been carried out, each specimen was then inspected with non-destructive methods to determine the extent of damage and to characterize that damage, as discussed in Chapter 2 previously. There were 81 impacted specimens, each was inspected using two separate ultrasonic pulse-echo scanning methods. The first method used was hand mapped A-scans to determine the extent of the damage and to draw the perimeter so a visual could be seen on the surface of each specimen. The second method was C-scans that were performed in an immersion tank using a machine-controlled transducer. This method allowed for a digital view of the top face of the specimen to be plotted with a contoured view of the damage region to allow the depth of delamination zones to be visualized. Rather than showing 81 scans, nine have been chosen (one from each material type and energy level pairing) and are shown in Figure 3.18 through Figure 3.26. These figures each have a photo of the physical specimen after being A-scanned on the left, with the C-scan of that image on the right. The first three figures are the 10 J impacts, followed by the three chosen 15 J impacts, and finally the three 20 J impacts.

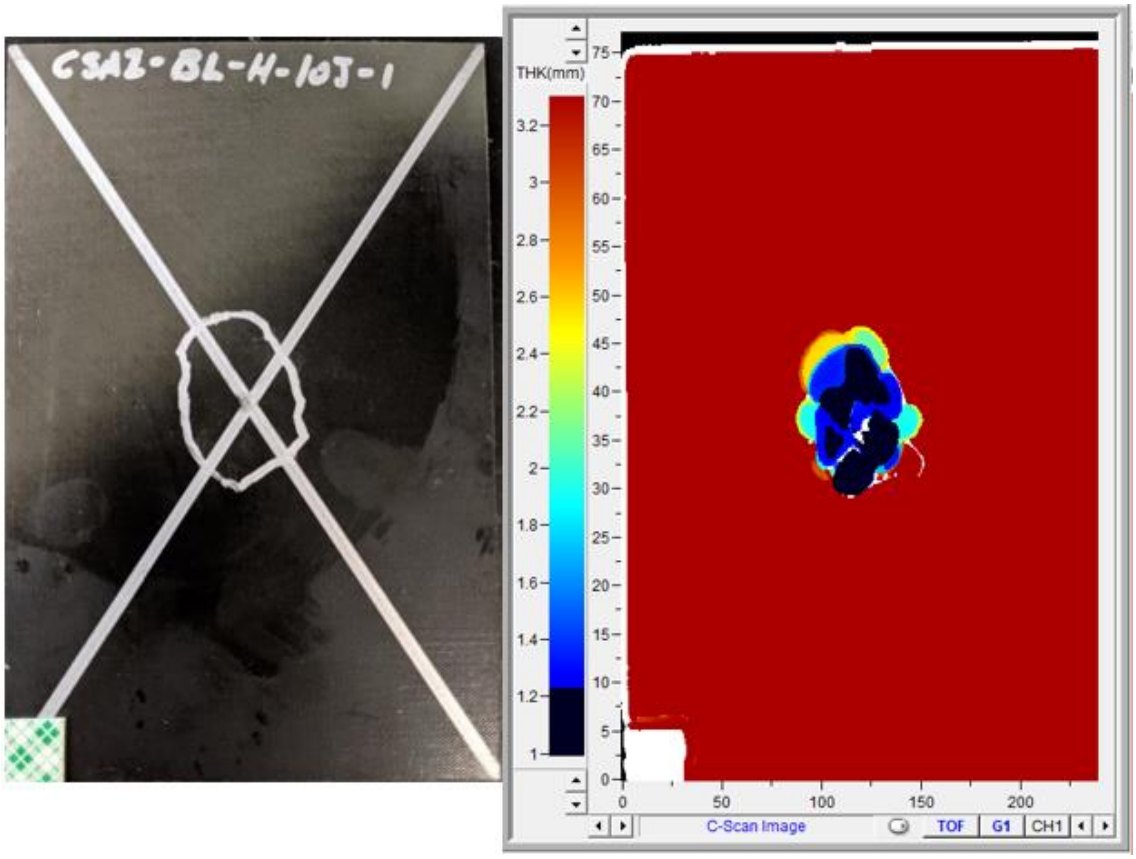

Figure 3.18: A-Scan and C-Scan Images of a 10 J Panel H Specimen.

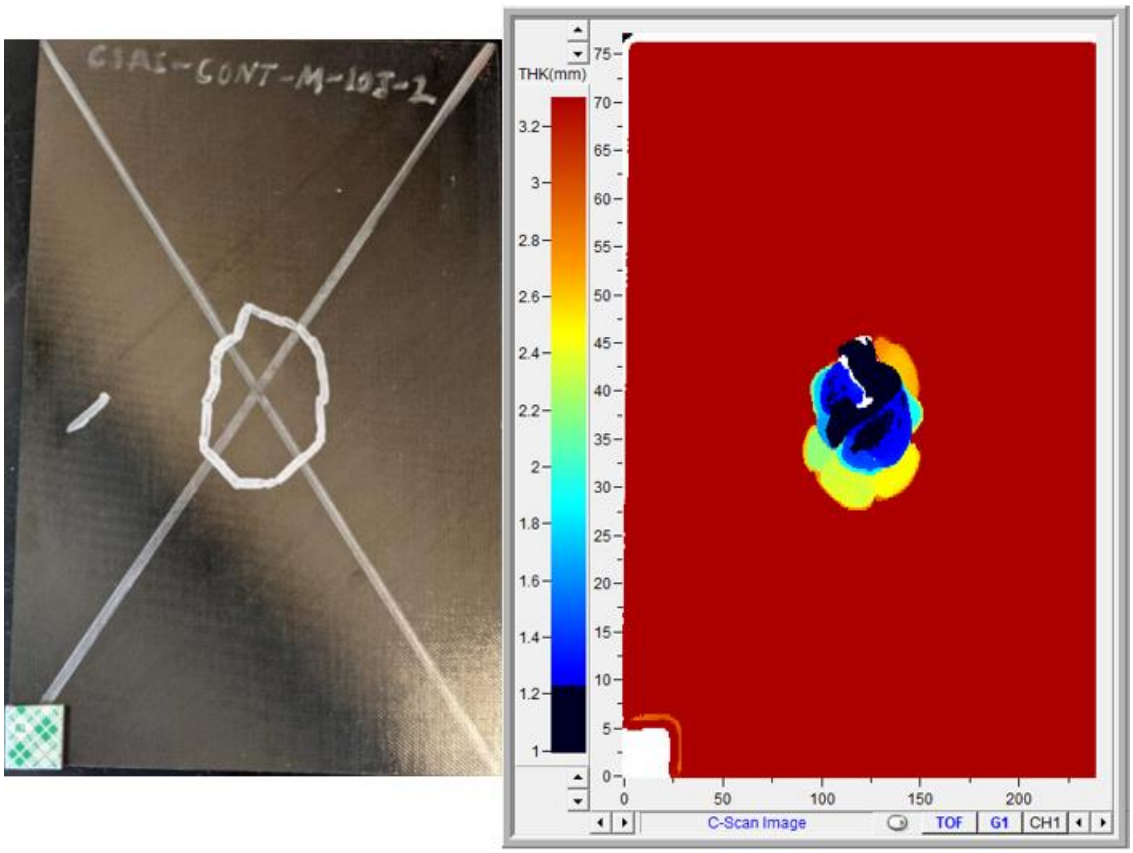

Figure 3.19: A-Scan and C-Scan Images of a 10 J Panel M Specimen.

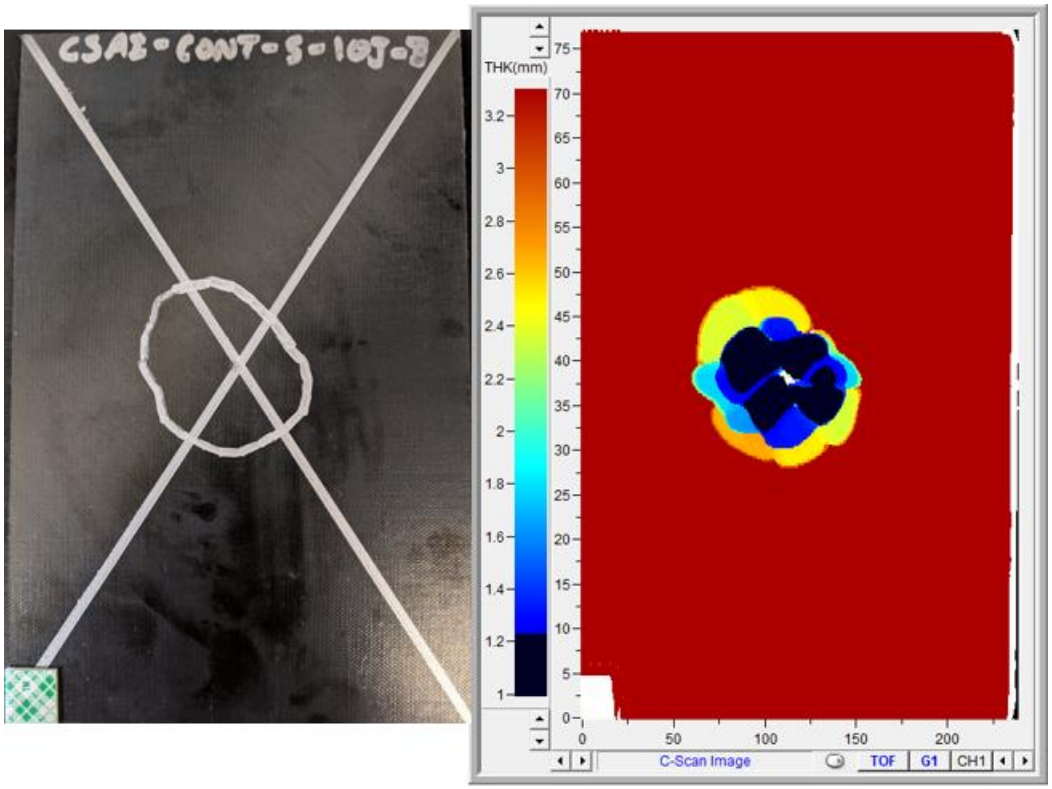

Figure 3.20: A-Scan and C-Scan Images of a 10 J Panel S Specimen.

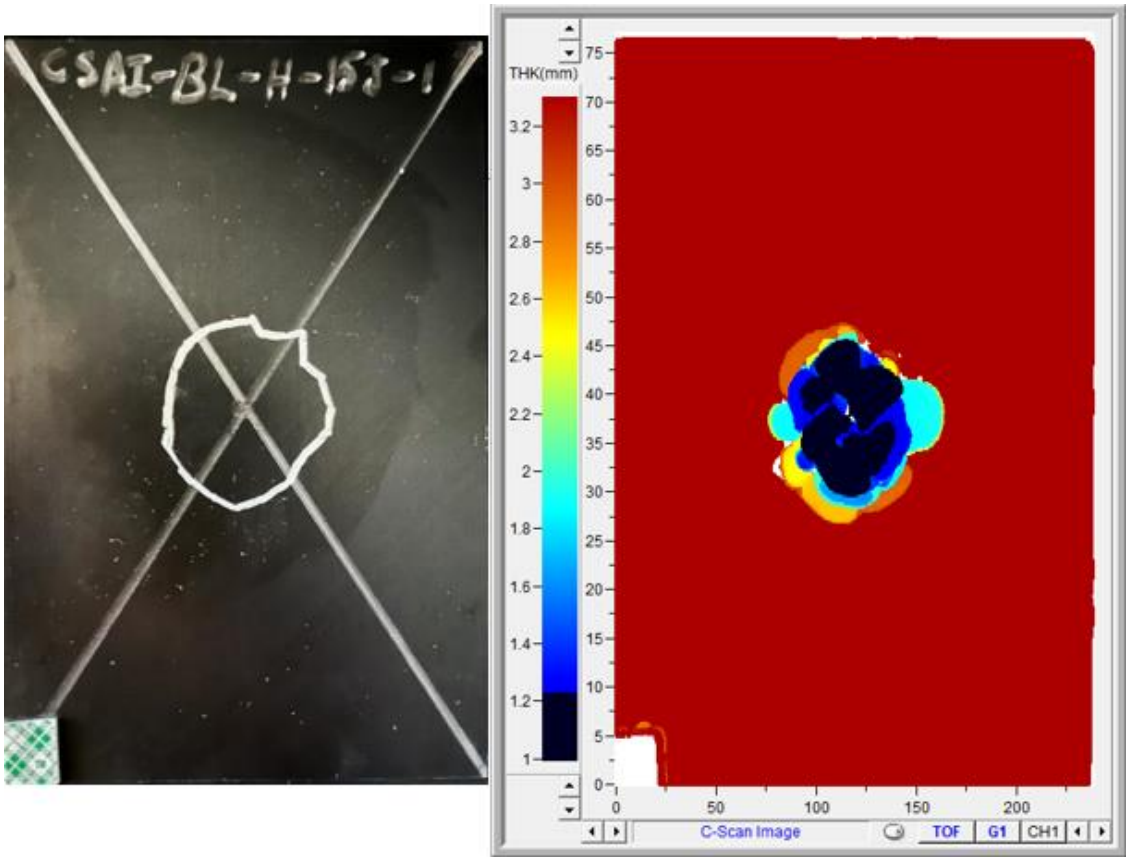

Figure 3.21: A-Scan and C-Scan Images of a 15 J Panel H Specimen.

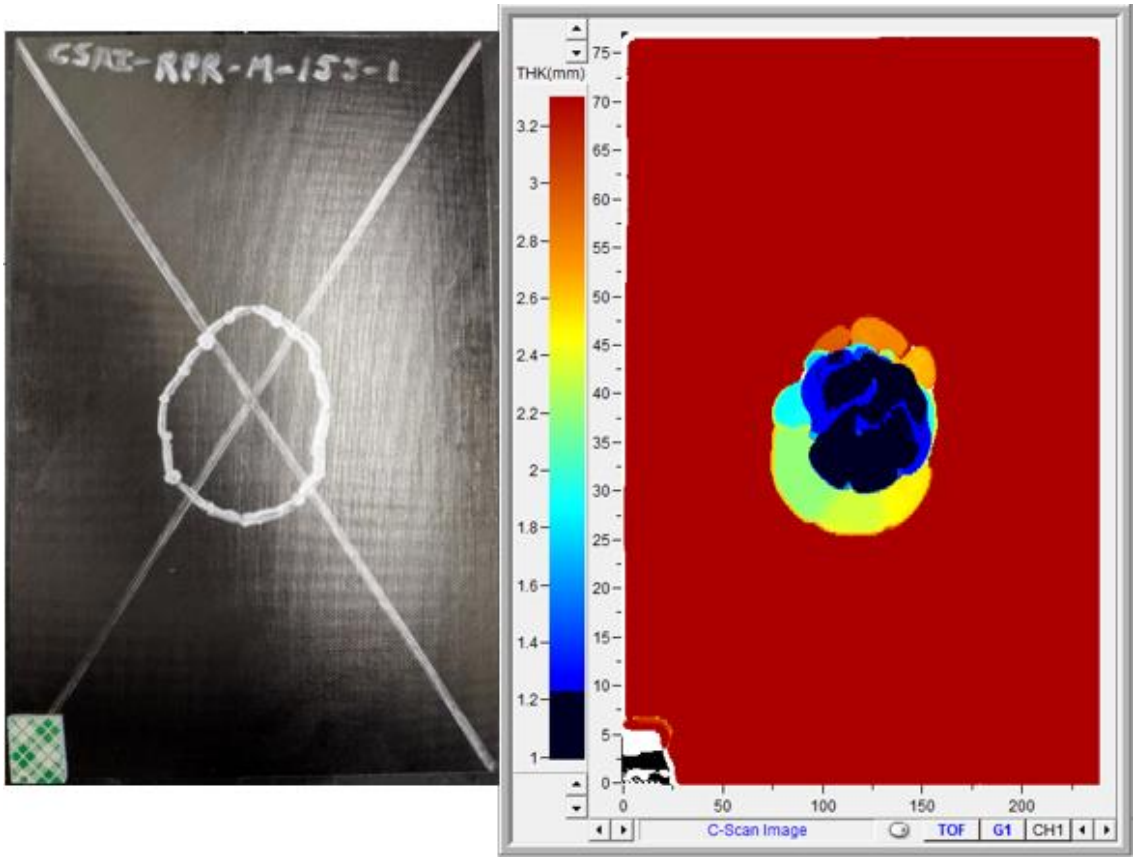

Figure 3.22 A-Scan and C-Scan Images of a 15 J Panel M Specimen.

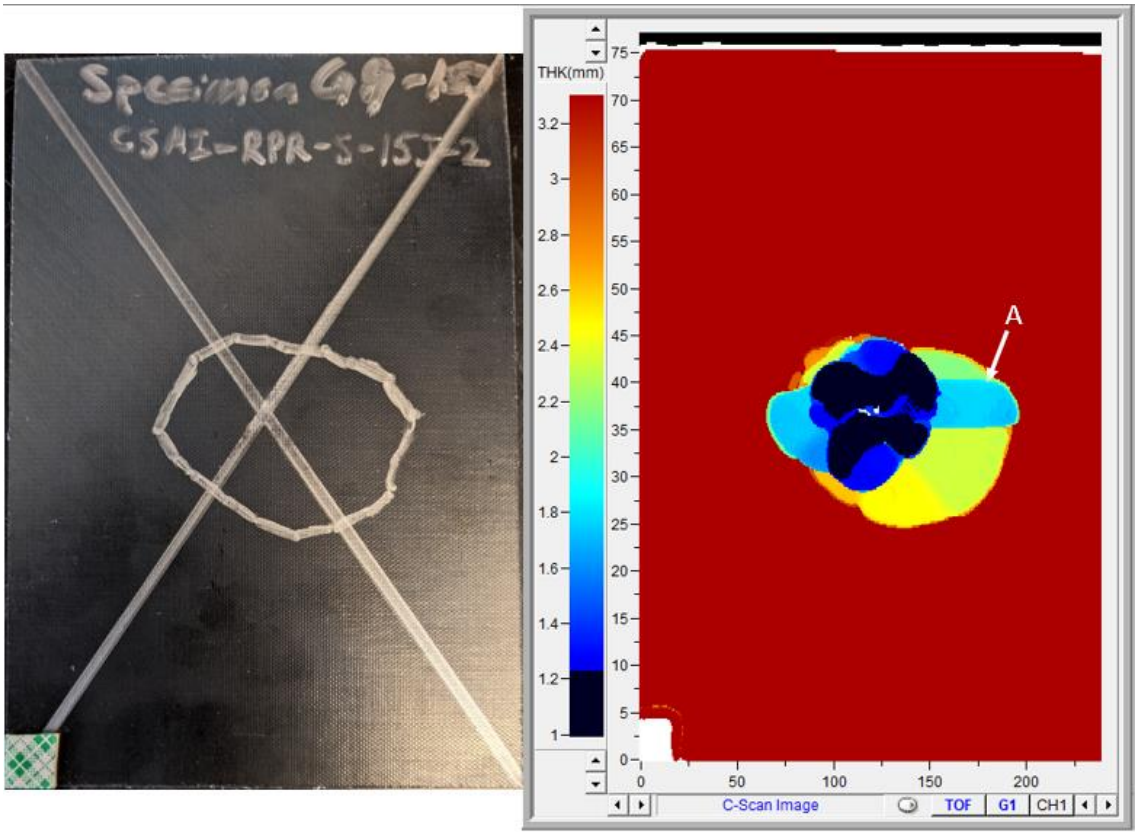

Figure 3.23: A-Scan and C-Scan Images of a 15 J Panel S Specimen.

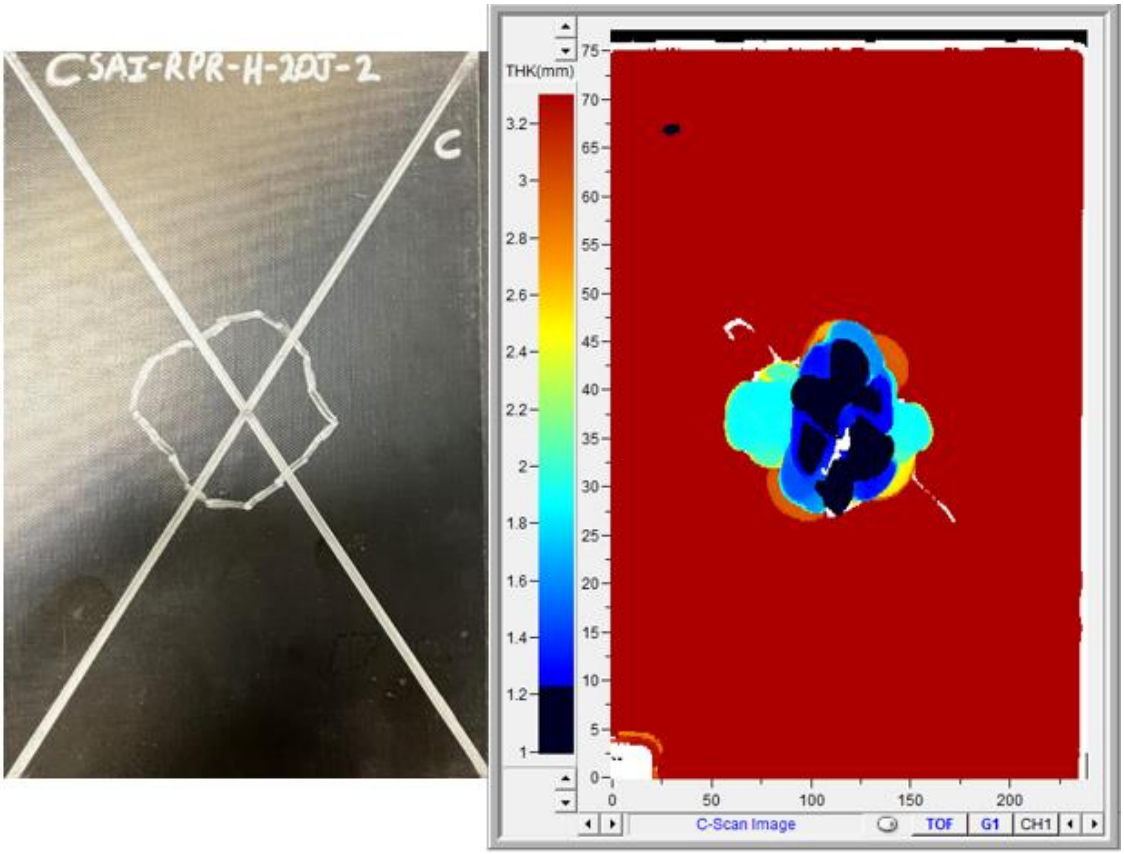

Figure 3.24: A-Scan and C-Scan Images of a 20 J Panel H Specimen.

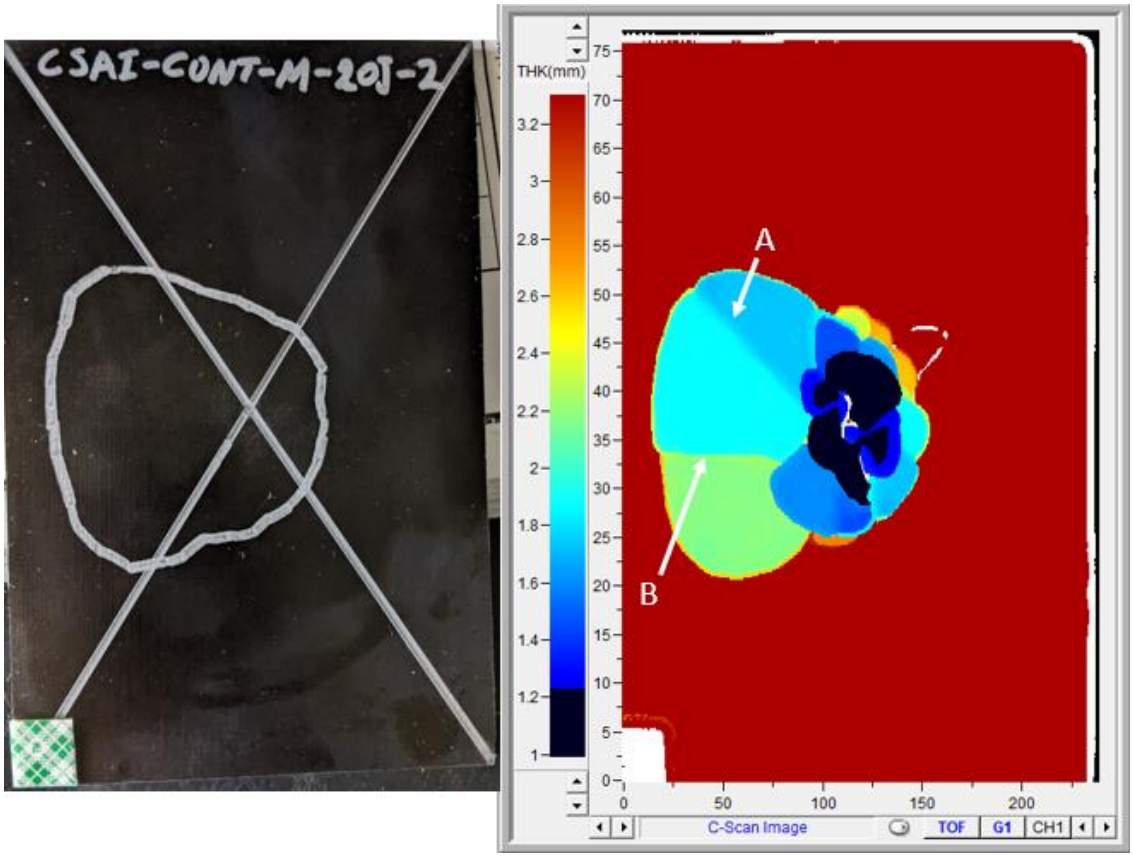

Figure 3.25: A-Scan and C-Scan Images of a 20 J Panel M Specimen.

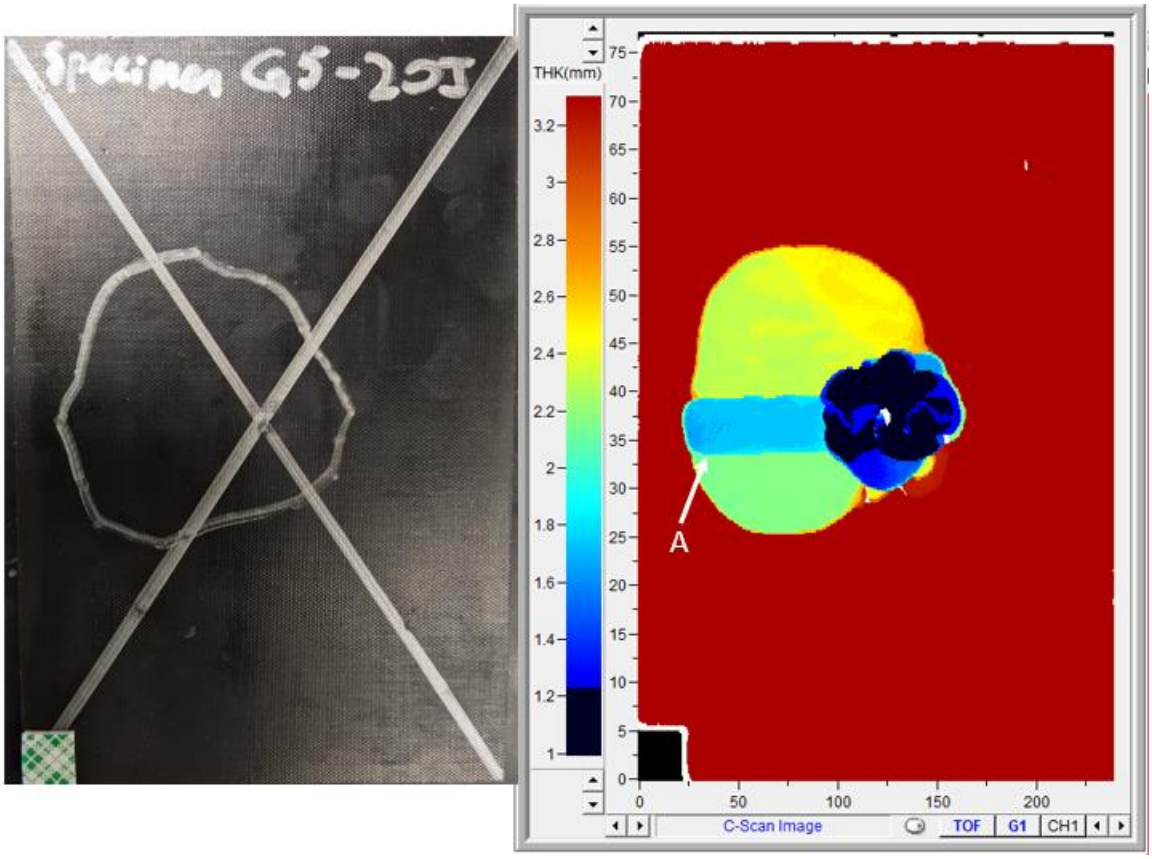

Figure 3.26: A-Scan and C-Scan Images of a 20 J Panel S Specimen.

It is seen that while the A-scans were able to accurately represent the perimeter of the damage region, the C-scan image is much more useful in understanding the damage region to a higher level. From the previous nine figures it can be seen that the damage profile of these specimens varies tremendously from specimen to specimen. Each impact creates a novel damage region that does not match the damage created in a previous test, even at the same energy level on the same panel type. The delaminations in all of the specimens occur on multiple planes and in multiple directions through the laminate. The size and shape of the delamination varies between the panel type and energy level, many are ovular with multiplanar delaminations, some have intricate shapes that extend beyond the ovular region and give the specimen a more distinctive damage profile. In the scans, there are white regions that occur at the epicenter of the

impact, these white regions represent a dent that while hard to detect by human eye, is able to be noticed by the transducer due to the wave being reflected off of it. Some specimens, such as Figure 3.25, have an additional white region. In this case that is a surface level disbond from the impact, effectively the first ply of the laminate has a crack from the impact. All 81 specimen C-scan images can be found in Appendix IV.

From the C-scan images, there are interesting characteristics about the damage profile in Figure 3.23, Figure 3.25, and Figure 3.26. These three figures have large sized delamination regions that extend to where the clamping boundary condition begins. The most interesting part of these figures, however, is the way that certain delaminations in the laminate follow the midplane fiber orientation. Figure 3.23 and Figure 3.26 are both Panel S and therefore have a [90/90/90] midplane, it is interesting to note that call out A shows the delamination following the 90° direction and is right around the midplane of the laminate. Similarly, Figure 3.25 is from Panel M, which has a [-45/-90/-45] midplane stacking sequence. Callout A on Figure 3.25 also shows that the upper edge of the delamination near the midplane extends out in at 45°, while callout B shows the lower edge of that delamination extends towards the boundary conditions at 90°. This shows that in Section 3.1 the shear stress from the impact was following the load path towards the boundary conditions.

3.3 Shadow Delamination Investigation – Backside Scan Comparison

C-scan imaging is 2-D, it gives a top-down view of your damage profile with a contour index to assist in understanding the depth of the different delamination planes. However, these delamination planes are not 2-D, they are 3-D and have unruly geometry. Therefore, in addition to the frontside of the specimens being C-scanned, the backside of nine Panel S specimens were

also C-scanned, three from each energy level. The goal of scanning the backside of nine different Panel S specimens was to get a set of data from one material type that could be used to study the effect of delamination shadowing. Delamination shadowing occurs when larger delaminations that are closer to the scanning surface cause smaller, deeper delaminations to be overshadowed, or hidden, in the C-scan contour plot due to the larger delaminations covering them. This means that the damage profile of a specimen could actually be even more excessive than what the front side C-scan showed. Of the nine specimens that were C-scanned, three have been chosen to be shown in Figure 3.27 through Figure 3.29. Each figure has a photo of the physical specimen alongside the front and backside scan images. To assist in understanding how the specimen has flipped from being scanned on the backside, two features from each scan side have been called out on each image. The full set of nine back side scan images can be found in Appendix IV.

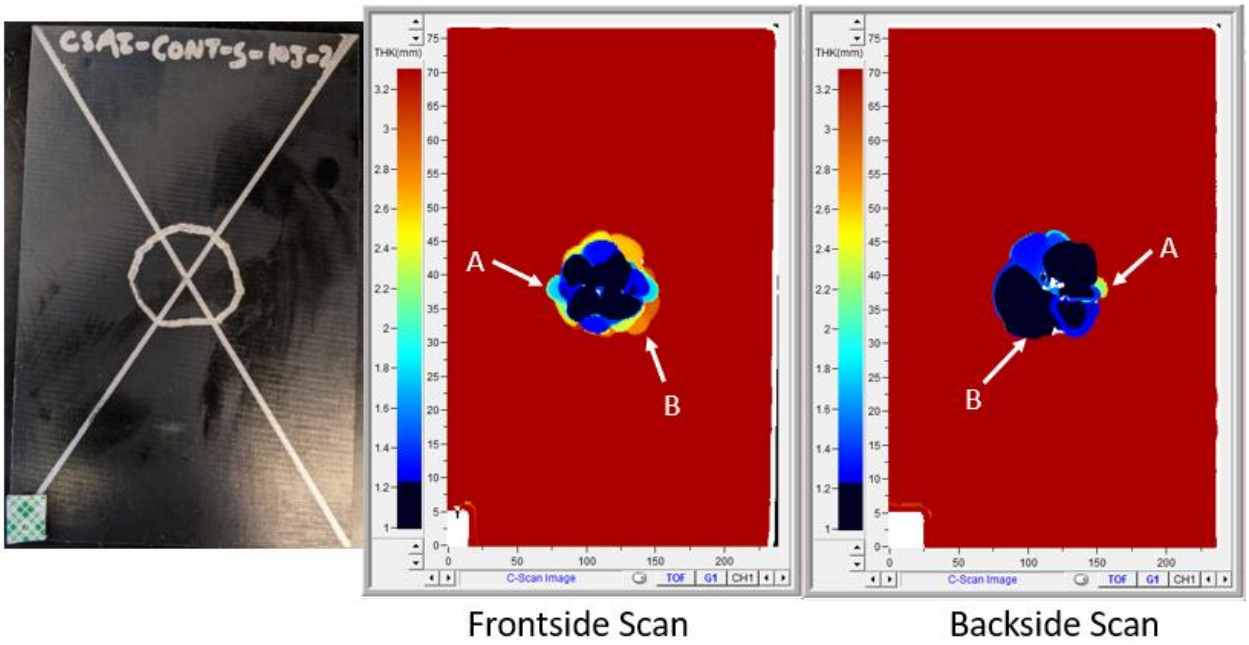

Figure 3.27: Front and Backside C-Scan Images of a 10 J Panel S Specimen.

From Figure 3.27 it is seen that the characteristic bulges from the A and B callouts can be seen in the backside scan as well as the frontside scan. The white region on the backside scan is backside breakout damage from the impact event. In the region below the backside A callout, there is a delamination that is hidden from the frontside scan due to larger delaminations that are closer to the front surface overshadowing that delamination.

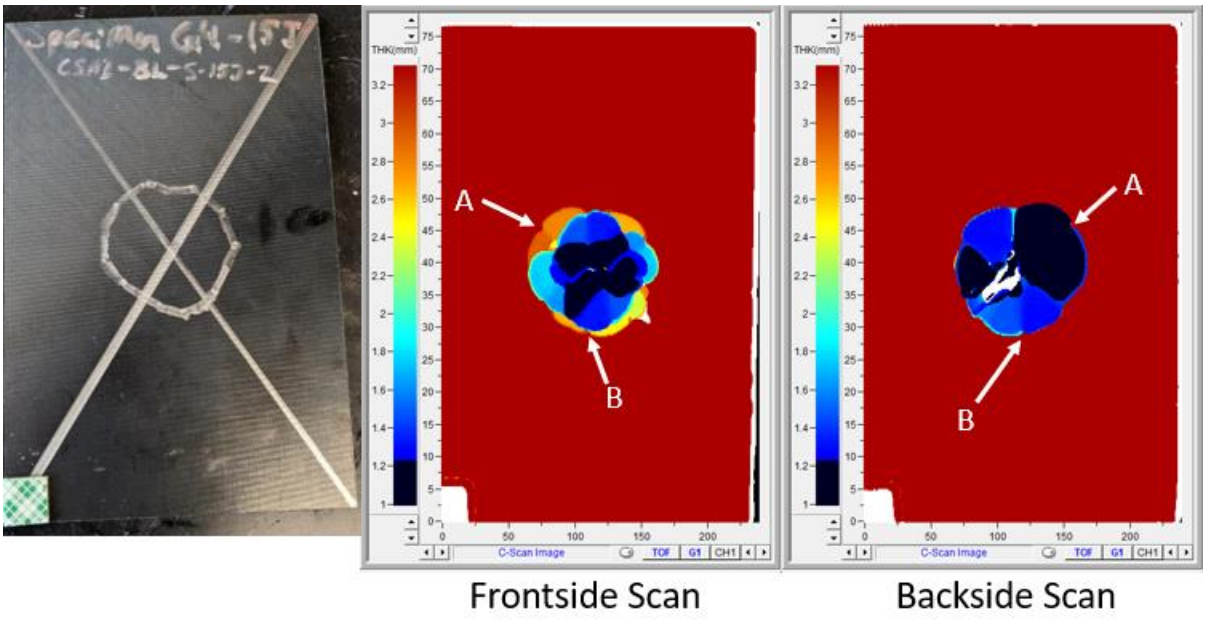

Figure 3.28: Front and Backside C-Scan Images of a 15 J Panel S Specimen.

From Figure 3.28 it is seen that the characteristic divots from the A and B callouts can be seen in the backside scan as well as the frontside scan, albeit a different color indicating the difference in relative depth of the delamination plane from the front or backside surfaces. The white region on the backside scan is backside breakout damage from the impact event. This scan has is similar to the frontside scan, there are no major delaminations that are shadowed on this particular specimen.

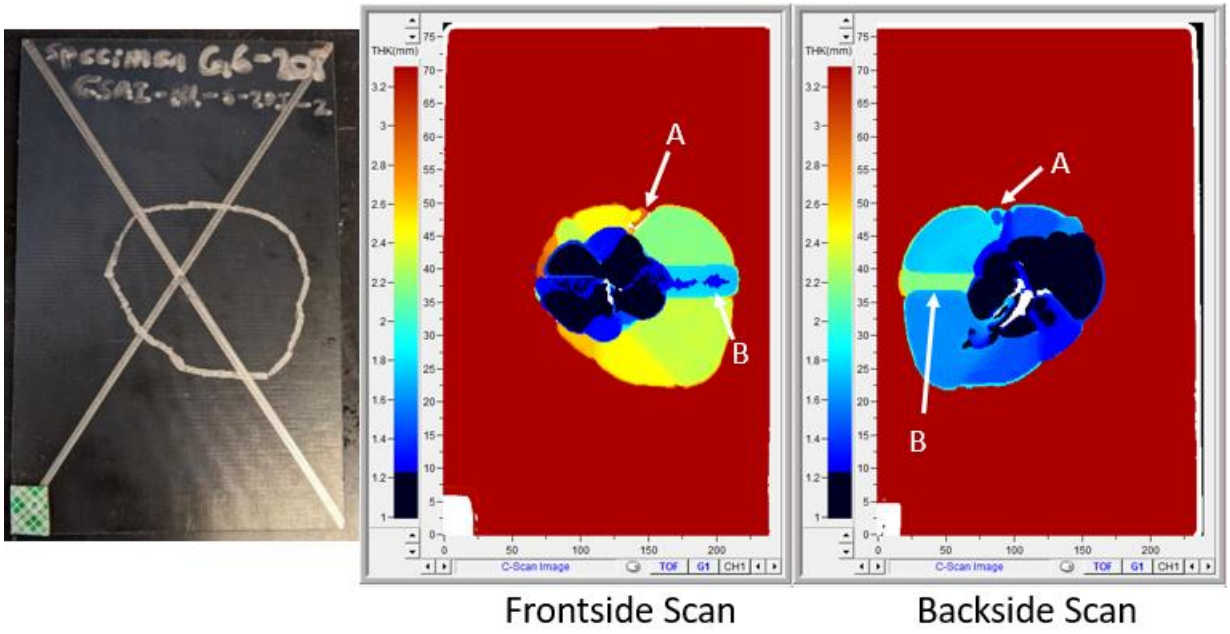

Figure 3.29: Front and Backside C-Scan Images of a 20 J Panel S Specimen.

From Figure 3.29 it is seen that there is a delamination near the back surface that is hidden in the frontside scan due to damage closer to the front surface enveloping it. It can also be seen in the item B callout in that figure that the 90° ply delamination that was discussed in Section 3.2 has a delamination that is spreading underneath it and making that almost rectangular zone appear a bit thinner, which is unable to be seen in the front side scan. The white regions in the center on the frontside scan are dents from the impact event, while the white regions on the backside scan are matrix cracks from backside breakout from the impact event.

These backside scans have shown that by scanning only one side of the specimen, there is further damage that is unable to be seen due to it being in the shadow of the delaminations closer to the surface. These scans will be used in a future project to determine the validity of an algorithm that is presumed to take a frontside scan and predict where further delaminations occur that have been shadowed by the damage closer to the surface.

CHAPTER 4: CONCLUSION AND FUTURE WORKS

The impact of 81 specimens with three varying energy levels and material properties allowed a comprehensive dataset to be generated for force versus time as well as A and C-scan damage investigation plots. The results of this investigation showed that interlaminar shear strength played a large part in the force required for damage to be initiated in the laminate, with the laminate having the lowest amount of 0° plies utilizing its higher amount of 90° plies around the midplane to transfer much of the load to the clamped boundary conditions in the shorter span direction of the impacting test fixture. This allowed the Panel S specimens to withstand a higher load magnitude before becoming damaged, however, this also caused there to be more strain energy in the Panel S specimens when damage did occur, causing more extensive damage. From certain C-scans that contained extensive delamination regions extending towards the clamped regions, delamination zones could be seen to follow the orientation of the plies directly surrounding the midplane of the laminate. The Panel M and Panel H specimens had similar damage size and peak force values, with the damage size being smaller than Panel S and the peak force values being greater than Panel S, due to less strain energy being stored in the panel prior to damage creation.

From the A and C-scans it is seen that while the A-scans are able to adequately be utilized to mark the perimeter of the damage region, the C-scans are much more useful in characterizing the multiplanar damage zones since delamination plane depth information is provided. The C-scans are very detailed and assisted in understanding the data acquired from the impact events. Additional backside scans of nine Panel S specimens showed that while the frontside scans are very useful in determining planes of delamination, they suffer from a shadowing effect that cover delamination regions that are smaller and deeper in the laminate than

delaminations that are closer to the surface. These hidden delamination regions were picked up on the backside scans and while they are smaller than many of the largest delamination zones that hide them, they are still internal voids that can grow if not properly repaired or dealt with. The dataset provided from these studies will be useful in many aspects of research in the future, both experimentally with the impacted and scanned specimens, and serve to provide validation data for modeling impact damage in composite laminates.

4.1 Future Works

The impacted specimens created for this thesis will be used in a PhD students dissertation research on injection repair of delamination regions. The research involves the creation of a novel injection method of epoxy resin with a contamination removal process to ensure proper bonding of the delaminated surfaces. The goal of this injection repair is to return strength to the delaminated specimen to determine if this injection process is able to be considered strength restoring, instead of just cosmetic. The testing will be completed using compression-strength-after-impact testing (CSAI) with repaired specimens compared to damaged, unrepaired specimens to have a quantitative percent of strength restored to the specimen. Initial tests were performed on unrepaired specimens in August 2021. Figure 4.1 shows the Digital Image Correlation (DIC) strain contour overlay on a tested 15 J Panel M specimen during loading.

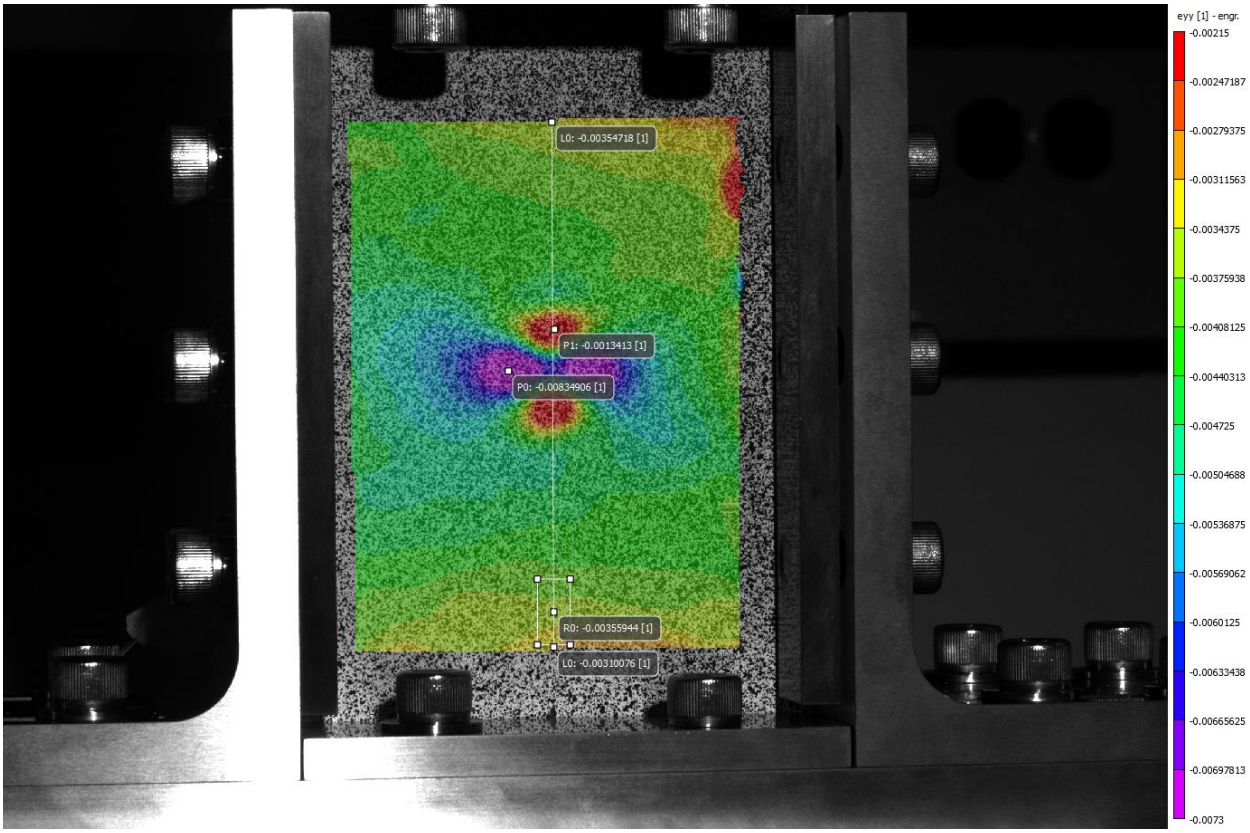

Figure 4.1: CSAI Testing of Unrepaired Panel M 15J Specimen Showing DIC Strain Contour.

A separate study is also being conducted for a separate thesis project to validate a shadow delamination extension code. This code is supposed to use a frontside C-scan and predict shadowed delamination regions and shapes. The researcher will utilize the front scans from this thesis to predict the shadowed delamination regions, they will then compare the predicted shadowed delaminations to the backside scans that were produced in this thesis. The goal being to validate that the shadowed delamination prediction software correctly predicts the shadowed delamination depths and shapes.

REFERENCES

[1] Siow, Y. P., & Shim, V. P. (1998). An experimental study of low velocity impact damage in woven fiber composites. *Journal of Composite Materials*, 32(12), 1178–1202. https://doi.org/10.1177/002199839803201203

[2] Ravikiran, N. K., Venkataramanaiah, A., Bhat, M. R., & Murthy, C. R. L. (2006, December). Detection and evaluation of impact damage in CFRP laminates using ultrasound c-scan and IR thermography. In *National seminar on non-destructive evaluation* (pp. 1-5).

[3] Talreja, R., & Phan, N. (2019). Assessment of damage tolerance approaches for composite aircraft with focus on barely visible impact damage. *Composite Structures*, 219, 1–7. https://doi.org/10.1016/j.compstruct.2019.03.052

[4] Richardson, M. O. W., & Wisheart, M. J. (1996). Review of low-velocity impact properties of composite materials. *Composites Part A: Applied Science and Manufacturing*, 27(12), 1123–1131. https://doi.org/10.1016/1359-835x(96)00074-7

[5] Liu, D., & Malvern, L. E. (1987). Matrix cracking in impacted glass/epoxy plates. *Journal of Composite Materials*, 21(7), 594–609. https://doi.org/10.1177/002199838702100701

[6] Ganesan, R. (2008). Experimental characterization of interlaminar shear strength. In *Delamination Behaviour of Composites* (pp. 117-137). Woodhead Publishing.

[7] Jackson, W. C., & Poe Jr, C. C. (1992, September). The use of impact force as a scale parameter for the impact response of composite laminates. In *FAA, Ninth DOD (NASA) FAA Conference on Fibrous Composites in Structural Design, Volume 2*.

[8] Sjoblom, P. O., Hartness, J. T., & Cordell, T. M. (1988). On low-velocity impact testing of composite materials. *Journal of Composite Materials*, *22*(1), 30–52. https://doi.org/10.1177/002199838802200103

[9] Shen, Q., Omar, M., & Dongri, S. (2011). Ultrasonic nde techniques for impact damage inspection on CFRP laminates. *Journal of Materials Science Research, 1*(1). https://doi.org/10.5539/jmsr.v1n1p2

[10] Misak, L., Corbett, D., & Grantham, M. (2019). Comparison of 2D and 3D ultrasonic pulse echo imaging techniques for structural assessment. *MATEC Web of Conferences, 289*, 06003. https://doi.org/10.1051/matecconf/201928906003

[11] Gordon, G. A., Canumalla, S., & Tittmann, B. R. (1993). Ultrasonic C-scan imaging for Material Characterization. *Ultrasonics, 31*(5), 373–380. https://doi.org/10.1016/0041-624x(93)90071-7

[12] Kim, N., & Achenbach, J. D. (1998). Quantitative characterization of multiple delaminations in laminated composites using the Compton Backscatter Technique. *Journal of Nondestructive Evaluation*, *17*(2), 53–65. https://doi.org/10.1007/bf02995483

[13] Test method for measuring the damage resistance of a fiber-reinforced polymer matrix composite to a drop-weight impact event. (n.d.). https://doi.org/10.1520/d7136_d7136m-15

[14] Prashanth, M., Gouda, P. S., Manjunatha, T. S., Banapurmath, N. R., & Edacheriane, A. (2021). Understanding the impact of fiber orientation on mechanical, interlaminar shear strength, and fracture properties of jute–banana hybrid composite laminates. *Polymer Composites*, *42*(10), 5475–5489. https://doi.org/10.1002/pc.26239

APPENDIX I: PENDULUM IMPACTOR PROCEDURE

The procedures outlined here are the necessary steps to capture data using the Picoscope 6 software package. This procedure is updated from the previous lab pendulum procedure.

1. Set position output switch to “1V”

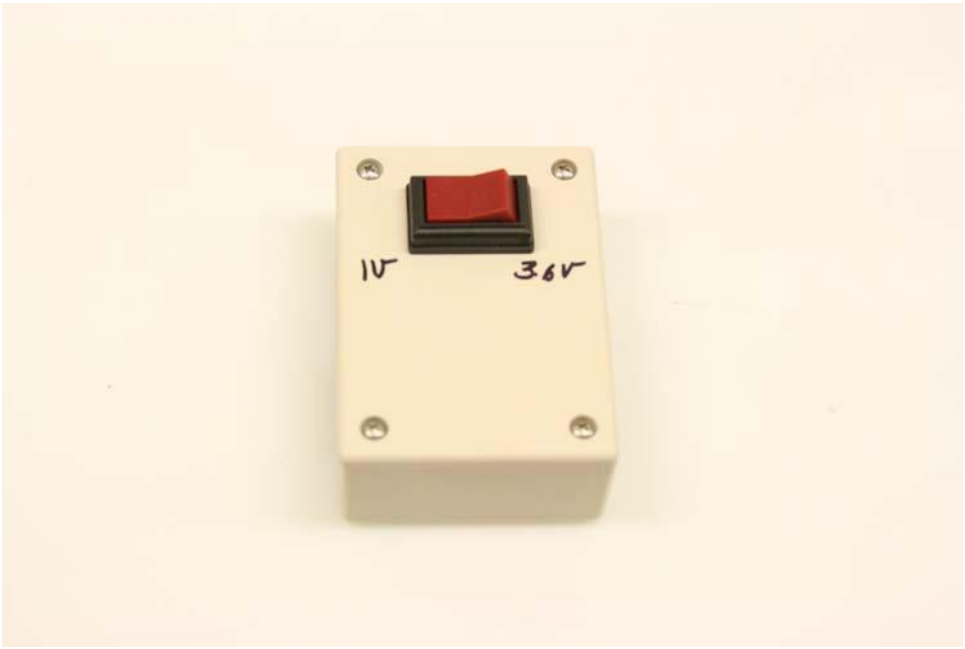

Figure A.1: Position Output Voltage Switch.

2. On computer, launch SEI Explorer (shortcut located on desktop)

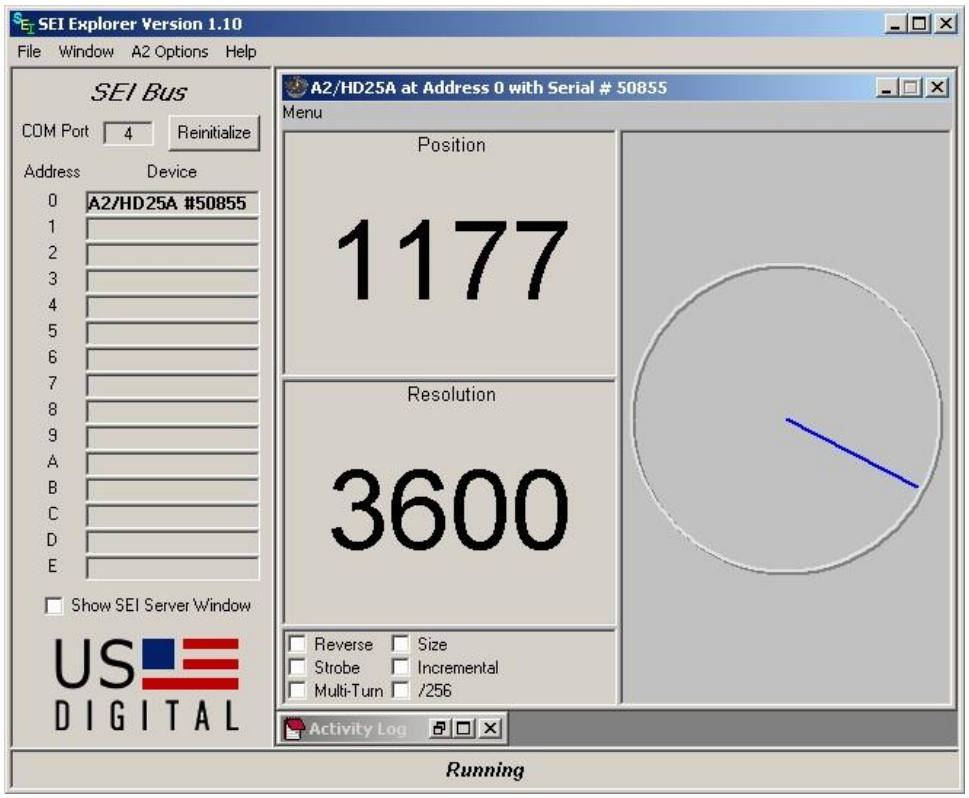

Figure A.2: SEI Screen.

3. Once the user interface has initialized and is reading the encoder position, set the position switch to “3.6V”, if this step was done prio to the SEI user interface loading, there will be a "No device found" error.

4. On computer, launch PicoScope 6 (shortcut located on desktop)

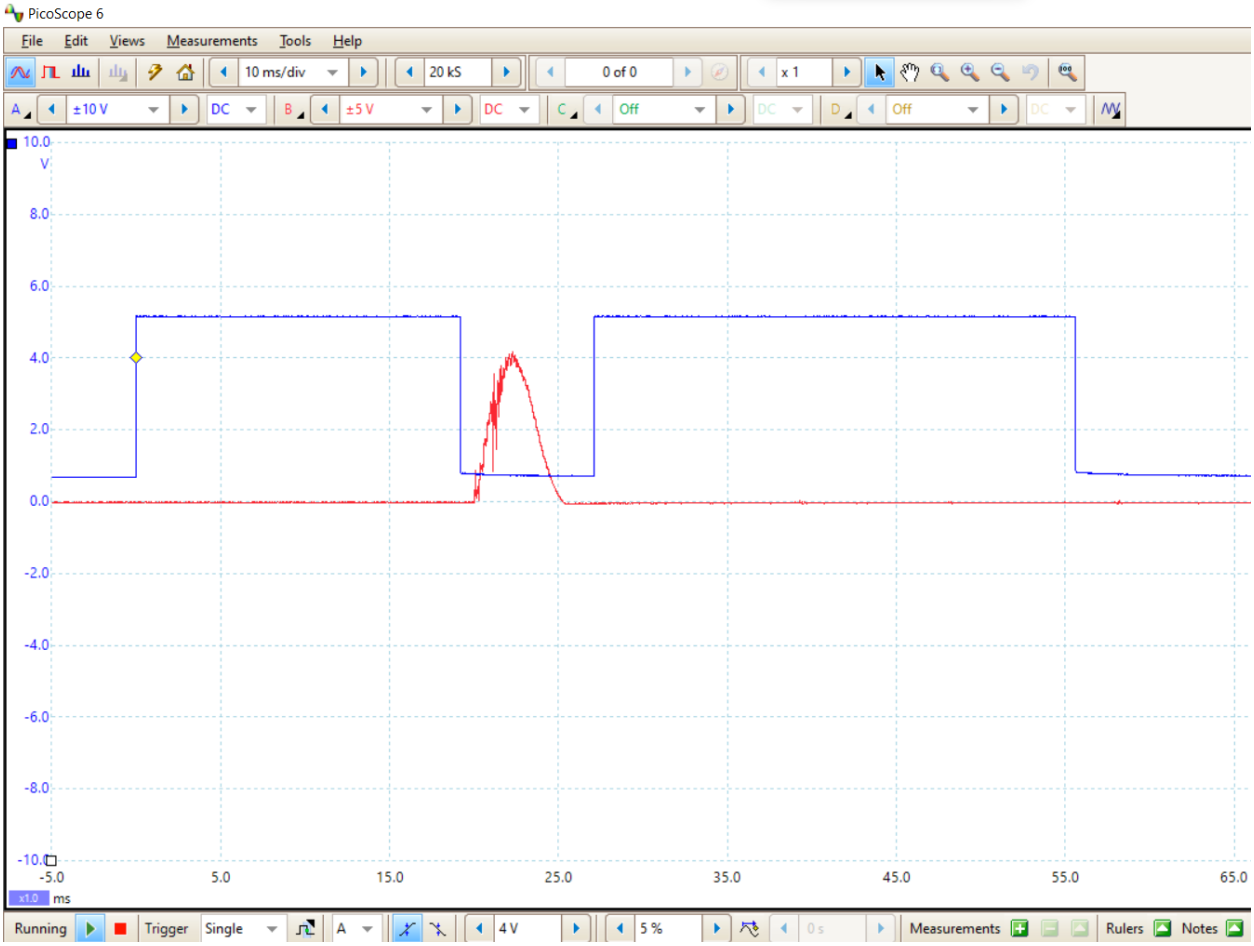

Figure A.3: Picoscope Screen After a Successful Impact.

5. Change the capture values to 10 ms/div, x 1, 1 MS (these values can all be changed based on the impacts being performed, it is recommended that impacts are performed on throwaway specimens to dial in the data capture that is best for that impact study).

6. Go to options > advanced > and set the capture rate to 20000

7. Set the photogate as CH A with a axis of +/- 10 V, set force sensor as CH B and set axis of +/- 2 V (use 2 V for 10 and 15 J impacts, use +/- 5 V for 20 J impacts)

8. Set trigger at Single, CH A, Rising, and 4 V and press the spacebar to begin capturing data (it is recommended to run hand through laser photogate prior to impacting the specimen to make sure that the trigger voltage is set to a correct value that triggers the data collection.

Figure A.5: Bottom of Picoscope.

9. Now able to perform impact study.

10. After capturing data, save the output as a .txt file and as a .psd file.

11. Data acquisition is complete

APPENDIX II: ULTRASONIC SCANNING PROCEDURE

The following procedure was originally produced by Eric Kim but has been updated by Barrett Romasko to show the specific steps used in the Injection Repair project ultrasonic testing.

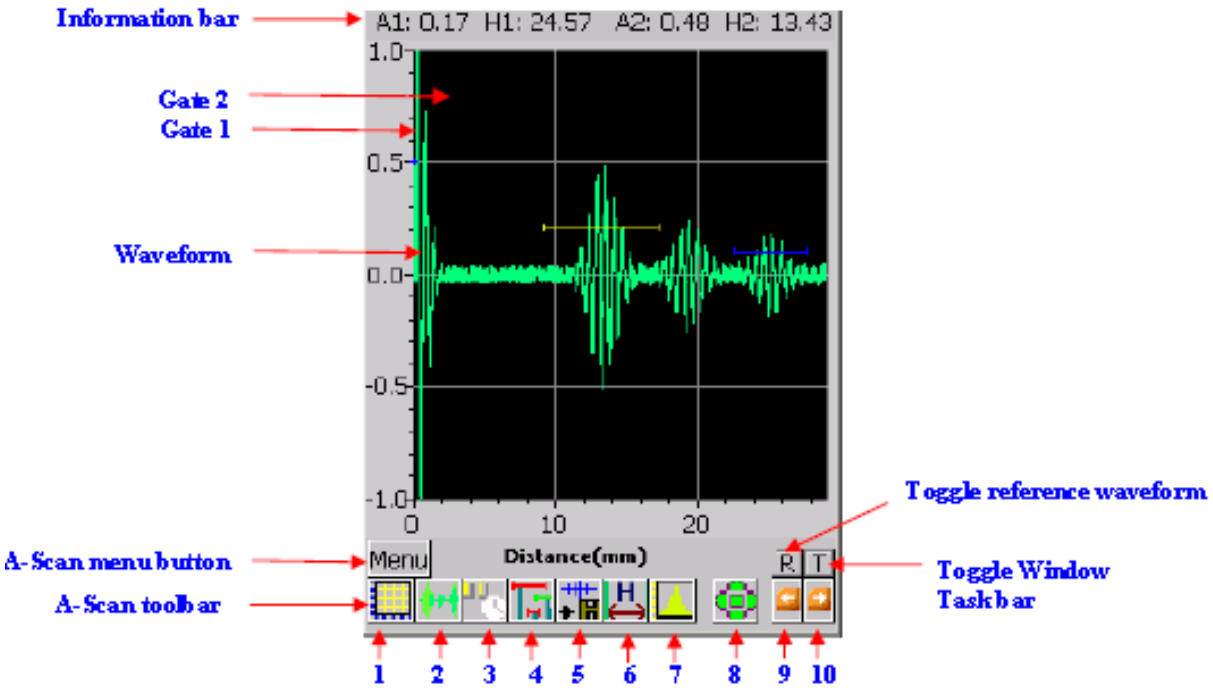

Figure A.6: A-scan Screen.

- A-scan
  1. Check the battery and the memory card are inserted properly, battery is not necessary if the PocketUT device is plugged in for the entire scanning period.
  2. Connect the transducer.
     *** Transducer port is extremely fragile, so leave the angled connector cord connected.**
     a. Angled connector should be connected to P/R already for Pulse-Echo testing.
  3. Disassemble the delay-line from the transducer. Clean the old couplant residue, if any, and apply fresh layer of gel couplant on the transducer and the delay-line interface.
  4. Power on Pocket UT.
  5. Select A-Scan Mode.
  6. Confirm that the signal on the screen is the first reflected signal from the delay-line tip.
     a. Apply small amount of gel couplant on your fingertip and press down the face of the delay-line. Change the x-axis (time/distance) domain as needed to identify the first reflected signal from the delay-line.
  7. Configure Settings
     a. Select A/D hardware settings (2 from the bottom options in Figure 1)
        i. Signal tab

1. Place the transducer on top of the test part coupled with the couplant. Change the Gain so that the peak of the signal is between 80-100% of the screen height.
2. Adjust the Delay and Width to well-identify the reflected signals from the front and back surface reflected waves.

ii. Filter tab
1. Adjust LP and HP filter that gives best SNR and make sure the range contains the transducer's operating frequency.

iii. Rect
1. Select the desired waveform. Full Rectification recommended.

b. Select DAC and P/R Settings (3 from the bottom options in Figure 1)
i. P/R tab → P/R, 400V and Low damping
ii. Pulser tab → Tone Burst, Frequency of the transducer, 1 cycle

- C-scan

1. Ensure DI water inside the tank is clean. If not, clean and re-fill the immersion tank with fresh DI water.
2. Screw in the transducer.
3. Place the part into the tank and affix the transducer at the distance of manufacturer's recommended focal distance.
    a. ONR Project: Use FR4 scrap piece next to immersion tank to set transducer a distance of 1 inch from the panel
4. Pocket UT → Pull-out the battery. Insert the memory card. Connect the angled connector to the yellow BNC from the XY controller. Connect the Pocket UT charging cable and power it on.
5. Select Scanner
    a. Automatic Scan → AS-XY
6. Turn on the XY controller.
7. Go back to the main menu and Select A-scan.
8. Select toggle motion control bar (8 from the bottom options in Figure 1)
9. Carefully move the scanner so the transducer is place perpendicular to the test part.

*Pay careful attention not to collide the scanner to its frame.

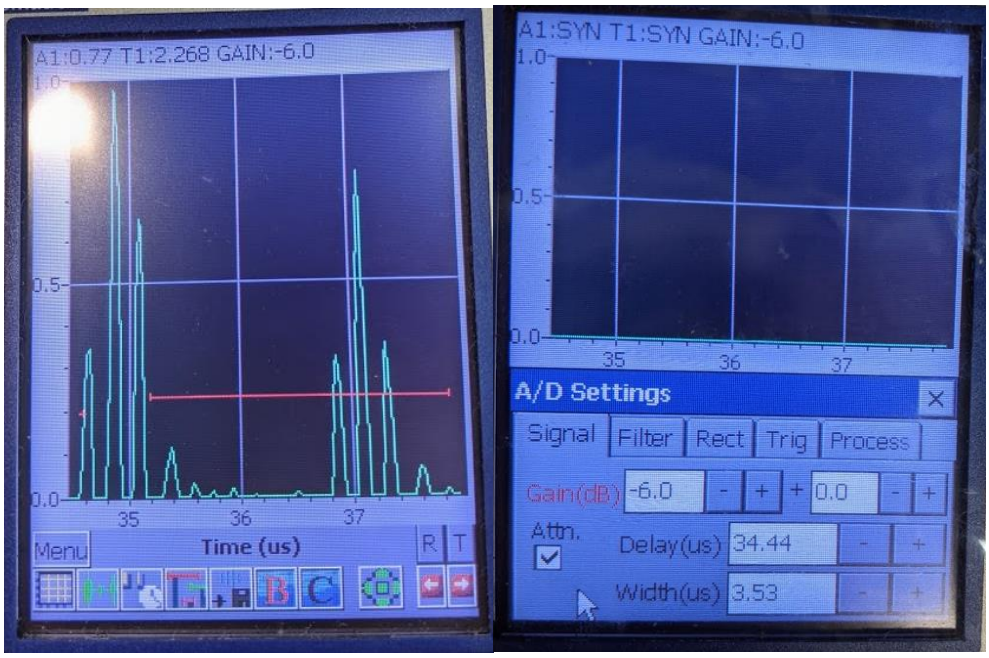

Figure A.7: A-scan Window and Signal Settings

10. Perform 6 and 7 of A-scan procedure.
    a. You can neglect any of the couplant related procedure, but ensure that focused transducer's face is free of air bubble blocking the wave path.
    b. Select Gate settings (4 from the bottom options in Figure 1)
        i. Change the gate sync, start, width, threshold, etc., to encompass domain after the front surface reflected signal and the back surface reflected signal.
11. Go back to the main menu and Select C-scan.
    a. Select Toggle motion control bar (7 from the bottom options of C-scan mode)
        i. Move the scanner to the desired Start point. Set as home

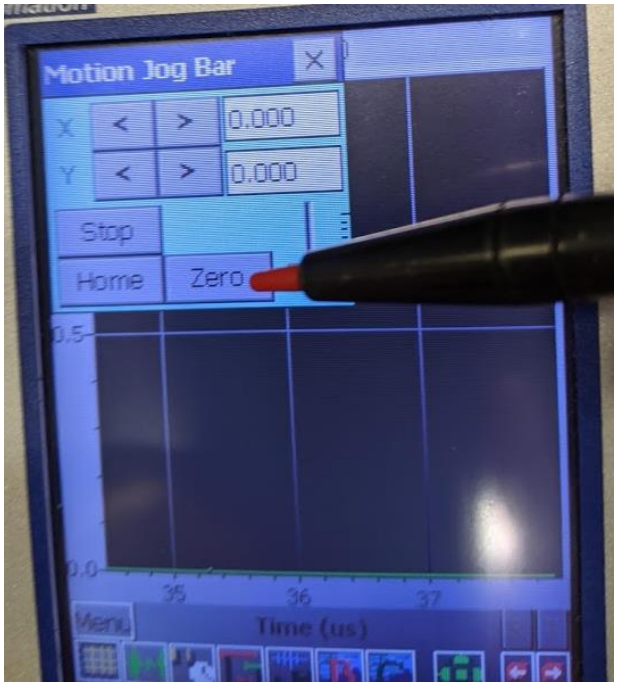

Figure A.8: Location of Home and Zero Buttons.

ii. Move the scanner to the End point Record the values
    1. (77,238) for ONR Project (X,Y) [we scan Y, index X]

b. C-scan Settings (2 from the bottom options of C-scan mode)
    i. Scan Axis → Enter the recorded X value in Length
        1. Y axis from 0 to 238 for ONR
    ii. Index Axis → Enter the recorded Y value in Length
        1. X axis from 0 to 77 for ONR
c. Start C-scan (5 from the bottom options of C-scan mode) (looks like green light on traffic light)
d. Data save (6 from the bottom options of C-scan mode)
    i. Save in csc file to post analyze the data using UTWin.

*Go back to the Main Menu and Exit the program when done. Otherwise, scanned data may not properly save on to the memory card.

APPENDIX III: CALCULATIONS FROM IMPACT EVENT DATA

The incoming and outgoing velocity of the pendulum impactor was determined via experimental calculations. The Picoscope data acquired from the laser photogate as well as from the Dytran force sensor from a representative impact study can be seen in Figure A.1. To calculate the velocity, the time for the pendulum to fully pass through the laser photogate was taken from the picoscope reading and then the pendulum mass (m) was divided by that time (s) to calculate the velocity as seen in Equation (A1).

$$v = m/s \tag{A1}$$

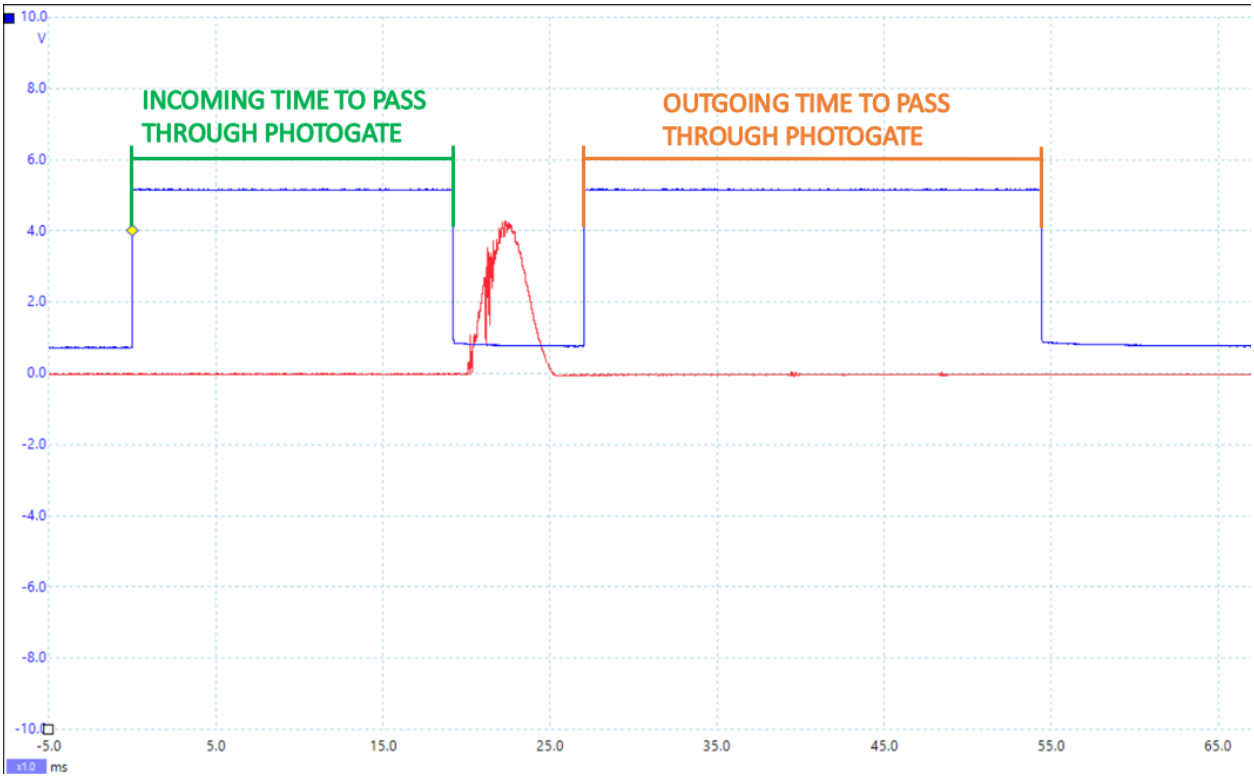

Figure A.9: Picoscope DAQ Impact Force and Photogate Time Data.

That velocity was then used to calculate the incoming and outgoing kinetic energy using Equation (A2).

$$KE = 0.5 * m * v^2 \tag{A2}$$

The amount of energy absorbed in the impact was determined by taking the difference between the incoming and outgoing energies, as seen in Equation (A3).

$$KE_{absorbed} = KE_{in} - KE_{out} \tag{A3}$$

These calculations were used in the following data tables for all of the specimens.

Panel H Data Table

Samples Set	Impact Energy	Impact Velocity (m/s)	Exit Velocity (m/s)	Max Force (kN)	KE in (J)	KE out (J)	Energy Absorbed (J)	Normalized Energy Absorbtion	Max Damage Diameter (mm)	Max Damage Area (mm^2)	Damage Onset Force (kN)
CSAI-BL-H-10J-1	10	2.05	1.37	6.92	10.12	4.52	5.60	0.55	N/A	N/A	6.5
CSAI-BL-H-10J-2	10	2.04	1.39	6.58	9.97	4.66	5.30	0.53	41.00	1320.25	6
CSAI-BL-H-10J-3	10	2.04	1.41	6.48	9.97	4.79	5.17	0.52	40.00	1256.64	5.8
CSAI-RPR-H-10J-1	10	2.04	1.36	6.58	10.02	4.46	5.56	0.55	37.00	1075.21	6.5
CSAI-RPR-H-10J-2	10	2.04	1.41	7.08	9.97	4.75	5.22	0.52	38.00	1134.11	6.05
CSAI-RPR-H-10J-3	10	2.05	1.42	6.69	10.07	4.85	5.22	0.52	36.00	1017.88	6.8
CSAI-CONT-H-10J-1	10	2.04	1.41	6.61	10.02	4.79	5.22	0.52	34.00	907.92	5.8
CSAI-CONT-H-10J-2	10	2.04	1.41	7.16	10.02	4.76	5.26	0.52	33.00	855.30	5.75
CSAI-CONT-H-10J-3	10	2.04	1.40	5.86	9.97	4.70	5.27	0.53	35.00	962.11	5.25
CSAI-BL-H-15J-1	15	2.50	1.74	5.46	14.99	7.26	7.73	0.52	42.00	1385.44	N/A
CSAI-BL-H-15J-2	15	2.51	1.75	5.61	15.08	7.36	7.73	0.51	43.00	1452.20	N/A
CSAI-BL-H-15J-3	15	2.51	1.74	5.61	15.08	7.26	7.82	0.52	53.00	2206.18	N/A
CSAI-RPR-H-15J-1	15	2.50	1.77	5.28	14.99	7.49	7.50	0.50	43.00	1452.20	N/A
CSAI-RPR-H-15J-2	15	2.50	1.75	4.91	14.99	7.39	7.60	0.51	48.00	1809.56	N/A
CSAI-RPR-H-15J-3	15	2.50	1.76	4.80	14.99	7.42	7.57	0.50	44.00	1520.53	N/A
CSAI-CONT-H-15J-1	15	2.51	1.76	7.94	15.08	7.42	7.66	0.51	38.00	1134.11	6.2
CSAI-CONT-H-15J-2	15	2.51	1.78	8.20	15.08	7.62	7.47	0.50	42.00	1385.44	5.75
CSAI-CONT-H-15J-3	15	2.51	1.77	7.95	15.08	7.52	7.56	0.50	43.00	1452.20	5.95
CSAI-BL-H-20J-1	20	3.05	2.06	9.33	22.37	10.17	12.19	0.55	50.00	1963.50	6.25
CSAI-BL-H-20J-2	20	2.92	2.05	9.28	20.52	10.07	10.45	0.51	51.00	2042.82	6.33
CSAI-BL-H-20J-3	20	2.89	1.97	9.19	20.08	9.35	10.73	0.53	63.00	3117.25	6.15
CSAI-RPR-H-20J-1	20	2.89	1.98	9.04	20.08	9.44	10.64	0.53	64.00	3216.99	6.2
CSAI-RPR-H-20J-2	20	2.89	2.04	9.60	20.08	9.97	10.11	0.50	45.00	1590.43	6.05
CSAI-RPR-H-20J-3	20	2.89	1.95	9.28	20.08	9.12	10.95	0.55	64.00	3216.99	6.1
CSAI-CONT-H-20J-1	20	2.89	2.00	9.10	20.08	9.62	10.45	0.52	59.00	2733.97	6.05
CSAI-CONT-H-20J-2	20	2.89	2.03	9.56	20.08	9.87	10.20	0.51	57.00	2551.76	6
CSAI-CONT-H-20J-3	20	2.89	2.04	9.54	20.08	10.02	10.06	0.50	43.00	1452.20	6.1

Panel M Data Table

Samples Set	Impact Energy	Impact Velocity (m/s)	Exit Velocity (m/s)	Max Force (kN)	KE in (J)	KE out (J)	Energy Absorbed (J)	Normalized Energy Absorbtion	Max Damage Diameter (mm)	Max Damage Area (mm^2)	Damage Onset Force (kN)
CSAI-BL-M-10J-1	10	2.06	1.38	6.60	10.17	4.55	5.62	0.55	37.00	1075.21	6.1
CSAI-BL-M-10J-2	10	2.06	1.38	6.89	10.17	4.55	5.62	0.55	28.00	615.75	6.1
CSAI-BL-M-10J-3	10	2.06	1.37	7.07	10.17	4.54	5.64	0.55	29.00	660.52	6.2
CSAI-RPR-M-10J-1	10	1.94	1.33	6.83	9.08	4.24	4.84	0.53	34.00	907.92	5.9
CSAI-RPR-M-10J-2	10	1.94	1.32	7.85	9.08	4.17	4.91	0.54	34.00	907.92	6.1
CSAI-RPR-M-10J-3	10	1.94	1.34	6.56	9.08	4.28	4.79	0.53	36.00	1017.88	5.9
CSAI-CONT-M-10J-1	10	1.94	1.33	6.98	9.08	4.22	4.86	0.54	36.00	1017.88	5.8
CSAI-CONT-M-10J-2	10	1.94	1.31	6.29	9.08	4.15	4.93	0.54	40.00	1256.64	6.1
CSAI-CONT-M-10J-3	10	2.06	1.40	6.98	10.17	4.70	5.48	0.54	31.00	754.77	6.1
CSAI-BL-M-15J-1	**15**	2.50	1.72	7.88	14.99	7.11	7.88	0.53	N/A	N/A	6.5
CSAI-BL-M-15J-2	**15**	2.50	1.74	8.04	14.99	7.23	7.76	0.52	N/A	N/A	6.33
CSAI-BL-M-15J-3	**15**	2.50	1.75	7.85	14.99	7.32	7.67	0.51	N/A	N/A	6.05
CSAI-RPR-M-15J-1	**15**	2.37	1.65	7.89	13.45	6.56	6.88	0.51	47.00	1734.94	6.2
CSAI-RPR-M-15J-2	**15**	2.49	1.74	8.32	14.90	7.26	7.63	0.51	45.00	1590.43	6.15
CSAI-RPR-M-15J-3	**15**	2.50	1.75	8.50	14.99	7.39	7.60	0.51	46.00	1661.90	6.15
CSAI-CONT-M-15J-1	**15**	2.50	1.75	8.56	14.99	7.32	7.67	0.51	44.00	1520.53	6.05
CSAI-CONT-M-15J-2	**15**	2.50	1.75	8.67	14.99	7.32	7.67	0.51	43.00	1452.20	6.1
CSAI-CONT-M-15J-3	**15**	2.50	1.74	7.96	14.99	7.29	7.70	0.51	40.00	1256.64	6.2
CSAI-BL-M-20J-1	20	2.87	1.94	8.71	19.81	8.99	10.82	0.55	63.00	3117.25	6.2
CSAI-BL-M-20J-2	20	2.87	2.00	9.41	19.81	9.58	10.23	0.52	50.00	1963.50	6.25
CSAI-BL-M-20J-3	20	2.87	2.01	9.31	19.81	9.72	10.08	0.51	45.00	1590.43	6.8
CSAI-RPR-M-20J-1	20	2.87	2.00	10.16	19.81	9.62	10.18	0.51	58.00	2642.08	6.15
CSAI-RPR-M-20J-2	20	2.87	2.01	10.47	19.81	9.72	10.08	0.51	49.00	1885.74	6.25
CSAI-RPR-M-20J-3	20	2.87	1.95	9.52	19.81	9.16	10.64	0.54	70.00	3848.45	6.1
CSAI-CONT-M-20J-1	20	2.87	1.94	9.70	19.79	8.99	10.79	0.55	69.00	3739.28	6.2
CSAI-CONT-M-20J-2	20	2.87	1.92	10.03	19.81	8.82	10.99	0.55	66.00	3421.19	6.1
CSAI-CONT-M-20J-3	20	2.87	2.01	8.89	19.81	9.72	10.08	0.51	47.00	1734.94	6.05

Panel S Data Table

Samples Set	Impact Energy	Impact Velocity (m/s)	Exit Velocity (m/s)	Max Force (kN)	KE in (J)	KE out (J)	Energy Absorbed (J)	Normalized Energy Absorbtion	Max Damage Diameter (mm)	Max Damage Area (mm^2)	Damage Onset Force (kN)
CSAI-BL-S-10J-1	10	2.05	1.35	7.00	10.12	4.36	5.76	0.57	39.00	1194.59	6.5
CSAI-BL-S-10J-2	***10***	2.05	1.37	7.00	10.12	4.49	5.63	0.56	39.00	1194.59	6.33
CSAI-BL-S-10J-3	10	2.05	1.35	6.47	10.07	4.37	5.70	0.57	55.00	2375.83	6.5
CSAI-RPR-S-10J-1	10	2.04	1.40	7.00	9.97	4.71	5.25	0.53	36.00	1017.88	6.15
CSAI-RPR-S-10J-2	***10***	2.04	1.37	7.84	9.97	4.52	5.45	0.55	34.00	907.92	6.5
CSAI-RPR-S-10J-3	10	2.05	1.37	7.48	10.12	4.52	5.60	0.55	38.00	1134.11	6.5
CSAI-CONT-S-10J-1	10	2.08	1.39	7.01	10.39	4.62	5.77	0.56	38.00	1134.11	6.66
CSAI-CONT-S-10J-2	***10***	2.08	1.38	7.79	10.39	4.60	5.79	0.56	36.00	1017.88	6.5
CSAI-CONT-S-10J-3	10	2.08	1.37	6.89	10.39	4.52	5.87	0.56	44.00	1520.53	6.75
CSAI-BL-S-15J-1	15	2.49	1.70	7.74	14.90	6.96	7.94	0.53	51.00	2042.82	6.66
CSAI-BL-S-15J-2	***15***	2.50	1.69	7.93	14.99	6.84	8.15	0.54	45.00	1590.43	6.25
CSAI-BL-S-15J-3	15	2.51	N/A	7.82	15.08	N/A	N/A	N/A	47.00	1734.94	6.75
CSAI-RPR-S-15J-1	15	2.50	N/A	8.00	14.99	N/A	N/A	N/A	67.00	3525.65	5.9
CSAI-RPR-S-15J-2	***15***	2.50	N/A	7.79	15.03	N/A	N/A	N/A	55.00	2375.83	6.25
CSAI-RPR-S-15J-3	15	2.51	1.69	7.76	15.08	6.84	8.24	0.55	62.00	3019.07	6.5
CSAI-CONT-S-15J-1	15	2.51	1.64	8.02	15.17	6.43	8.73	0.58	66.00	3421.19	6.5
CSAI-CONT-S-15J-2	***15***	2.51	1.69	8.29	15.17	6.87	8.30	0.55	47.00	1734.94	6.5
CSAI-CONT-S-15J-3	15	2.51	1.71	8.48	15.17	7.05	8.12	0.54	47.00	1734.94	6.5
CSAI-BL-S-20J-1	20	2.90	1.94	8.76	20.22	9.04	11.19	0.55	63.00	3117.25	6.4
CSAI-BL-S-20J-2	***20***	2.89	1.91	8.66	20.08	8.74	11.34	0.56	65.00	3318.31	6.5
CSAI-BL-S-20J-3	20	2.89	1.91	9.25	20.08	8.78	11.29	0.56	72.00	4071.50	6.5
CSAI-RPR-S-20J-1	20	2.89	1.88	9.30	20.08	8.49	11.58	0.58	80.00	5026.55	6.5
CSAI-RPR-S-20J-2	***20***	2.89	1.90	9.08	20.08	8.66	11.42	0.57	89.00	6221.14	6.8
CSAI-RPR-S-20J-3	20	2.89	1.91	9.19	20.08	8.78	11.29	0.56	74.00	4300.84	6.5
CSAI-CONT-S-20J-1	20	2.89	1.91	8.81	20.08	8.78	11.29	0.56	87.00	5944.68	6.75
CSAI-CONT-S-20J-2	***20***	2.89	1.86	8.74	20.08	8.26	11.81	0.59	88.00	6082.12	6.75
CSAI-CONT-S-20J-3	20	2.89	1.90	9.33	20.08	8.66	11.42	0.57	74.00	4300.84	6.5

Panel H 10 J

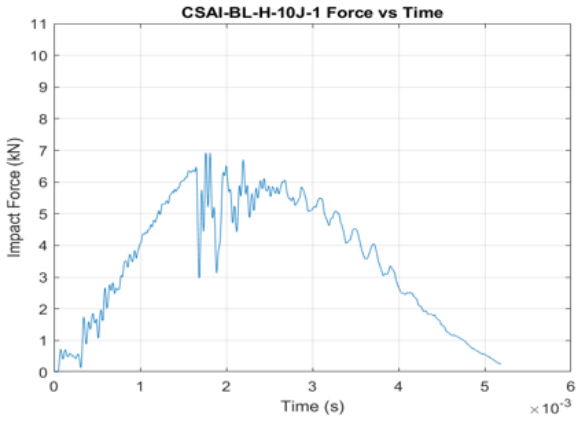
CSAI-BL-H-10J-1 Force vs Time
Impact Force (kN)
Time (s)
×10^-3

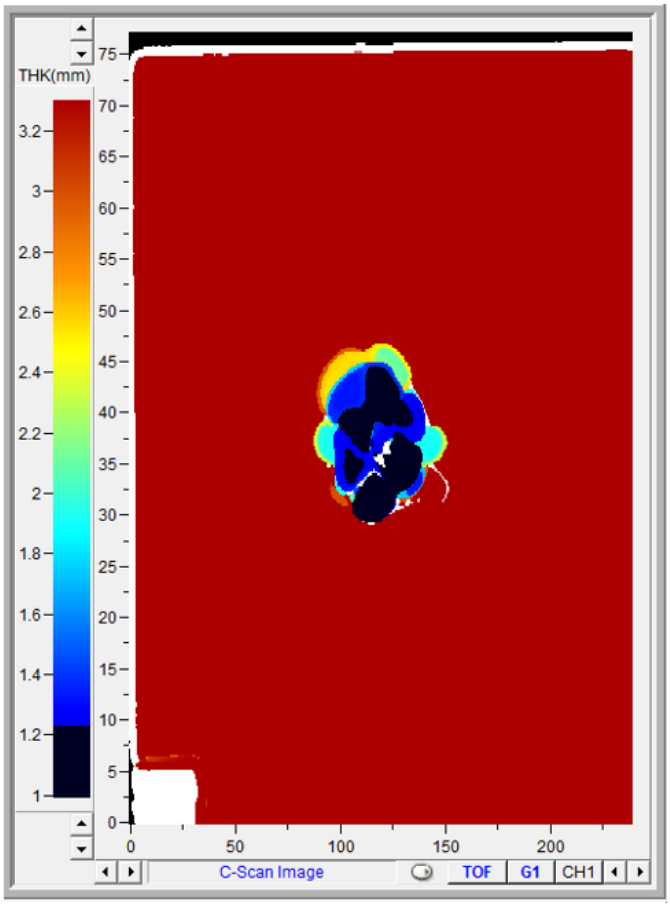
THK(mm)
C-Scan Image
TOF
G1
CH1

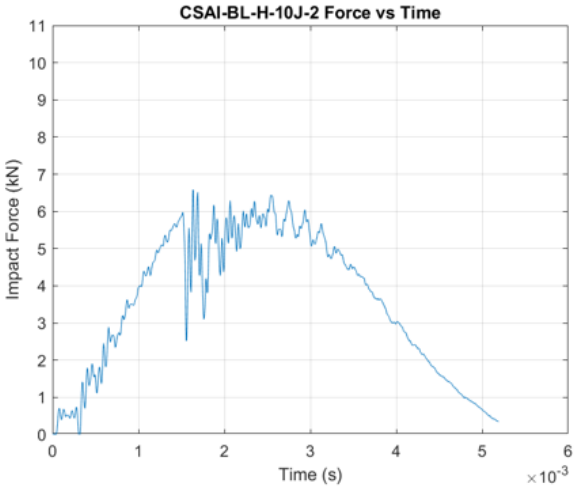
CSAI-BL-H-10J-2 Force vs Time
Impact Force (kN)
Time (s)
×10^-3

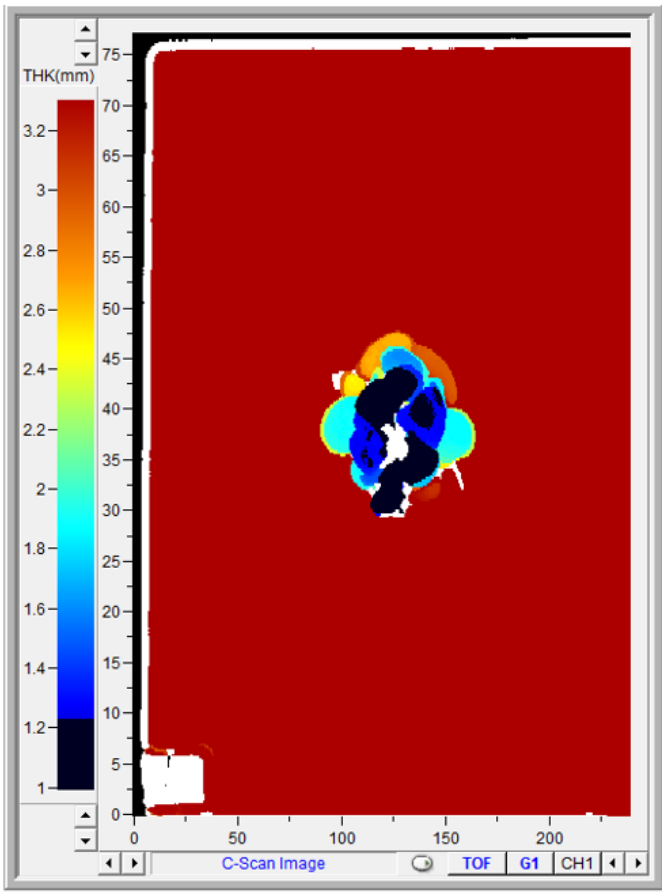
THK(mm)
C-Scan Image
TOF
G1
CH1

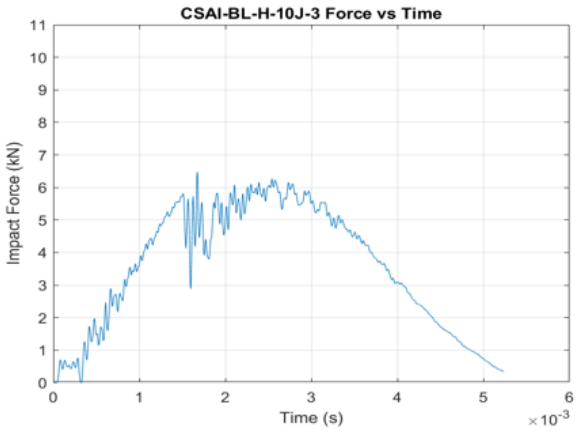
CSAI-BL-H-10J-3 Force vs Time
Impact Force (kN)
Time (s)
×10^-3

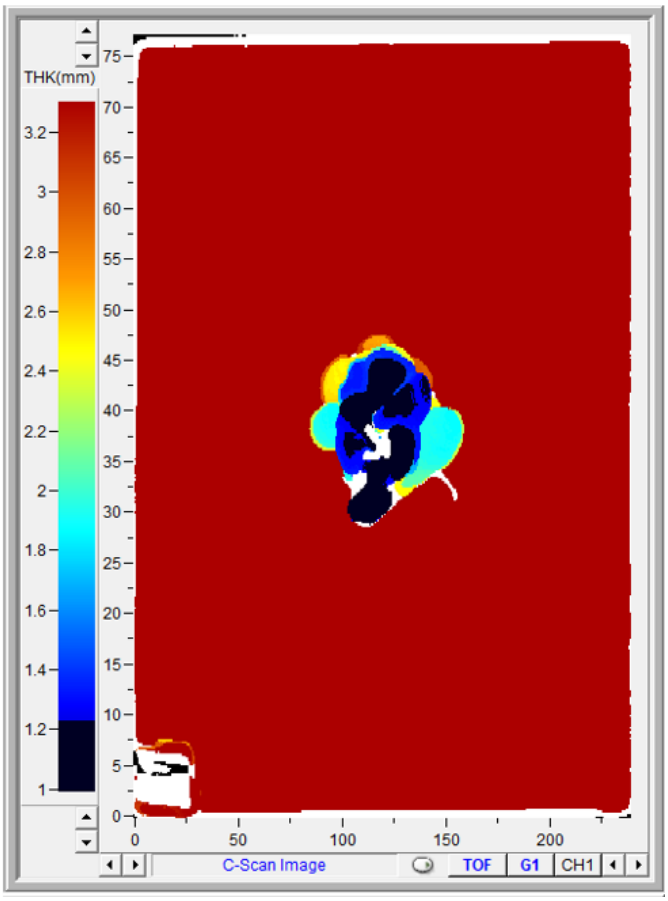
THK(mm)
C-Scan Image
TOF
G1
CH1

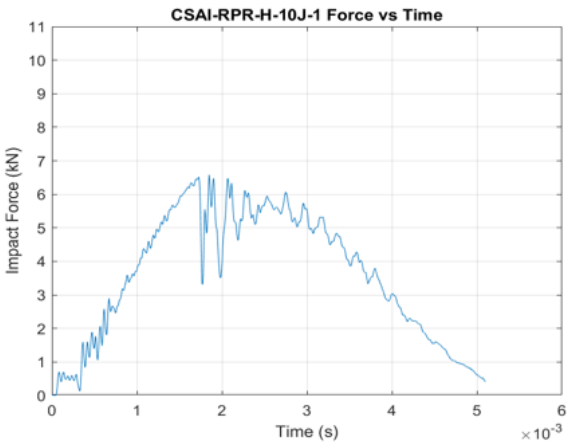
CSAI-RPR-H-10J-1 Force vs Time
Impact Force (kN)
Time (s)
×10^-3

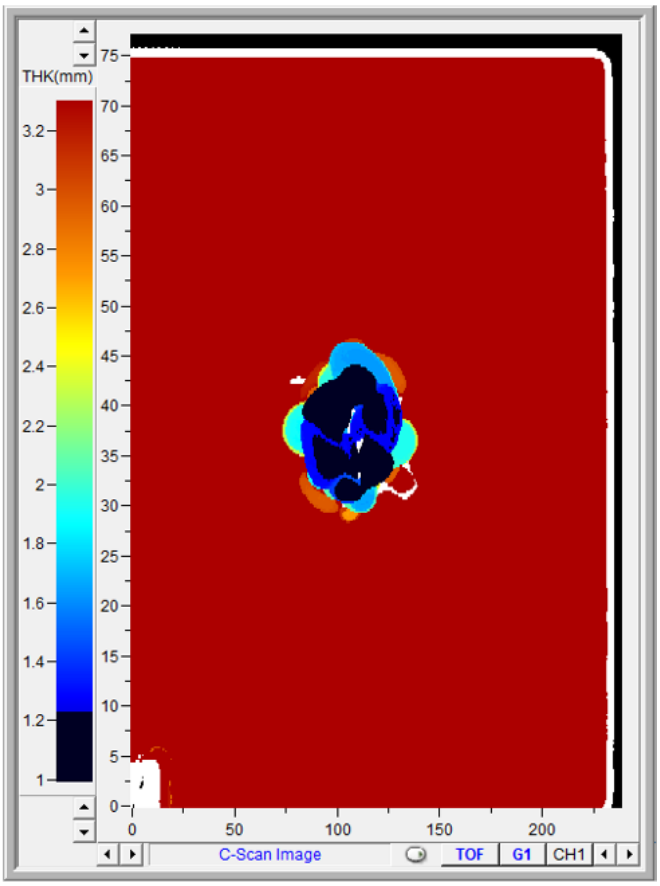
THK(mm)
C-Scan Image
TOF
G1
CH1

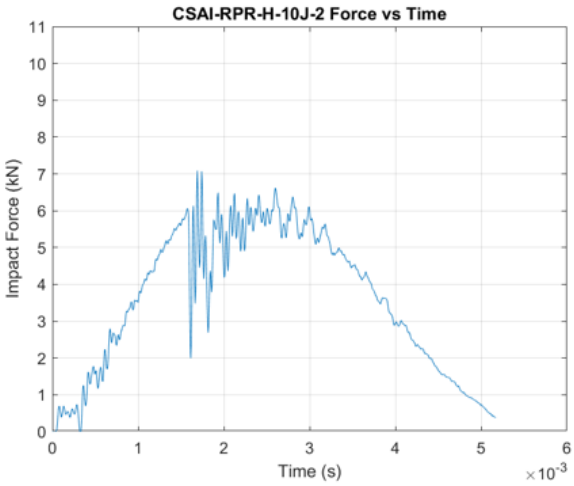
CSAI-RPR-H-10J-2 Force vs Time
Impact Force (kN)
Time (s)
×10^-3

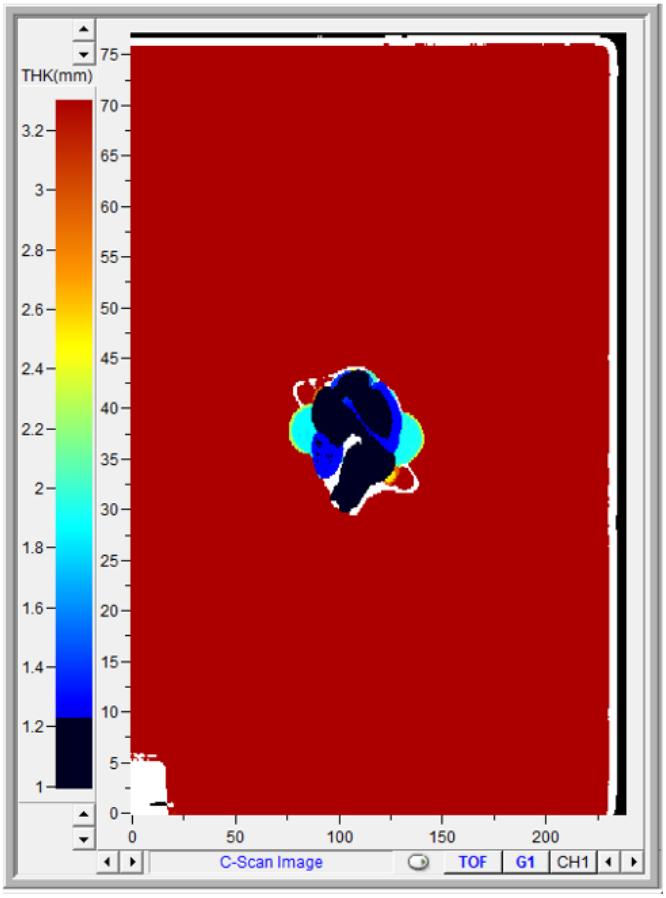
THK(mm)
C-Scan Image
TOF
G1
CH1

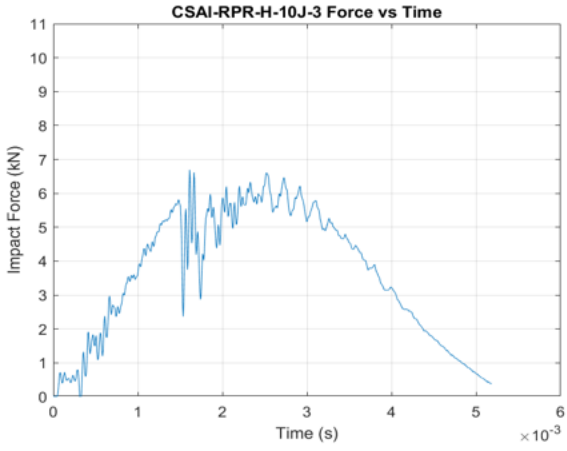
CSAI-RPR-H-10J-3 Force vs Time
Impact Force (kN)
Time (s)
×10^-3

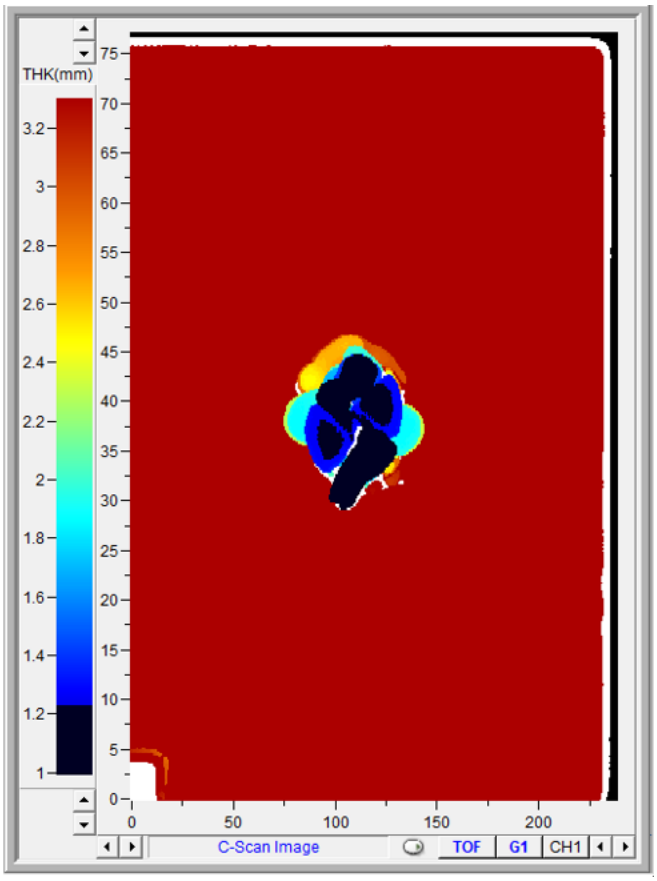
THK(mm)
C-Scan Image
TOF
G1
CH1

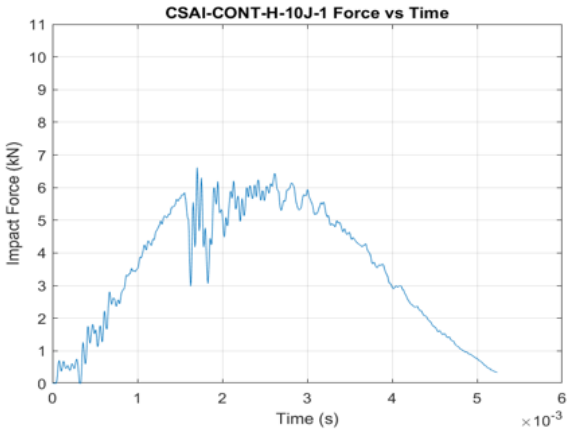
CSAI-CONT-H-10J-1 Force vs Time
Impact Force (kN)
Time (s)
×10^-3

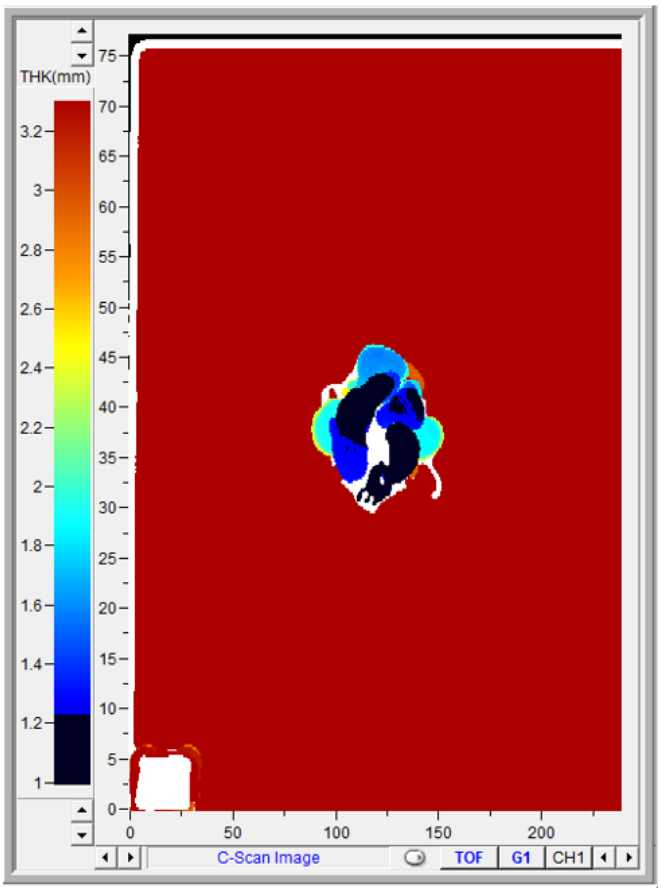
THK(mm)
C-Scan Image
TOF
G1
CH1

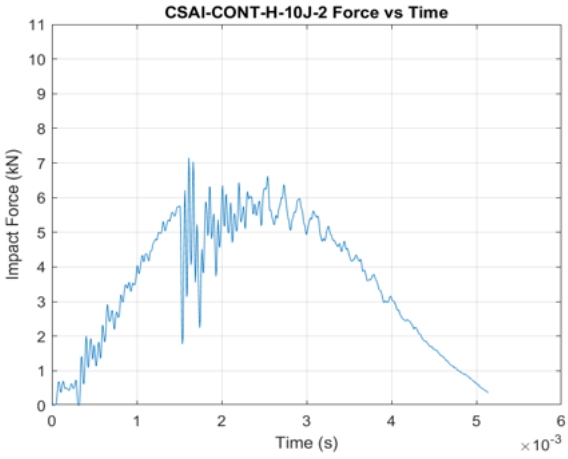
CSAI-CONT-H-10J-2 Force vs Time
Impact Force (kN)
Time (s)
×10^-3

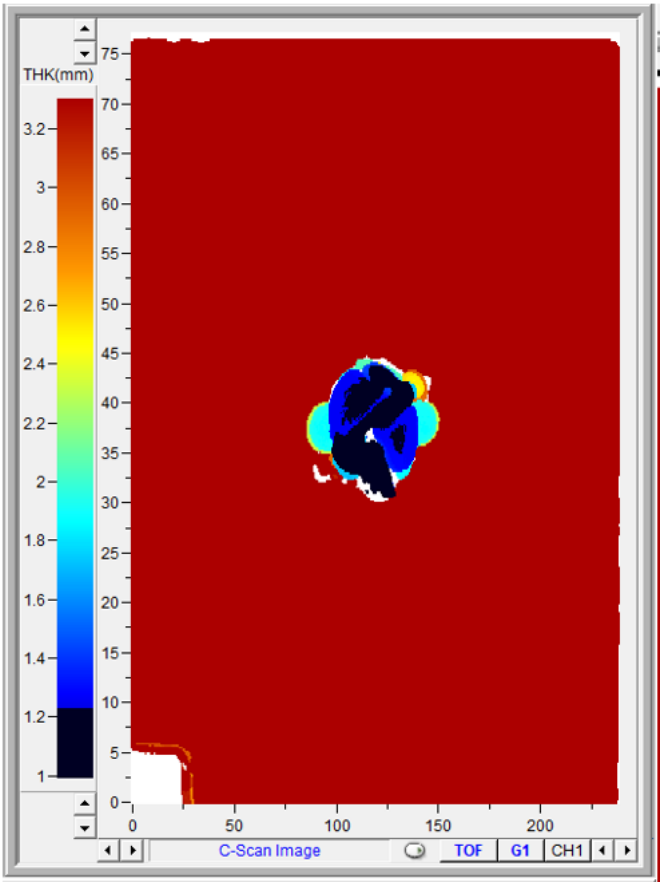
THK(mm)
C-Scan Image
TOF
G1
CH1

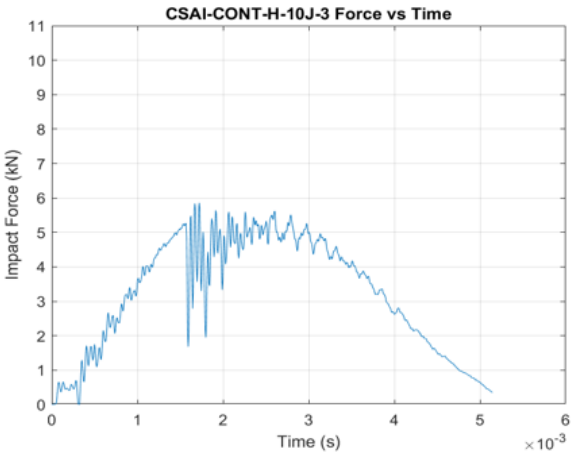
CSAI-CONT-H-10J-3 Force vs Time
Impact Force (kN)
Time (s)
×10^-3

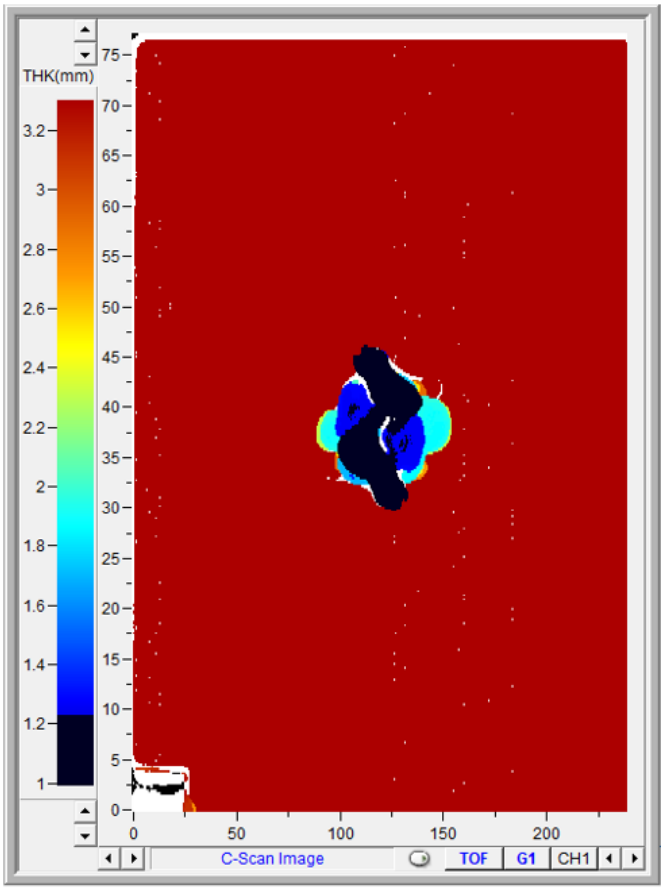
THK(mm)
C-Scan Image
TOF
G1
CH1

Panel M 10 J

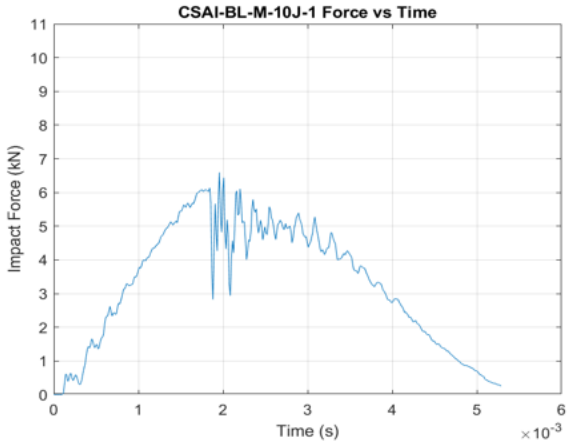
CSAI-BL-M-10J-1 Force vs Time
Impact Force (kN)
Time (s)
×10^-3

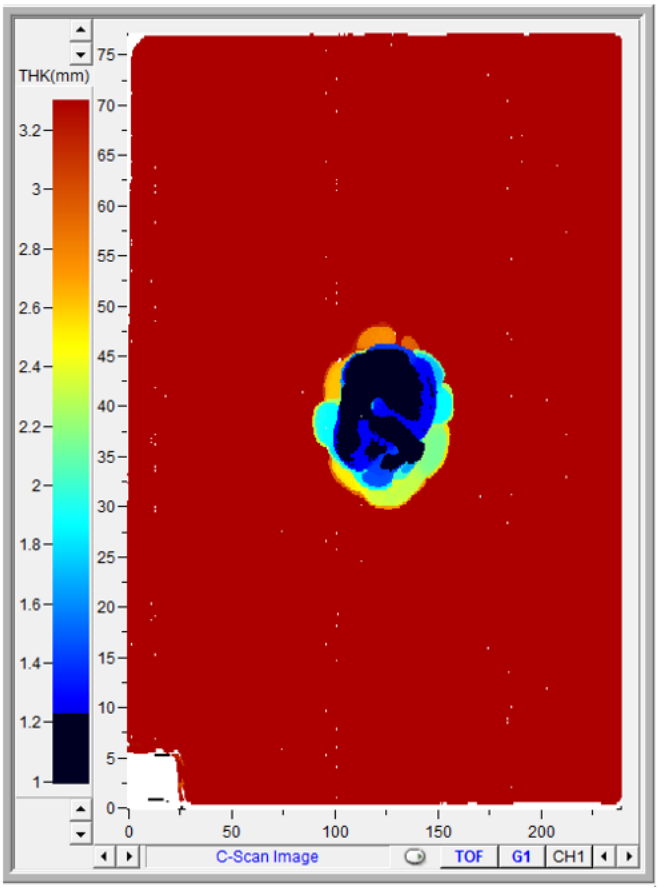
THK(mm)
C-Scan Image
TOF
G1
CH1

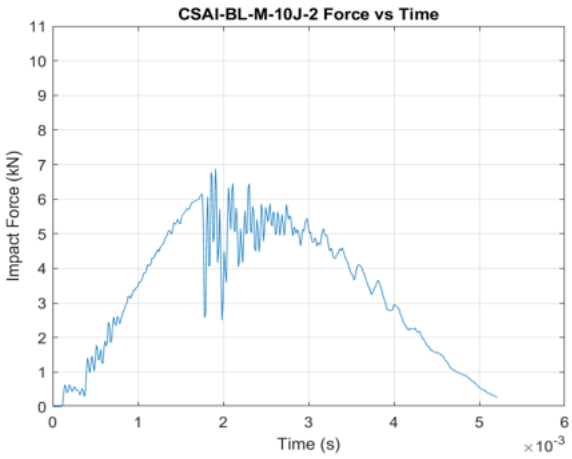
CSAI-BL-M-10J-2 Force vs Time
Impact Force (kN)
Time (s)
×10^-3

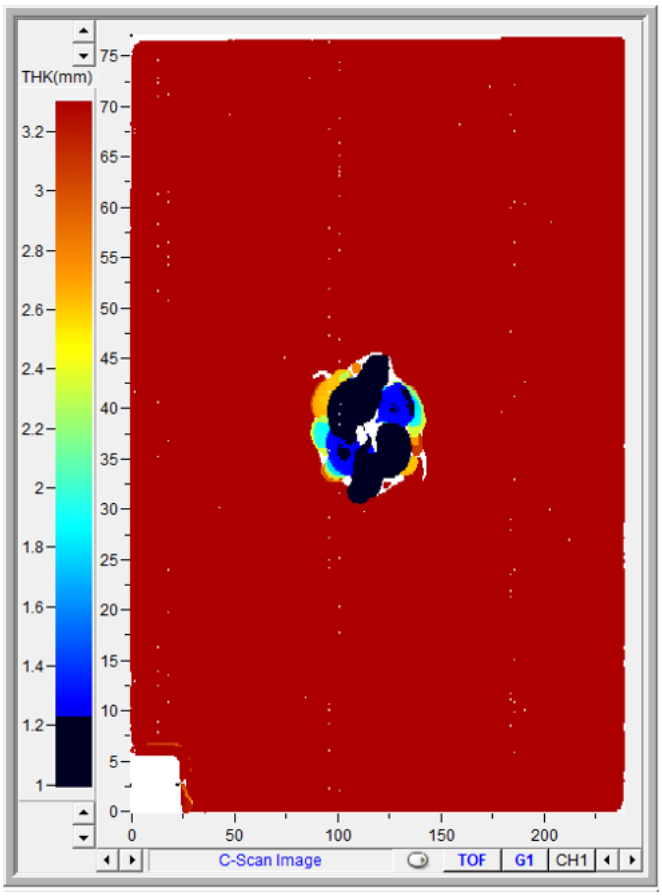
THK(mm)
C-Scan Image
TOF
G1
CH1

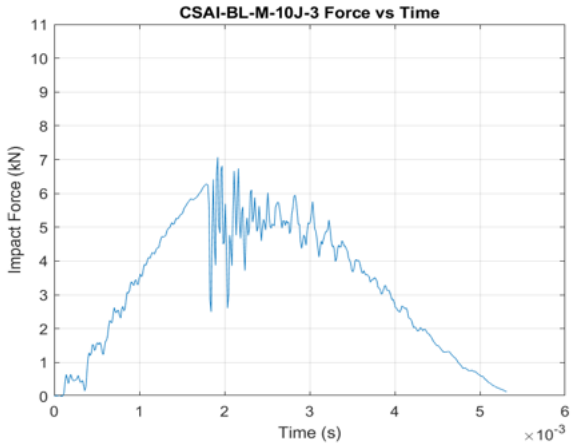
CSAI-BL-M-10J-3 Force vs Time
Impact Force (kN)
Time (s)
×10-3

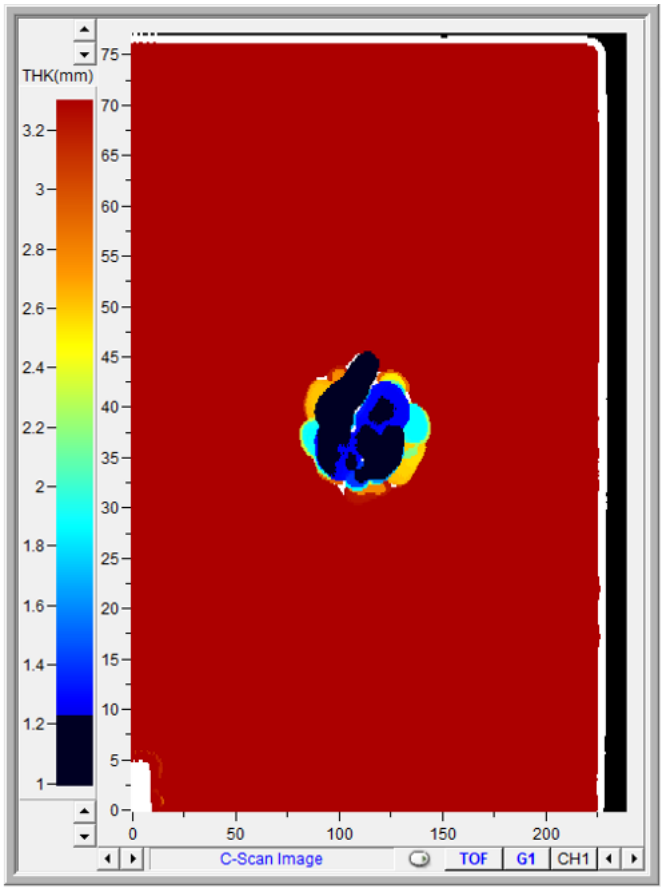
THK(mm)
C-Scan Image
TOF
G1
CH1

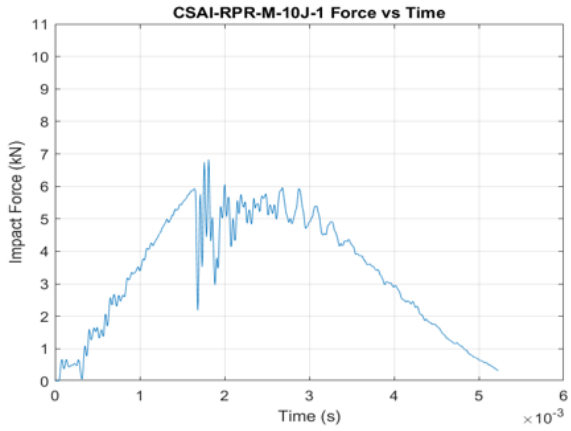
CSAI-RPR-M-10J-1 Force vs Time
Impact Force (kN)
Time (s)
×10^-3

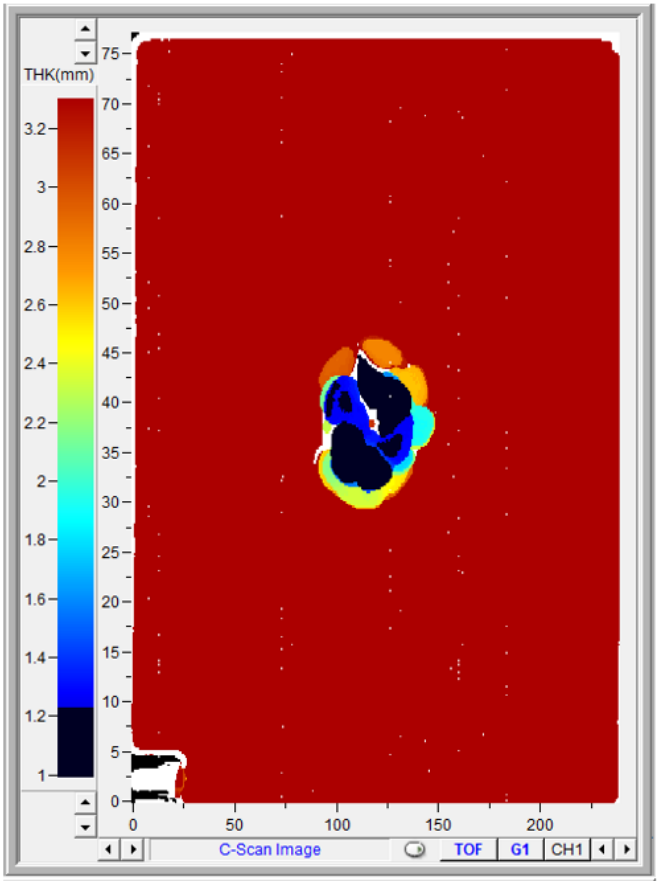
THK(mm)
C-Scan Image
TOF
G1
CH1

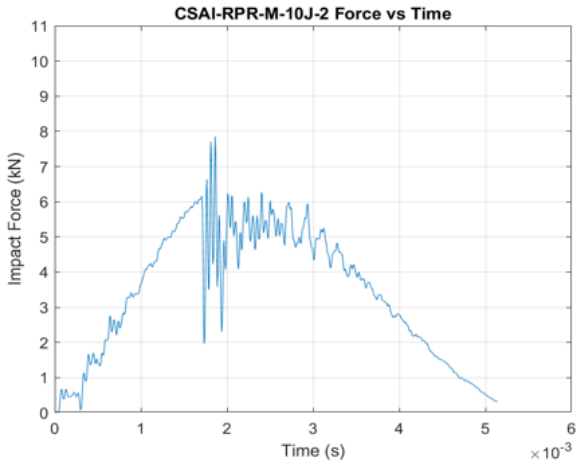
CSAI-RPR-M-10J-2 Force vs Time
Impact Force (kN)
Time (s)
×10-3

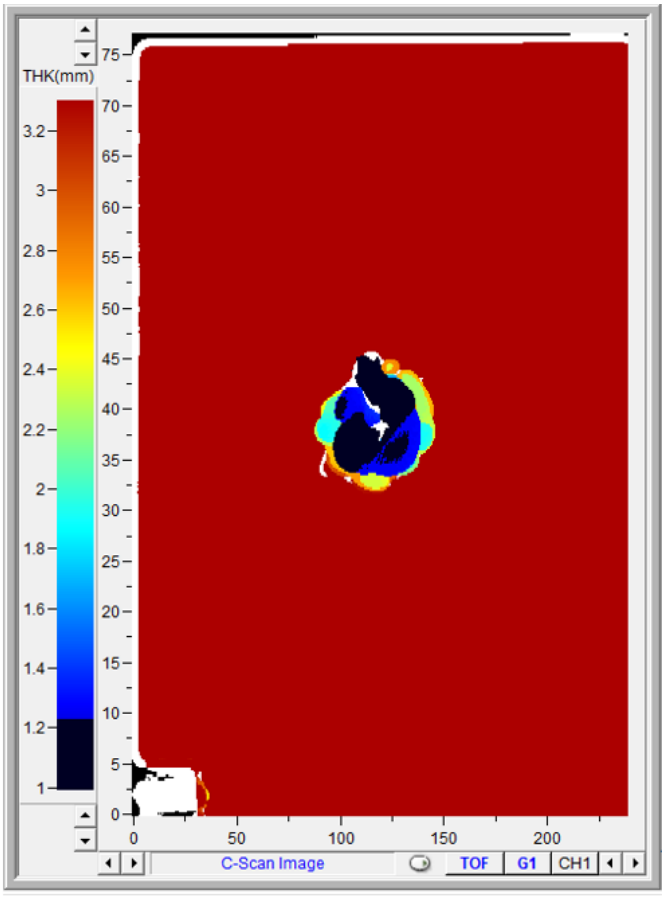
THK(mm)
C-Scan Image
TOF
G1
CH1

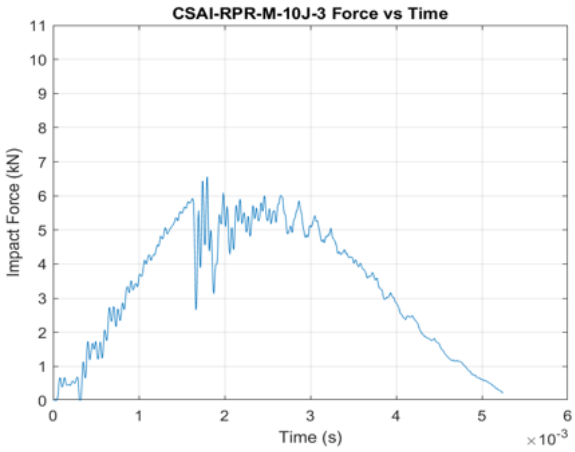
CSAI-RPR-M-10J-3 Force vs Time
Impact Force (kN)
Time (s)
×10-3

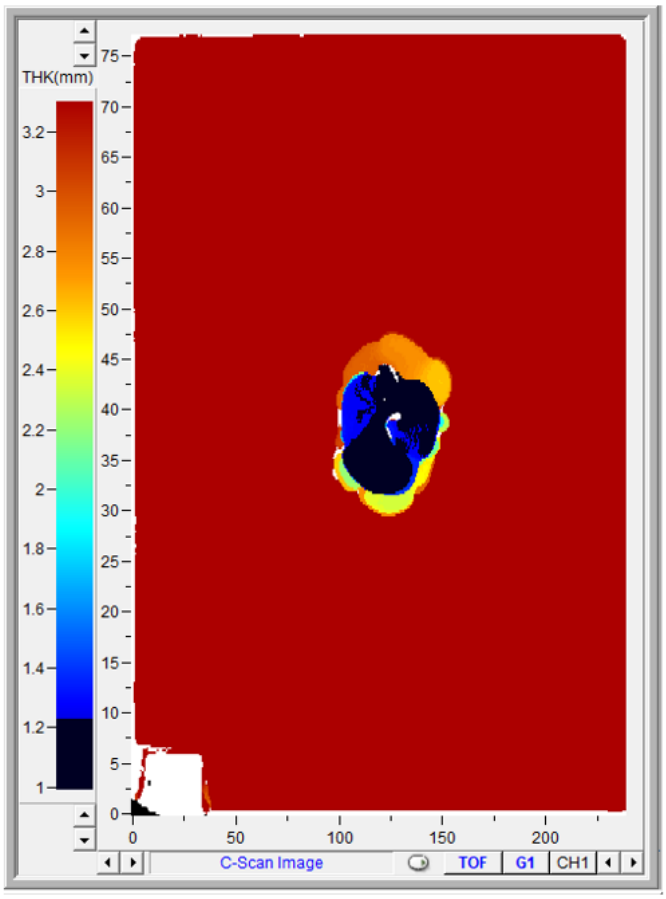
THK(mm)
C-Scan Image
TOF
G1
CH1

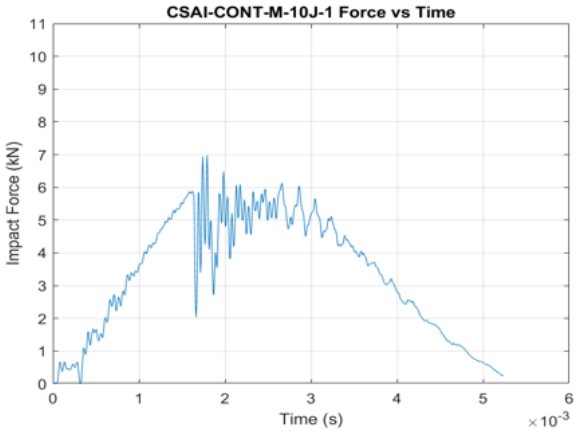
CSAI-CONT-M-10J-1 Force vs Time
Impact Force (kN)
Time (s)
×10^-3

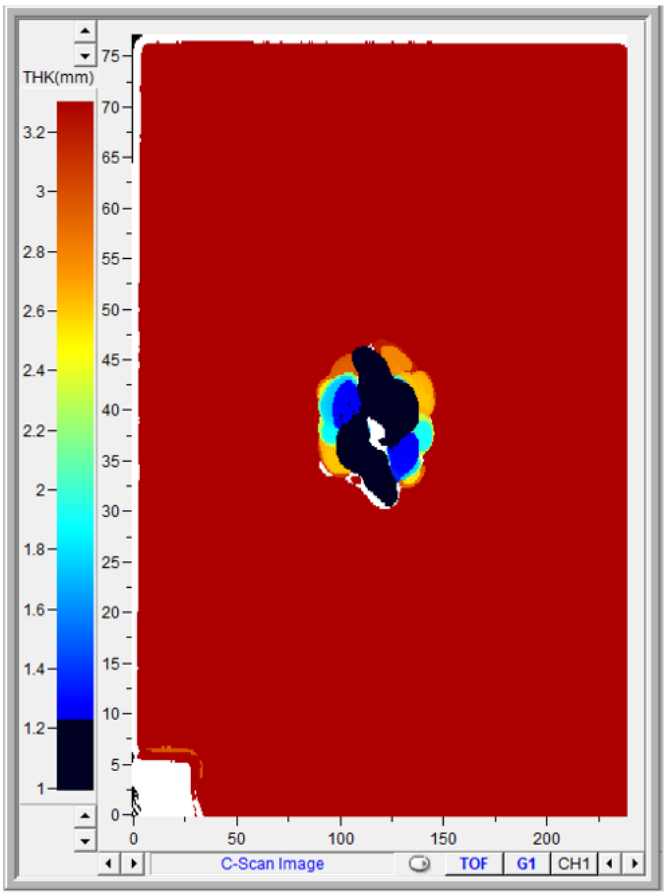
THK(mm)
C-Scan Image
TOF
G1
CH1

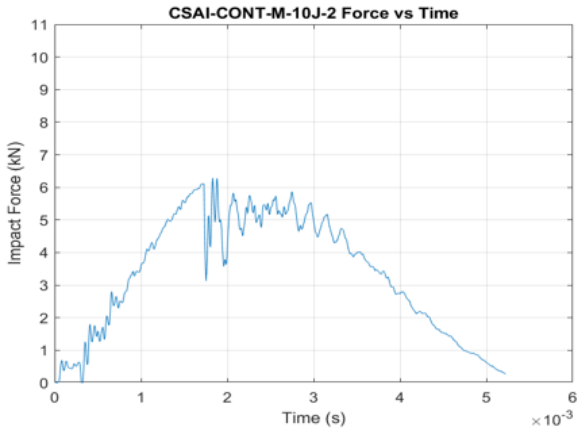
CSAI-CONT-M-10J-2 Force vs Time
Impact Force (kN)
Time (s)
×10^-3

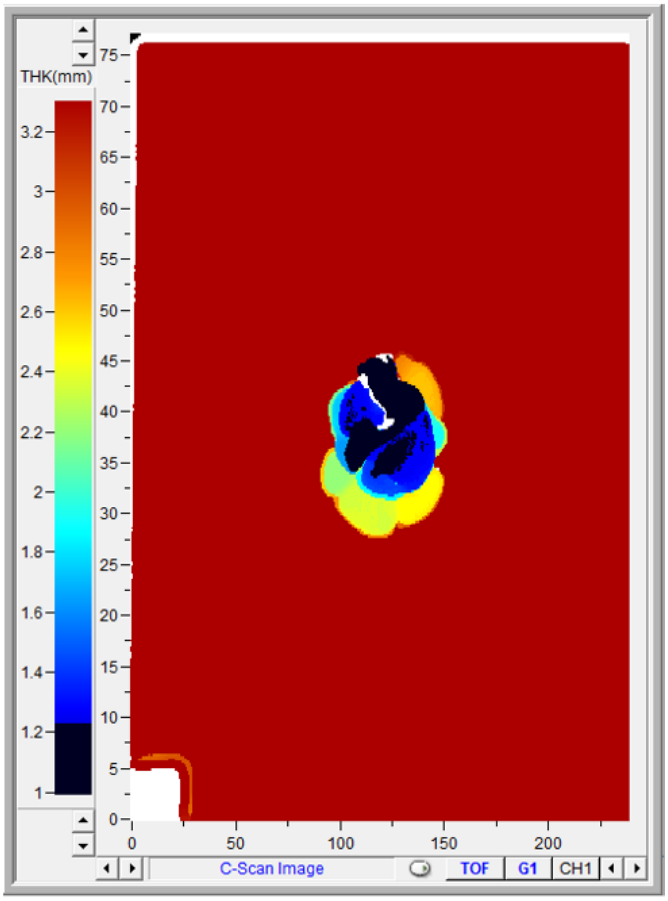
THK(mm)
C-Scan Image
TOF
G1
CH1

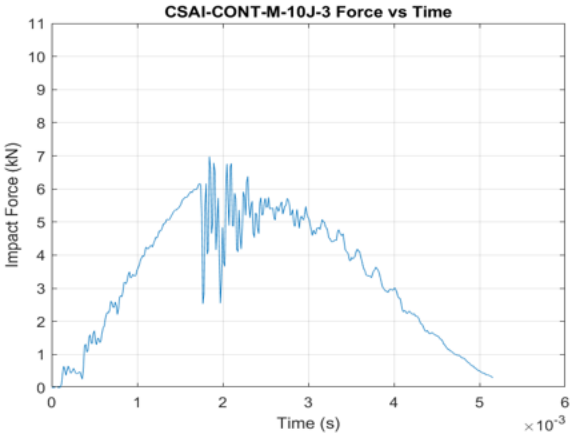
CSAI-CONT-M-10J-3 Force vs Time
Impact Force (kN)
Time (s)
×10-3

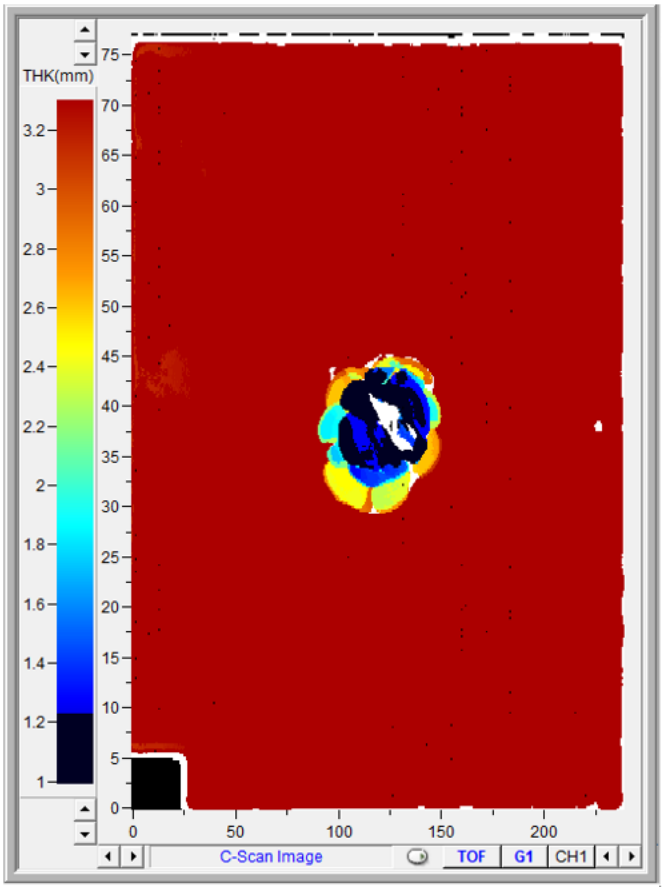
THK(mm)
C-Scan Image
TOF
G1
CH1

Panel S 10 J

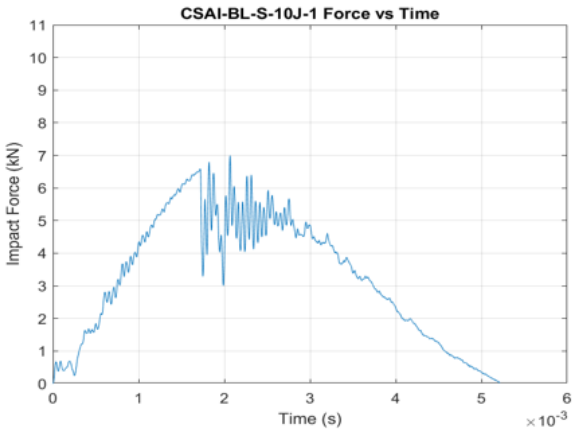
CSAI-BL-S-10J-1 Force vs Time
Impact Force (kN)
Time (s)
×10^-3

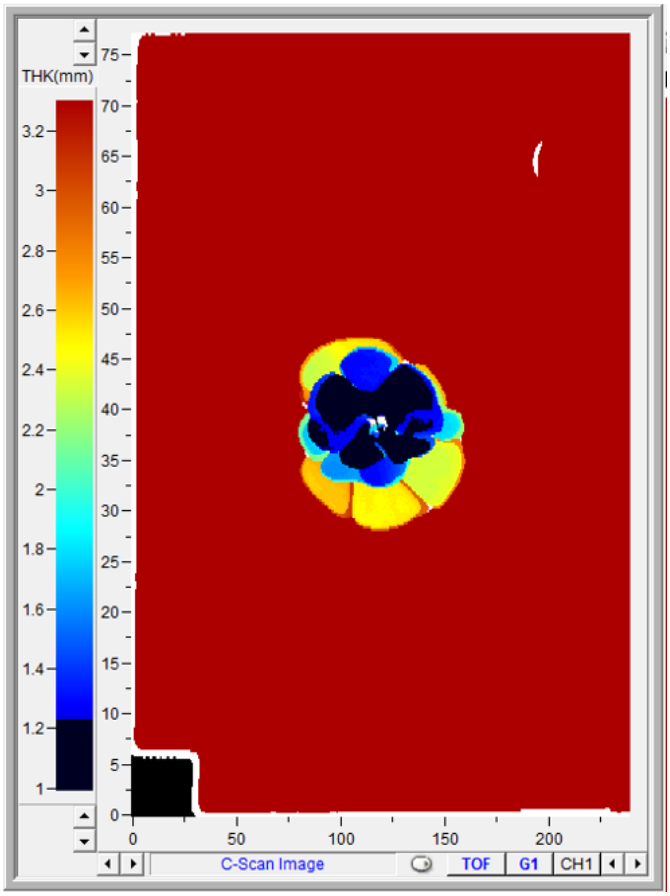
THK(mm)
C-Scan Image
TOF
G1
CH1

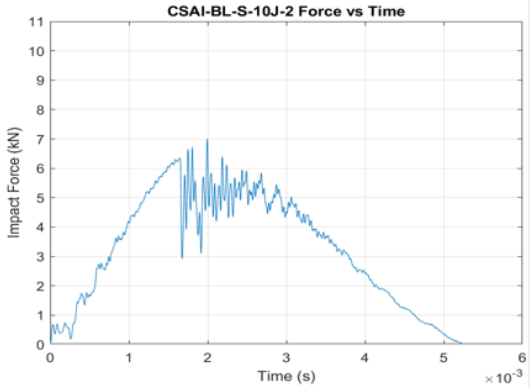

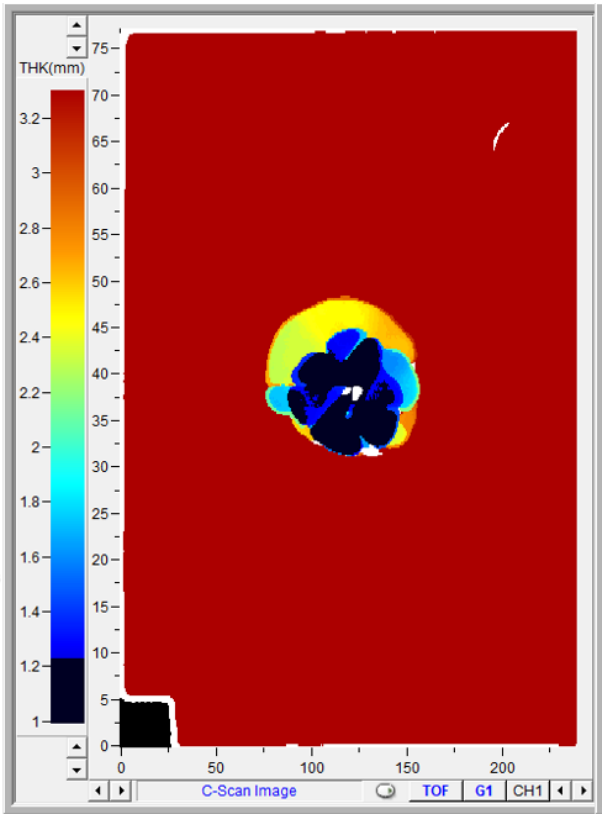

Frontside

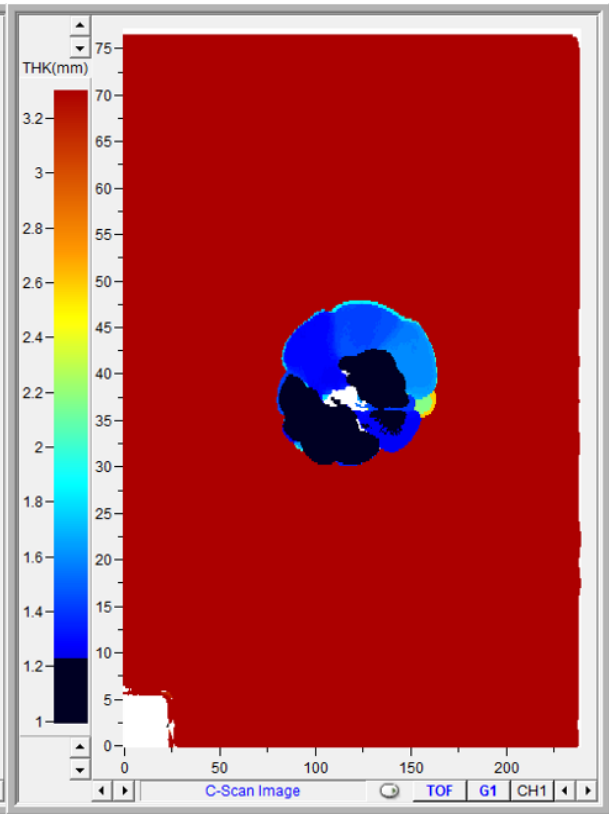

Backside

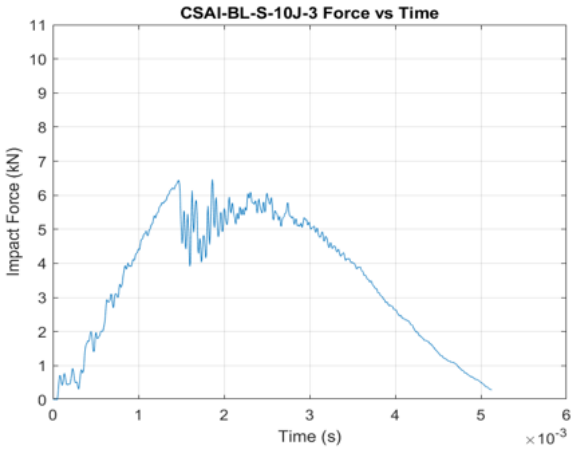
CSAI-BL-S-10J-3 Force vs Time
Impact Force (kN)
Time (s)
×10^-3

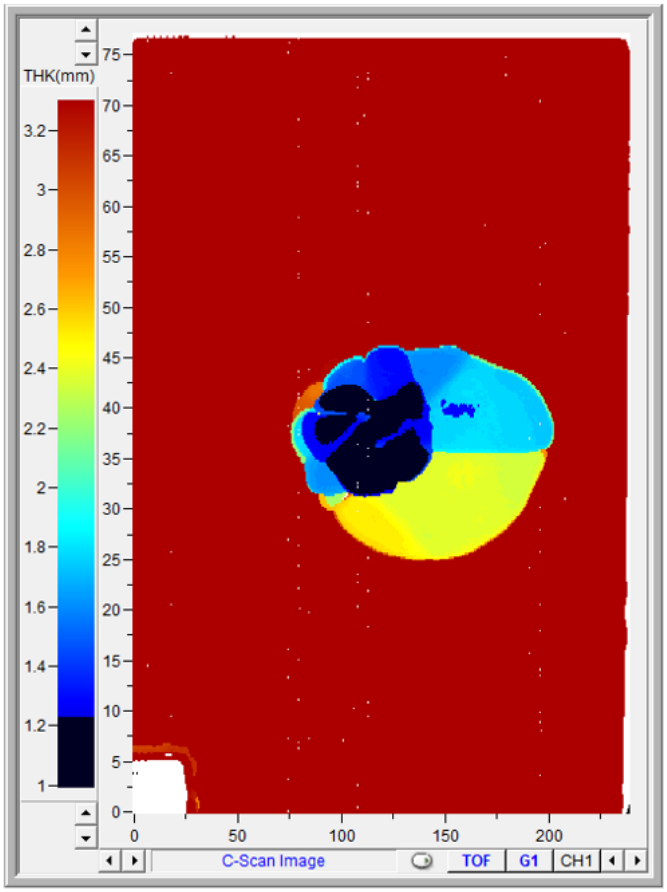
THK(mm)
C-Scan Image
TOF
G1
CH1

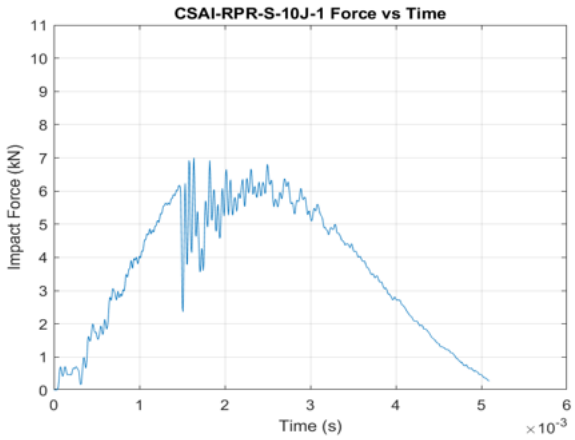
CSAI-RPR-S-10J-1 Force vs Time
Impact Force (kN)
Time (s)
×10^-3

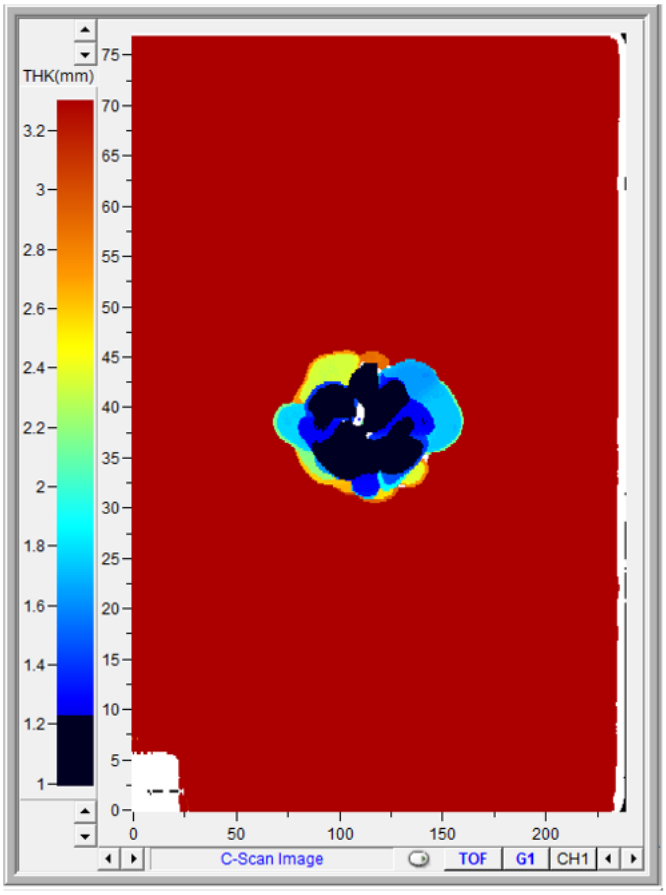
THK(mm)
C-Scan Image
TOF
G1
CH1

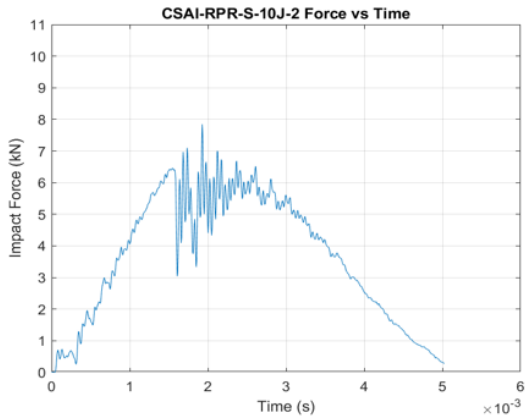

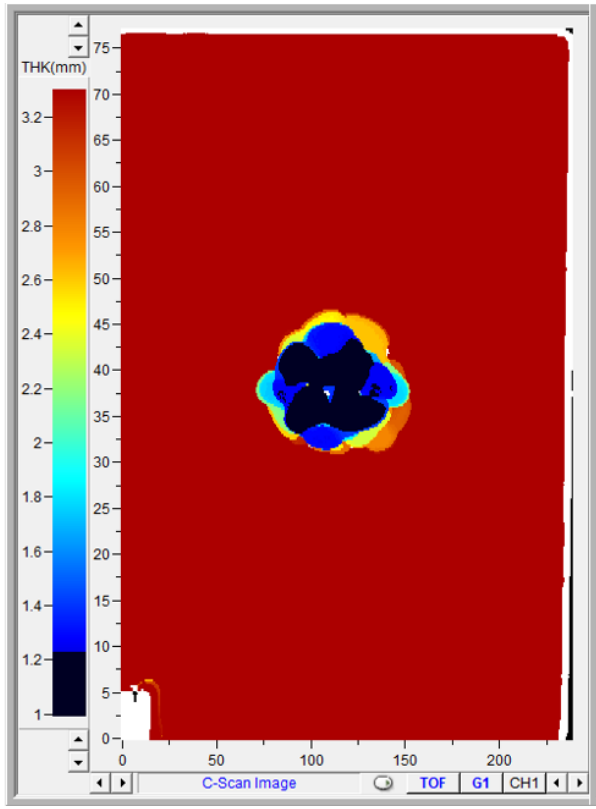

Frontside

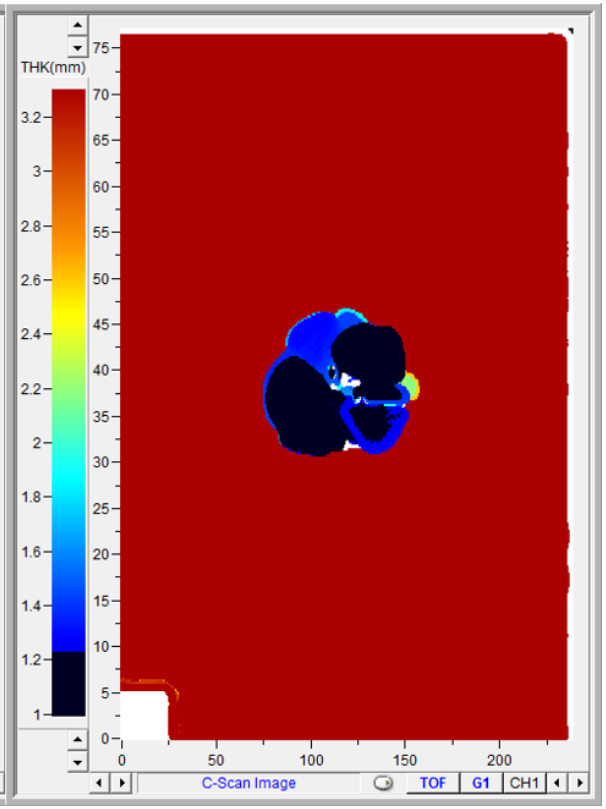

Backside

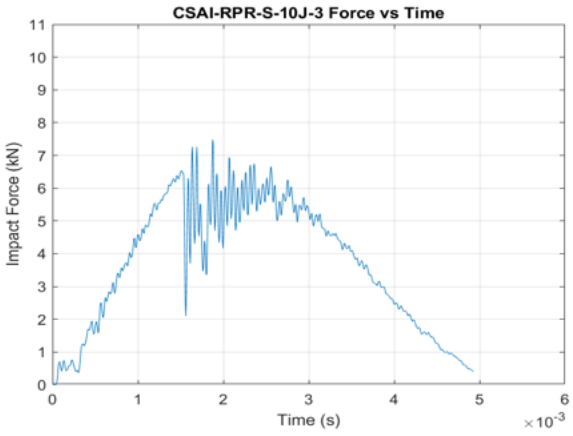
CSAI-RPR-S-10J-3 Force vs Time
Impact Force (kN)
Time (s)
×10^-3

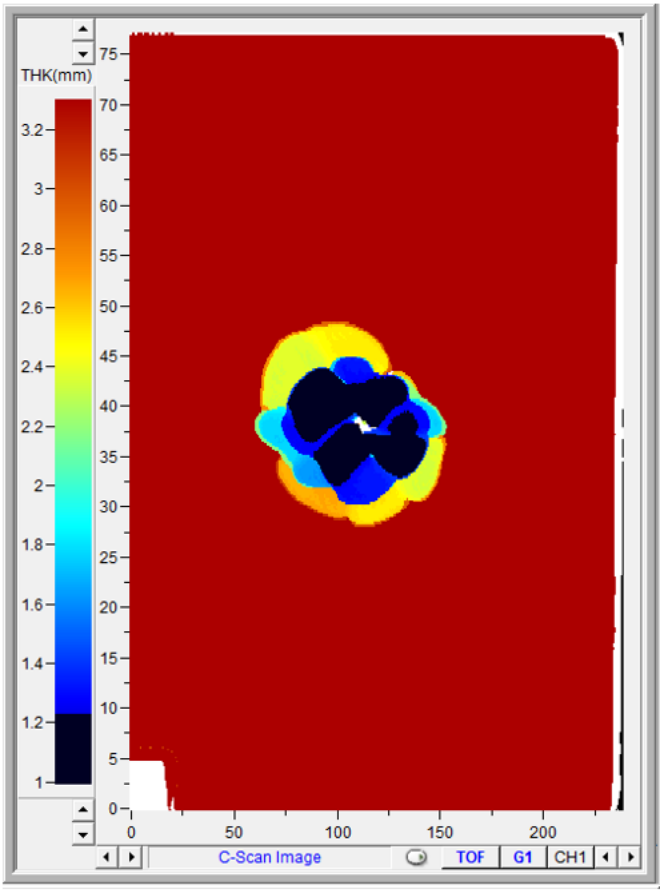
THK(mm)
C-Scan Image
TOF
G1
CH1

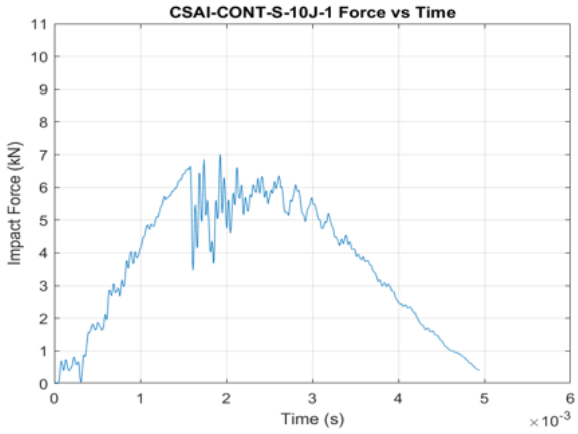
CSAI-CONT-S-10J-1 Force vs Time
Impact Force (kN)
Time (s)
×10^-3

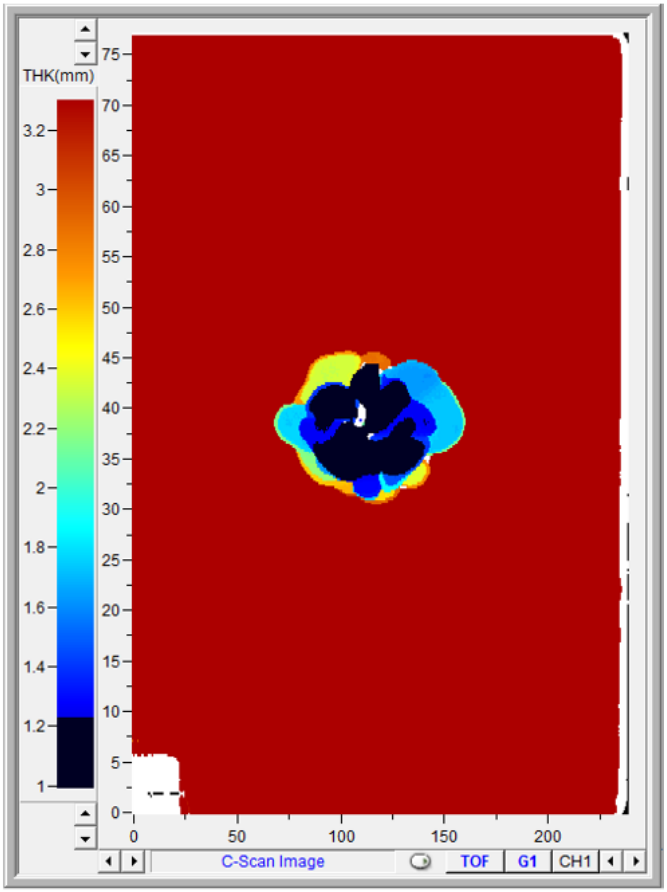
THK(mm)
C-Scan Image
TOF
G1
CH1

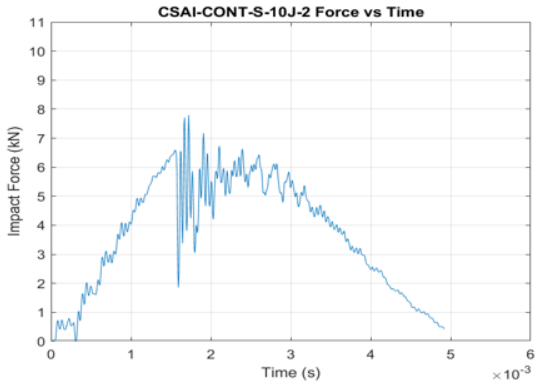

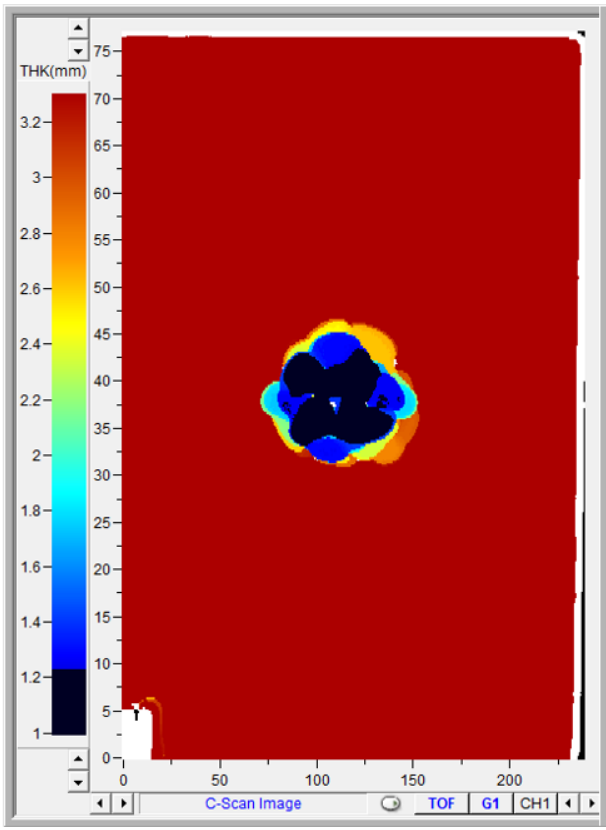

Frontside

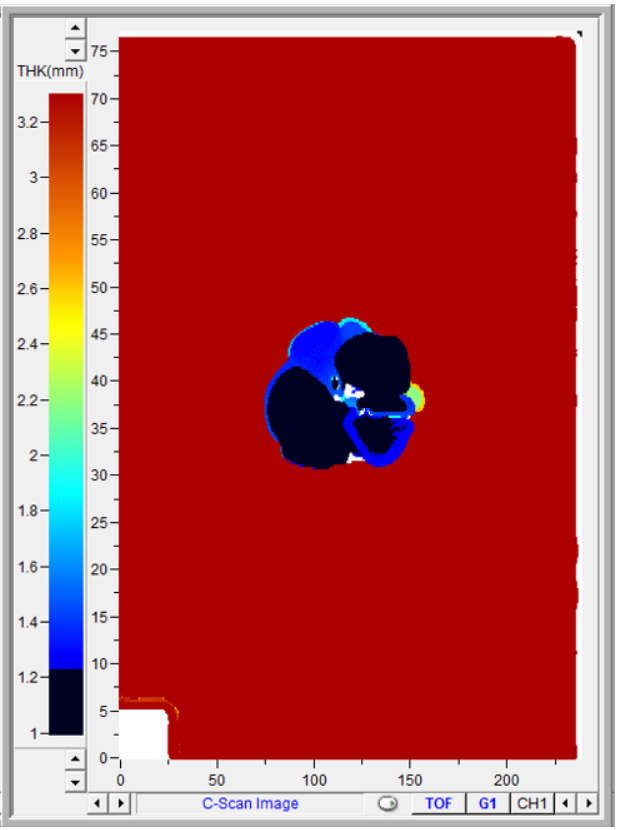

Backside

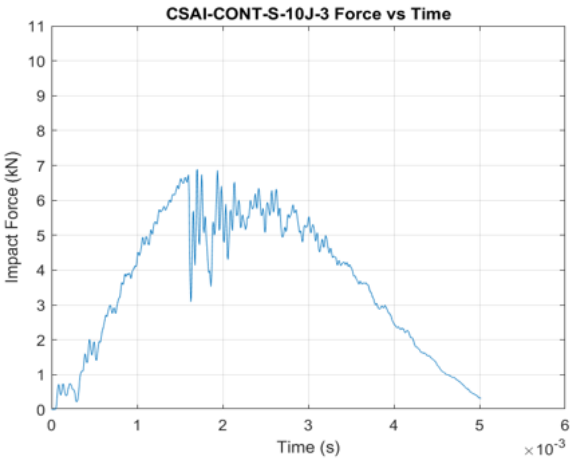
CSAI-CONT-S-10J-3 Force vs Time
Impact Force (kN)
Time (s)
×10-3

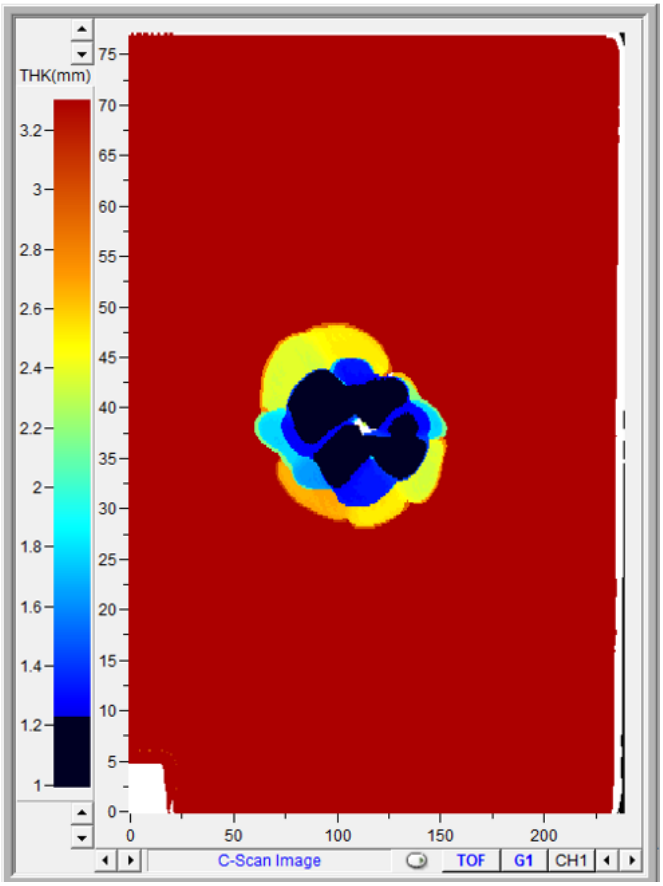
THK(mm)
C-Scan Image
TOF
G1
CH1

Panel H 15 J

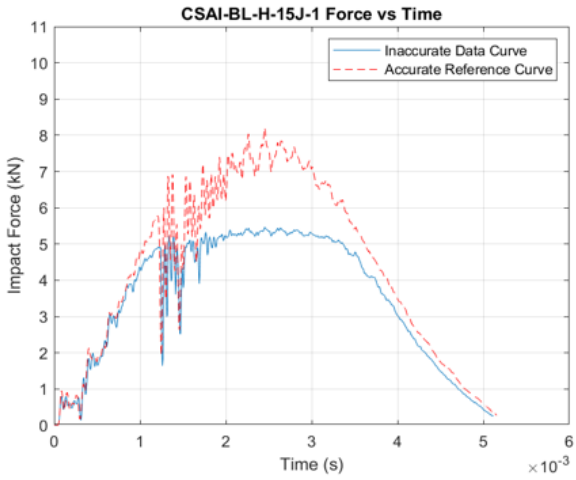
CSAI-BL-H-15J-1 Force vs Time
Inaccurate Data Curve
Accurate Reference Curve
Impact Force (kN)
Time (s)
×10^-3

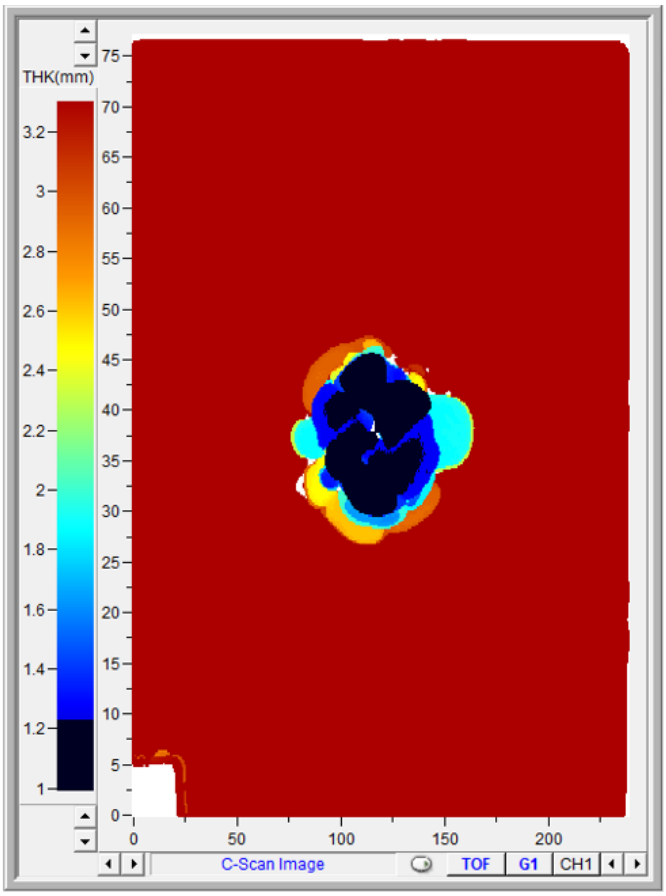
THK(mm)
C-Scan Image
TOF
G1
CH1

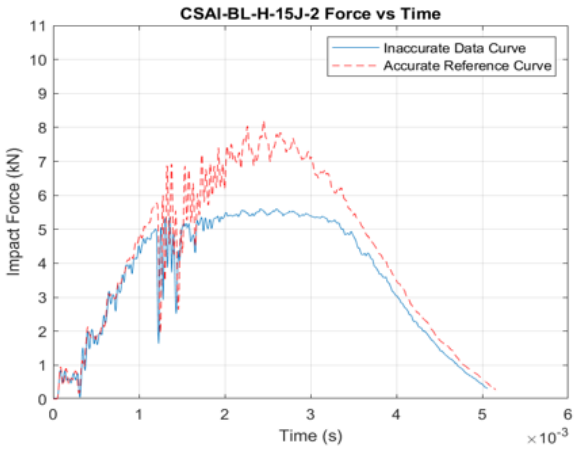
CSAI-BL-H-15J-2 Force vs Time
Inaccurate Data Curve
Accurate Reference Curve
Impact Force (kN)
Time (s)
×10^-3

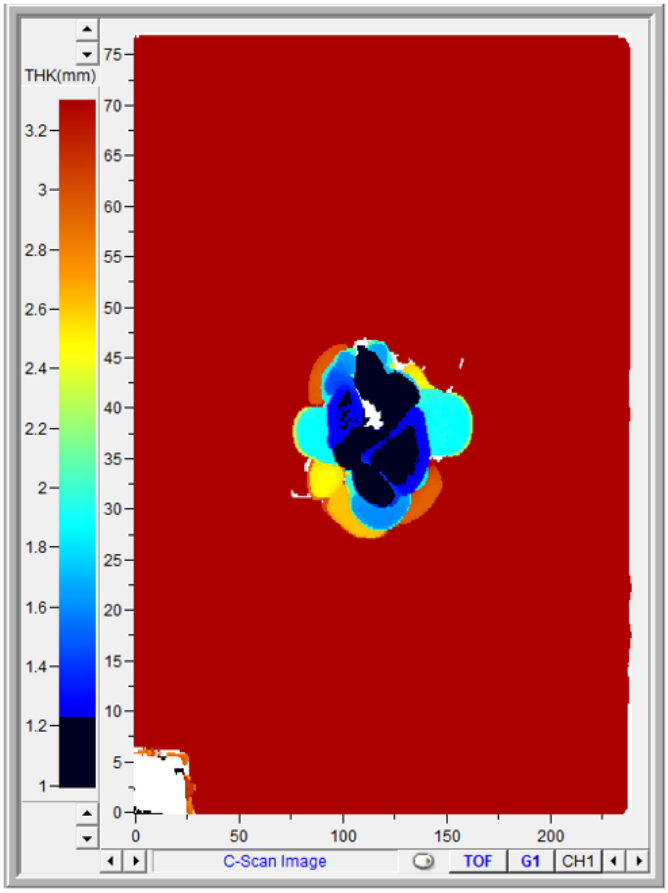
THK(mm)
C-Scan Image
TOF
G1
CH1

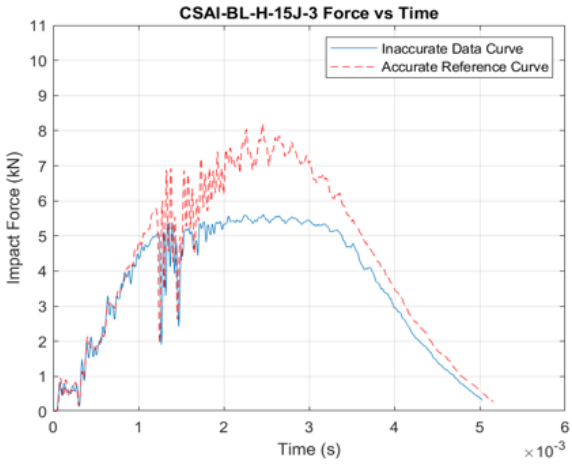
CSAI-BL-H-15J-3 Force vs Time
Inaccurate Data Curve
Accurate Reference Curve
Impact Force (kN)
Time (s)
×10^-3

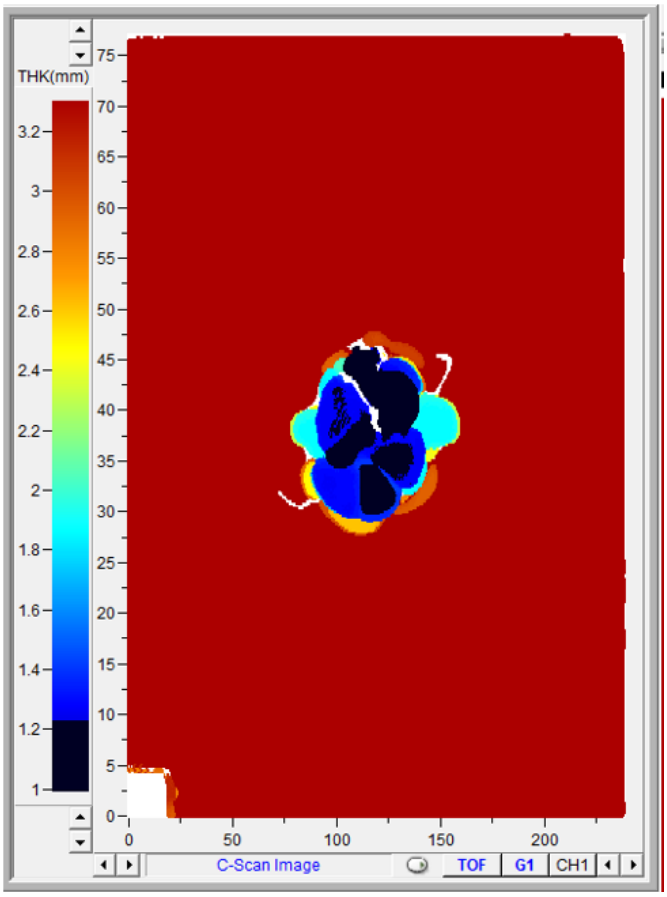
THK(mm)
C-Scan Image
TOF
G1
CH1

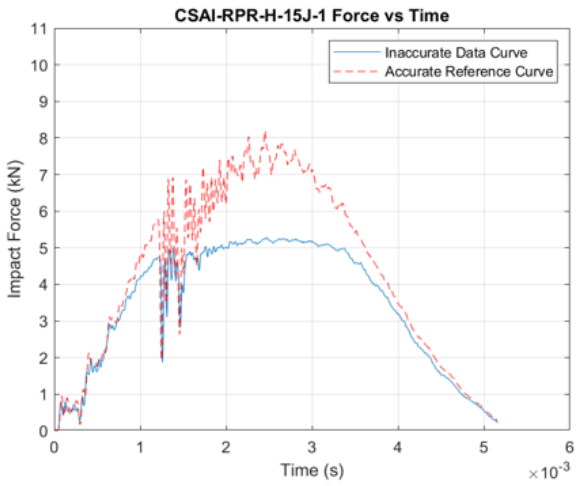
CSAI-RPR-H-15J-1 Force vs Time
Inaccurate Data Curve
Accurate Reference Curve
Impact Force (kN)
Time (s)
×10^-3

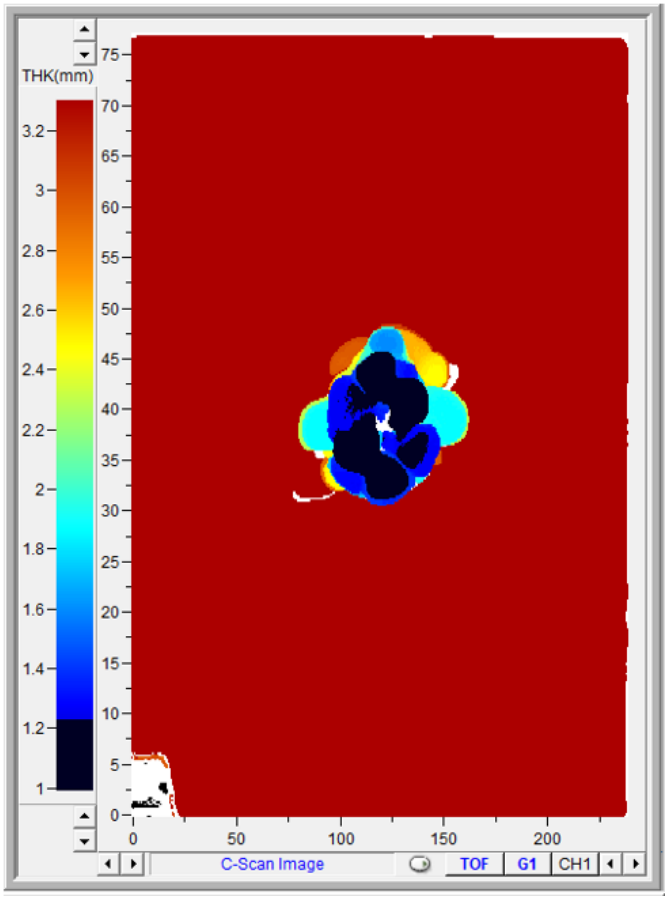
THK(mm)
C-Scan Image
TOF
G1
CH1

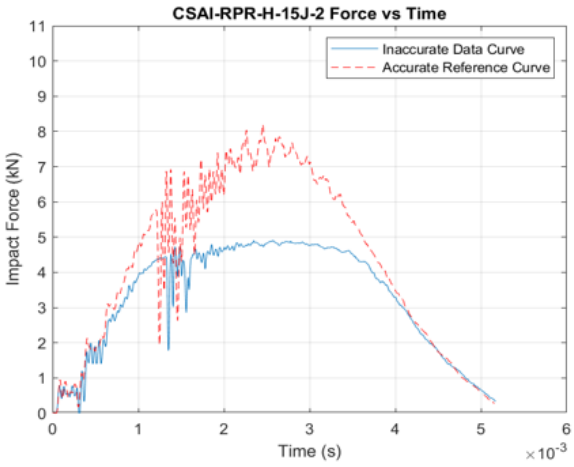
CSAI-RPR-H-15J-2 Force vs Time
Inaccurate Data Curve
Accurate Reference Curve
Impact Force (kN)
Time (s)
×10-3

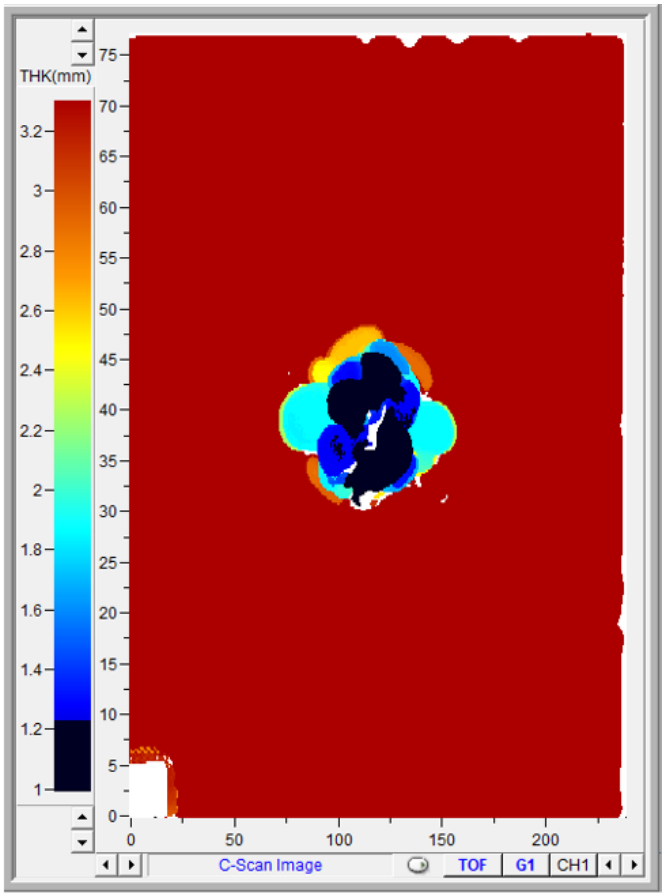
THK(mm)
C-Scan Image
TOF
G1
CH1

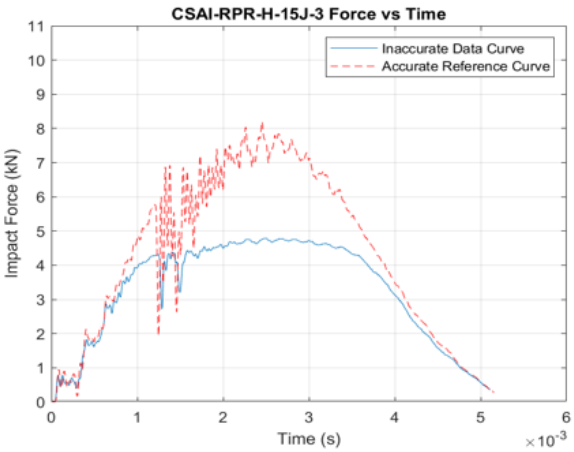
CSAI-RPR-H-15J-3 Force vs Time
Inaccurate Data Curve
Accurate Reference Curve
Impact Force (kN)
Time (s)
×10-3

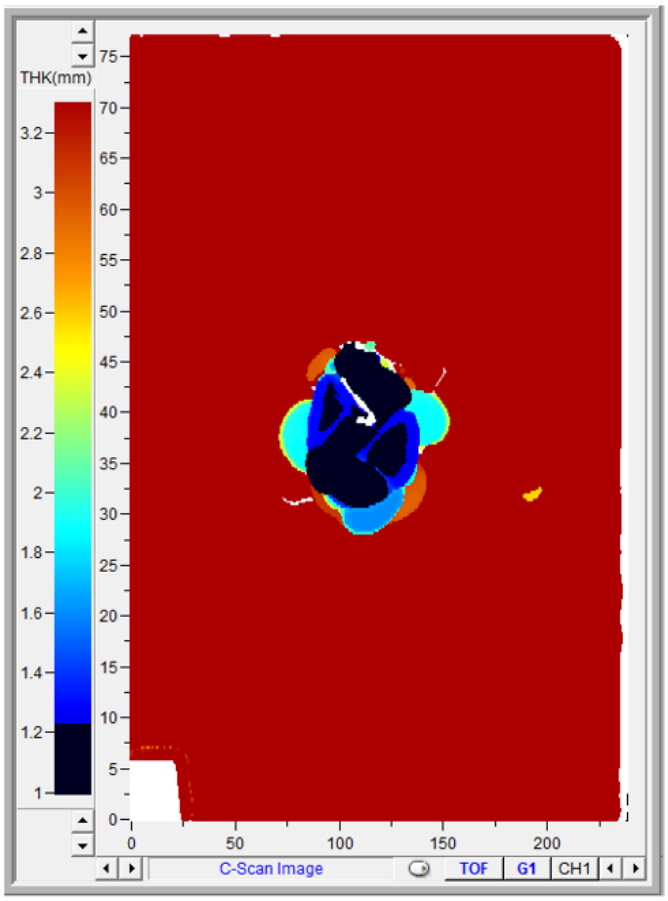
THK(mm)
C-Scan Image
TOF
G1
CH1

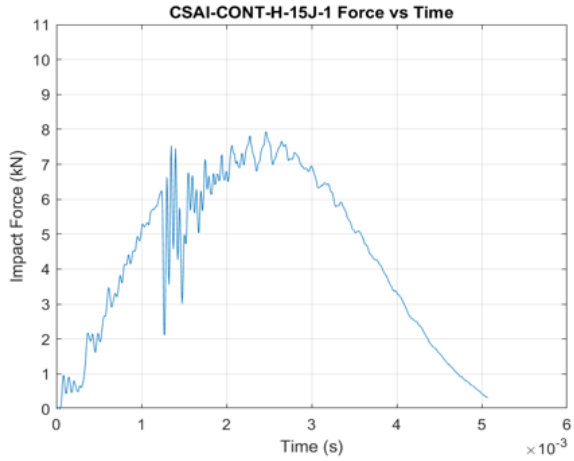
CSAI-CONT-H-15J-1 Force vs Time
Impact Force (kN)
Time (s)
×10-3

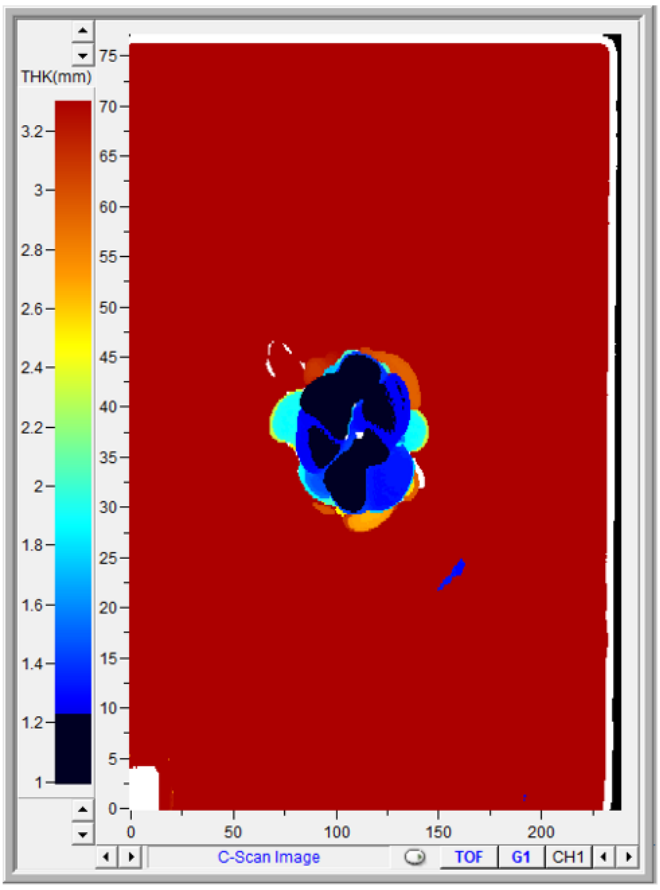
THK(mm)
C-Scan Image
TOF
G1
CH1

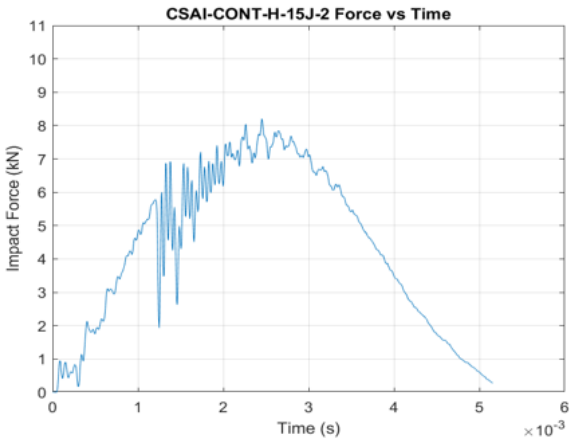
CSAI-CONT-H-15J-2 Force vs Time
Impact Force (kN)
Time (s)
×10^-3

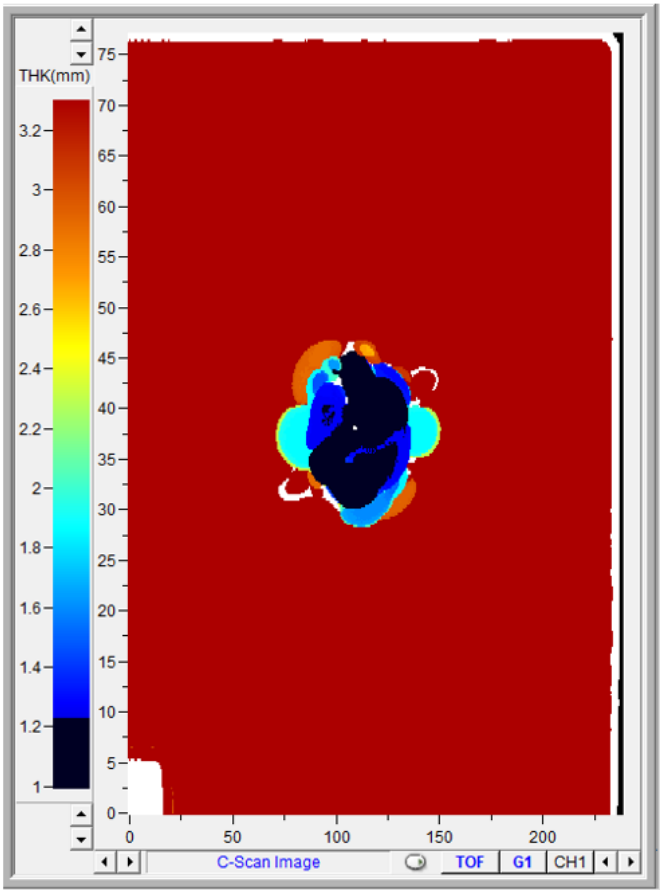
THK(mm)
C-Scan Image
TOF
G1
CH1

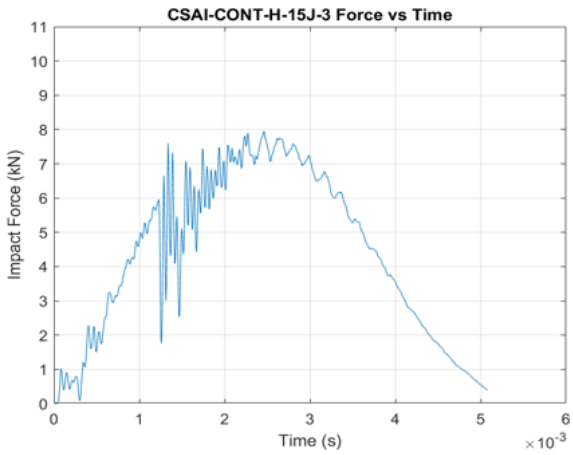
CSAI-CONT-H-15J-3 Force vs Time
Impact Force (kN)
Time (s)
×10^-3

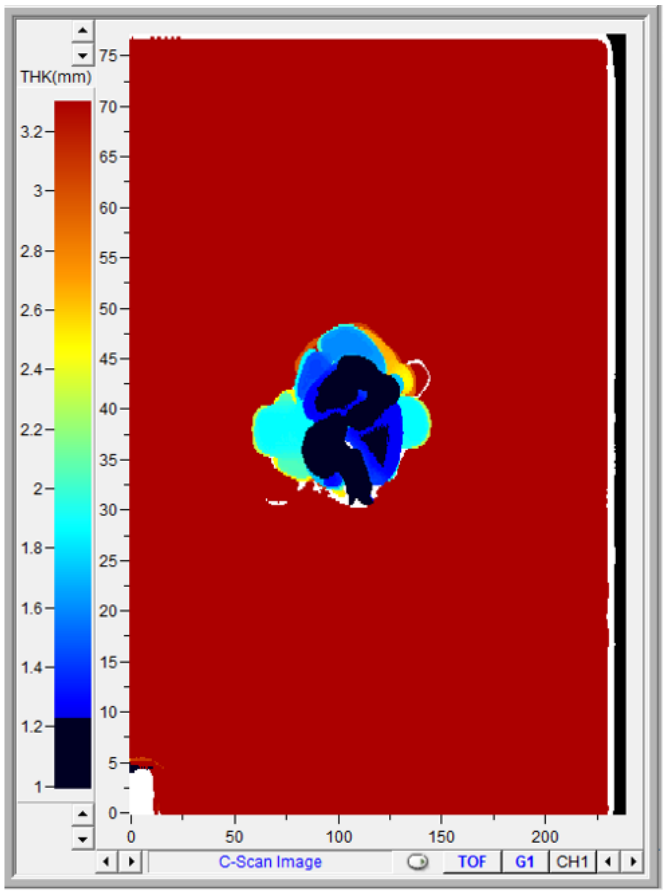
THK(mm)
C-Scan Image
TOF
G1
CH1

Panel M 15 J

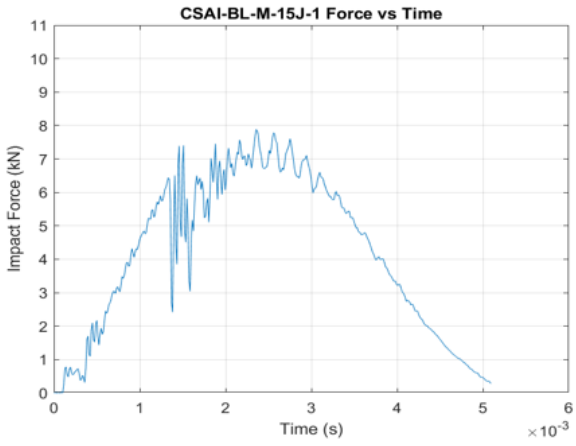
CSAI-BL-M-15J-1 Force vs Time
Impact Force (kN)
Time (s)
×10^-3

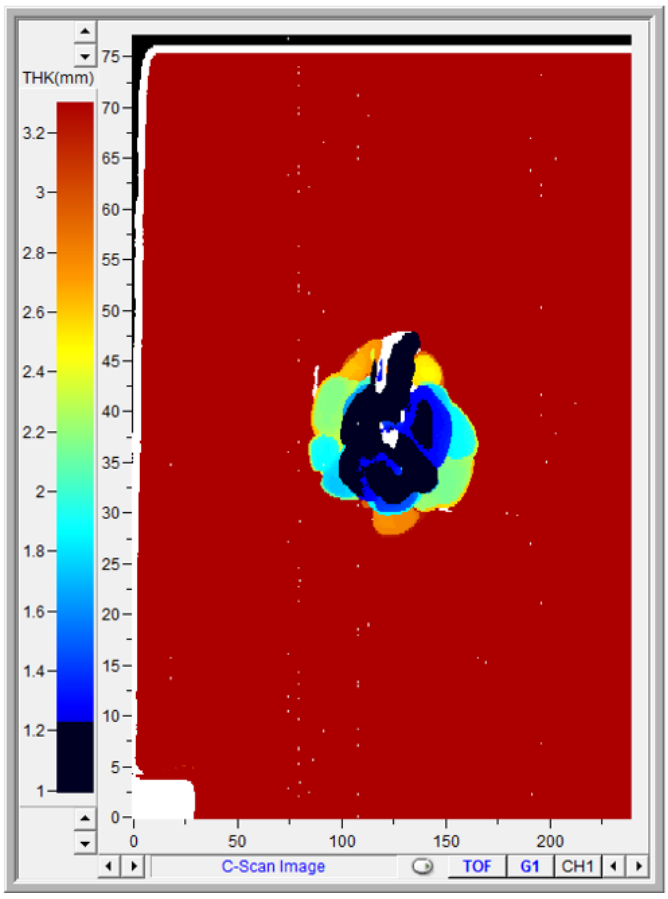
THK(mm)
C-Scan Image
TOF
G1
CH1

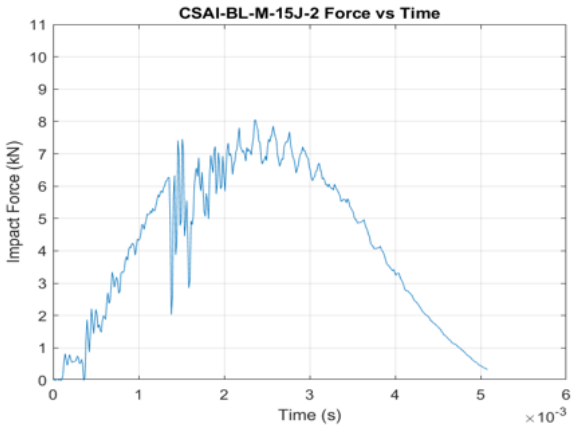
CSAI-BL-M-15J-2 Force vs Time
Impact Force (kN)
Time (s)
×10^-3

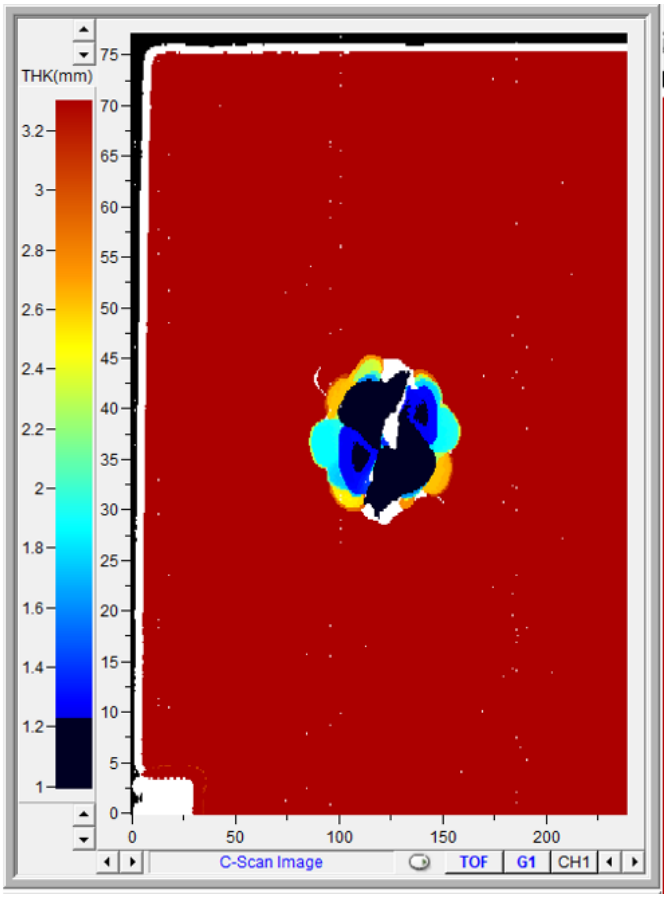
THK(mm)
C-Scan Image
TOF
G1
CH1

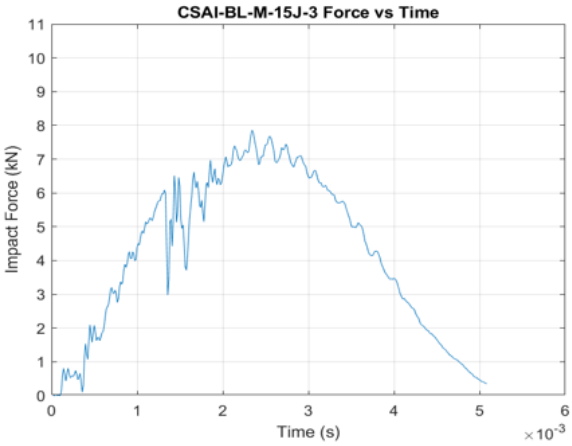
CSAI-BL-M-15J-3 Force vs Time
Impact Force (kN)
Time (s)
×10-3

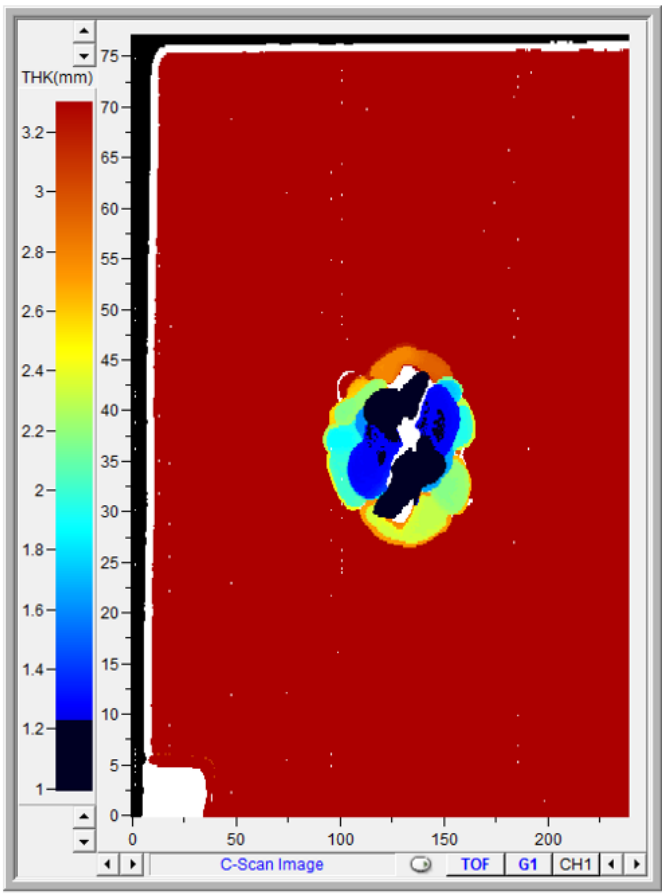
THK(mm)
C-Scan Image
TOF
G1
CH1

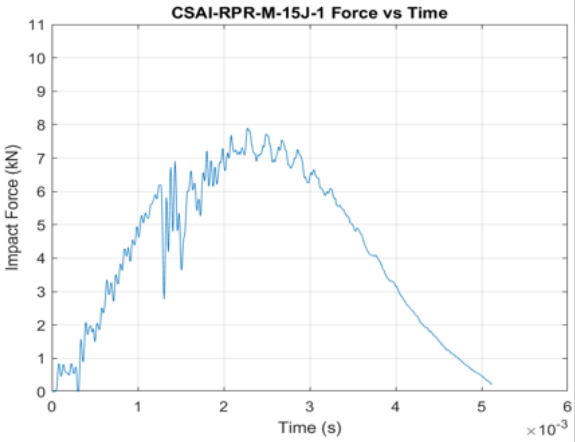
CSAI-RPR-M-15J-1 Force vs Time
Impact Force (kN)
Time (s)
×10-3

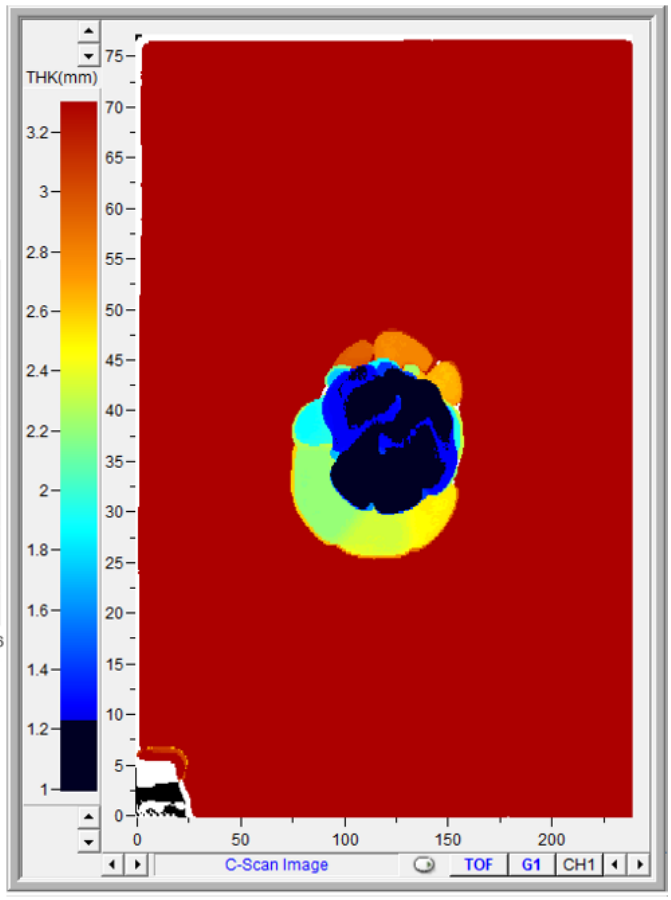
THK(mm)
C-Scan Image
TOF
G1
CH1

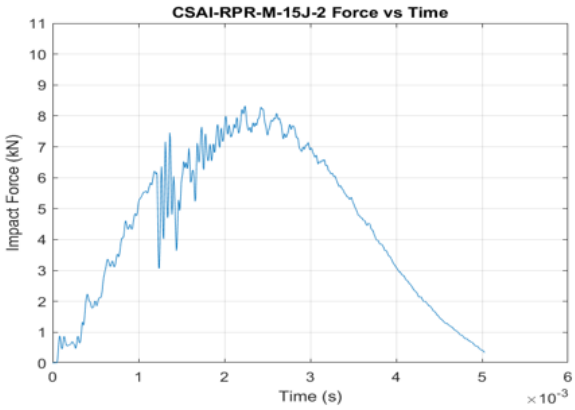
CSAI-RPR-M-15J-2 Force vs Time
Impact Force (kN)
Time (s)
×10^-3

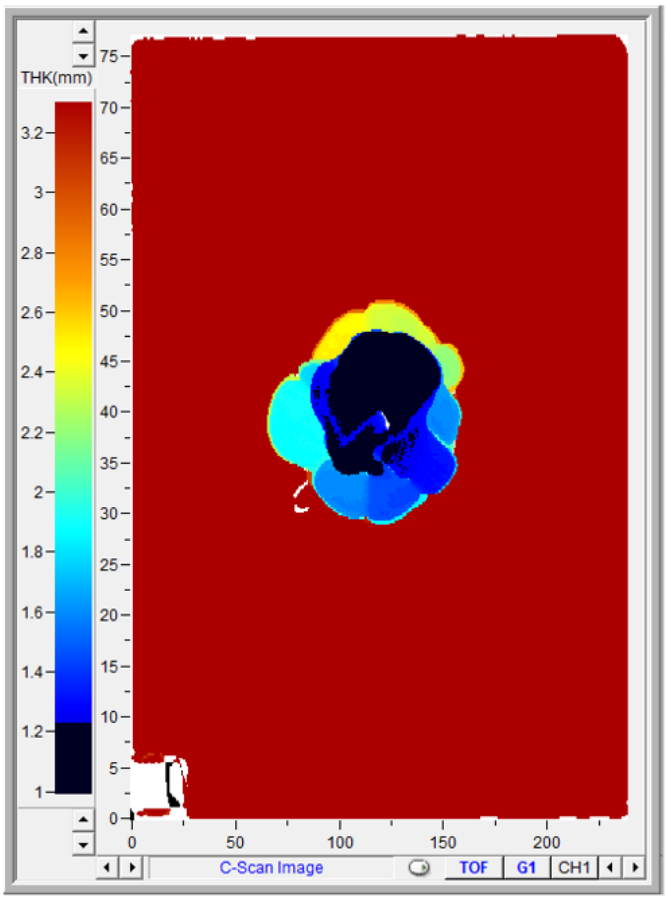
THK(mm)
C-Scan Image
TOF
G1
CH1

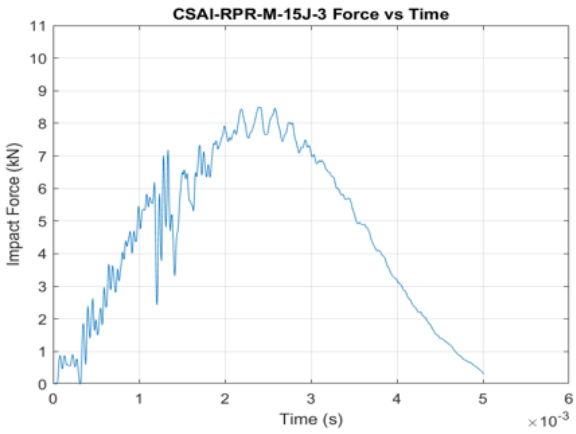
CSAI-RPR-M-15J-3 Force vs Time
Impact Force (kN)
Time (s)
×10^-3

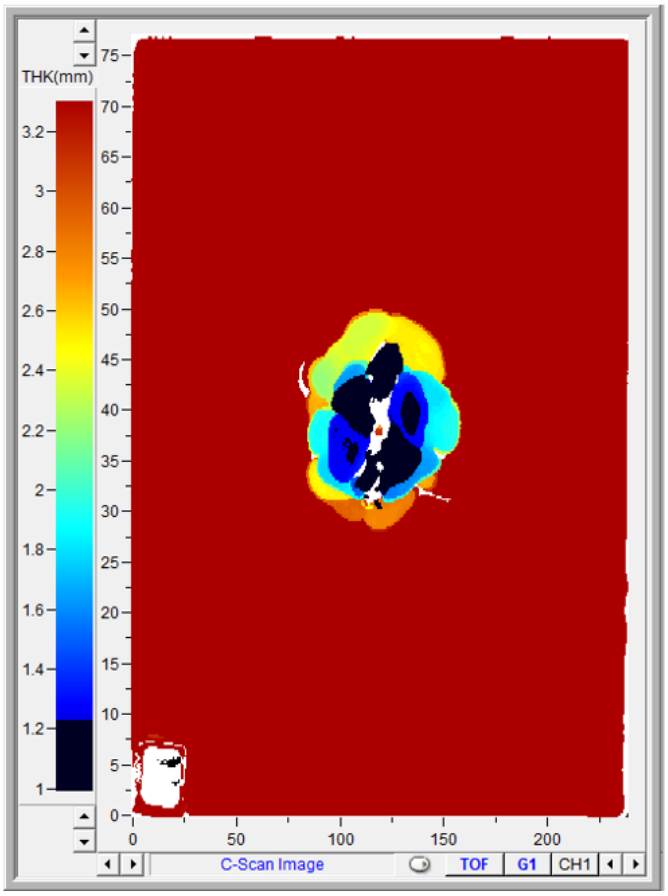
THK(mm)
C-Scan Image
TOF
G1
CH1

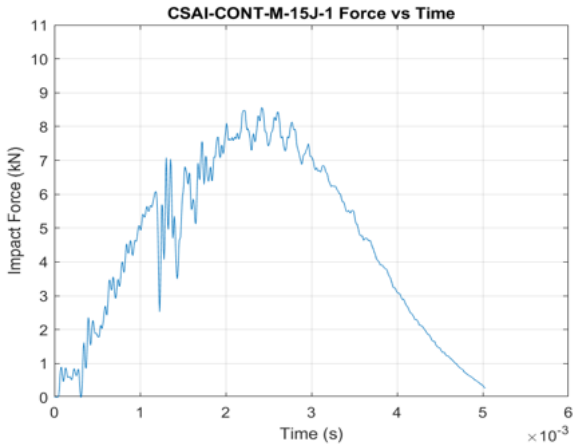
CSAI-CONT-M-15J-1 Force vs Time
Impact Force (kN)
Time (s)
×10^-3

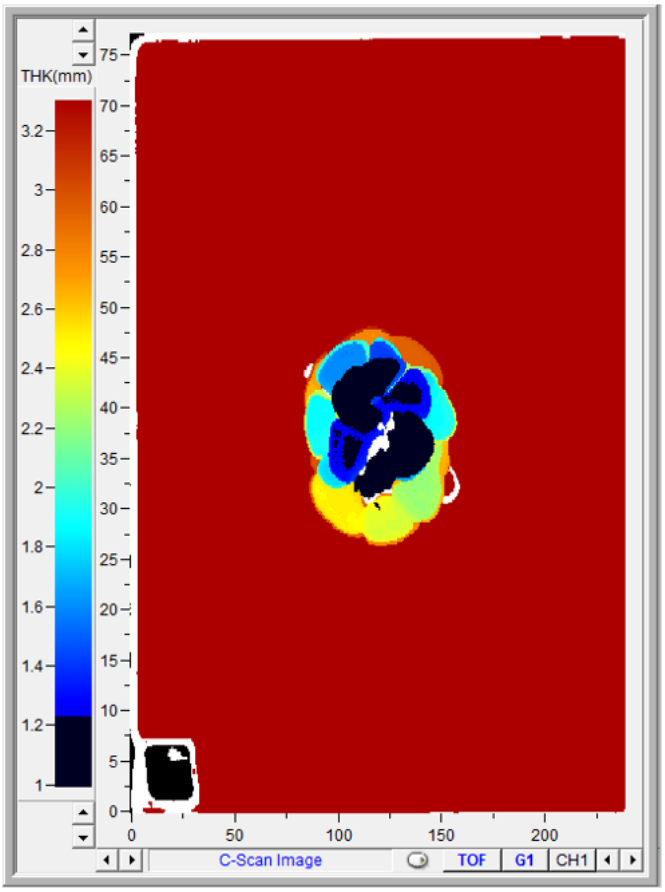
THK(mm)
C-Scan Image
TOF
G1
CH1

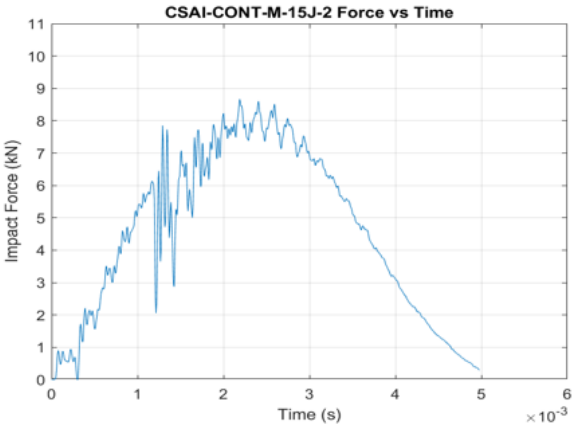
CSAI-CONT-M-15J-2 Force vs Time
Impact Force (kN)
Time (s)
×10-3

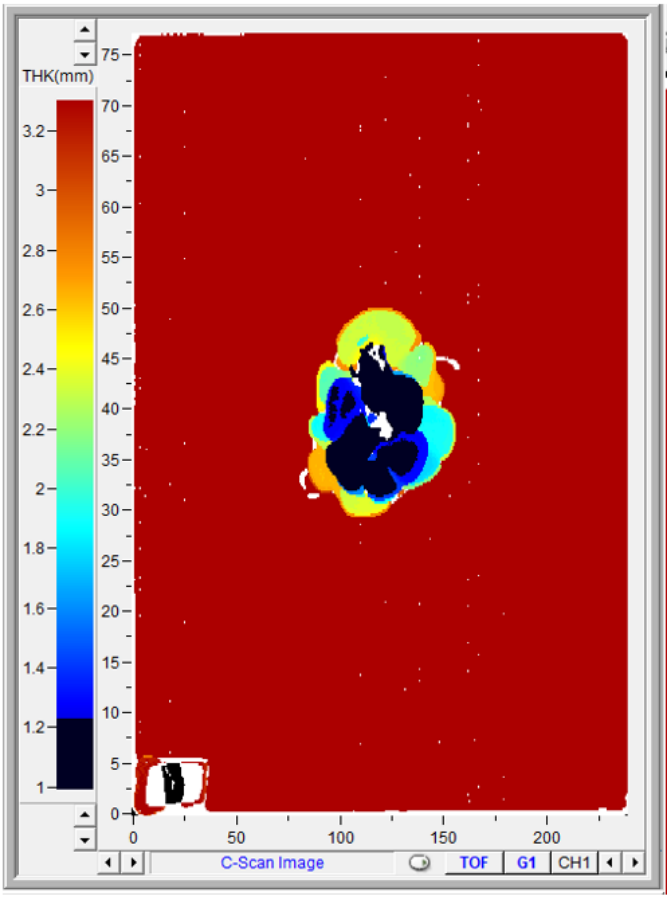
THK(mm)
C-Scan Image
TOF
G1
CH1

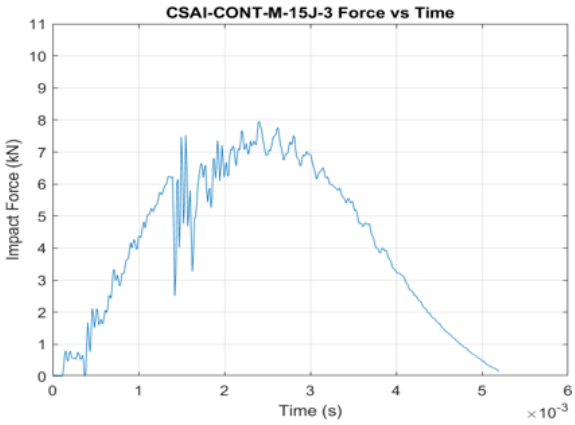
CSAI-CONT-M-15J-3 Force vs Time
Impact Force (kN)
Time (s)
×10^-3

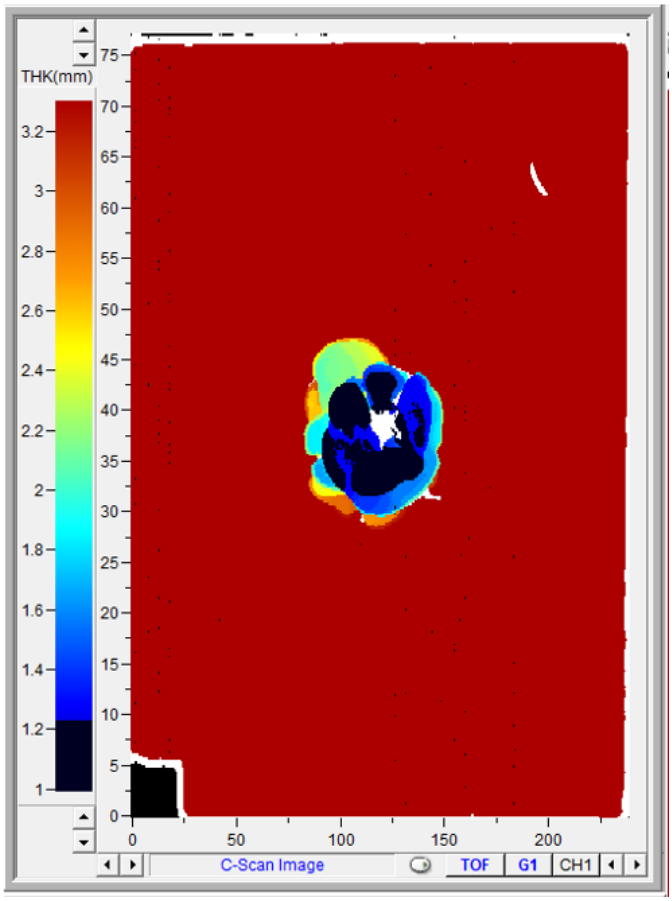
THK(mm)
C-Scan Image
TOF
G1
CH1

Panel S 15 J

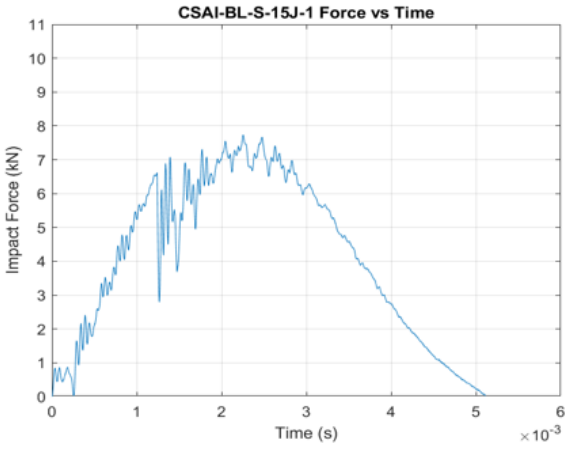
CSAI-BL-S-15J-1 Force vs Time
Impact Force (kN)
Time (s)
×10^-3

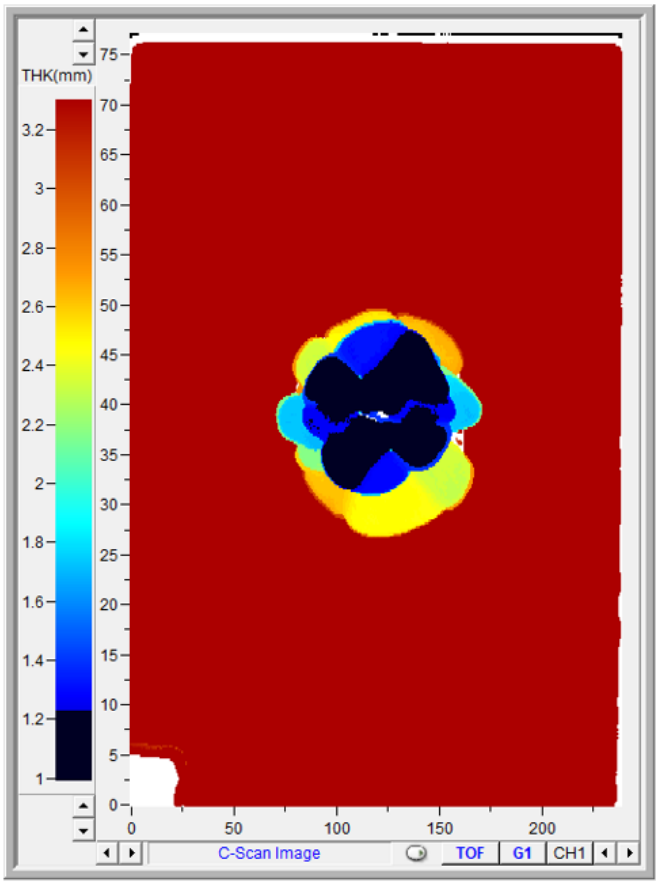
THK(mm)
C-Scan Image
TOF
G1
CH1

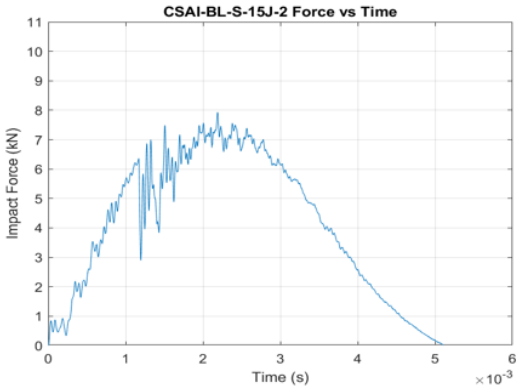

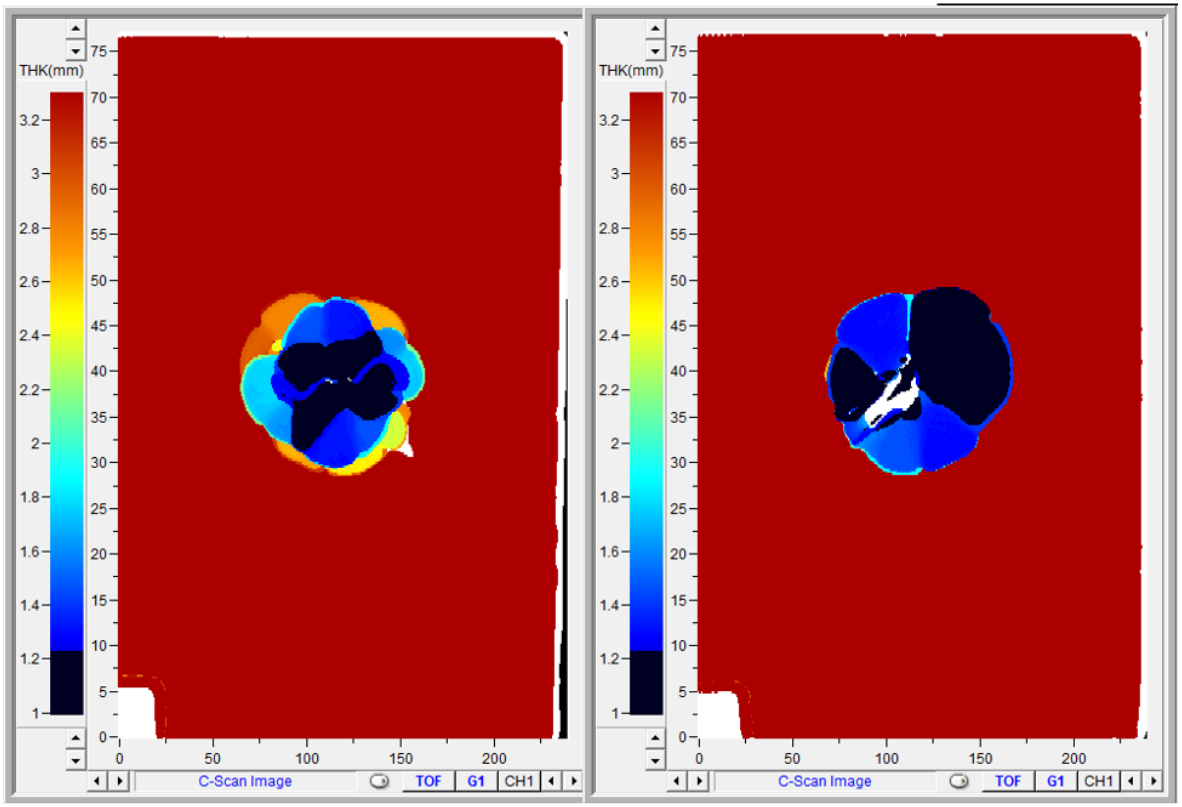

Frontside Backside

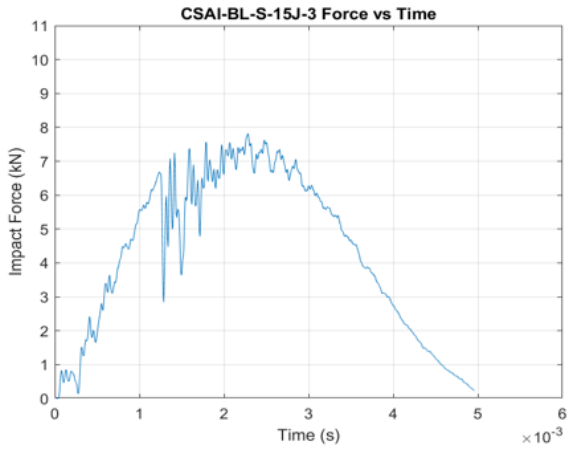
CSAI-BL-S-15J-3 Force vs Time
Impact Force (kN)
Time (s)
×10^-3

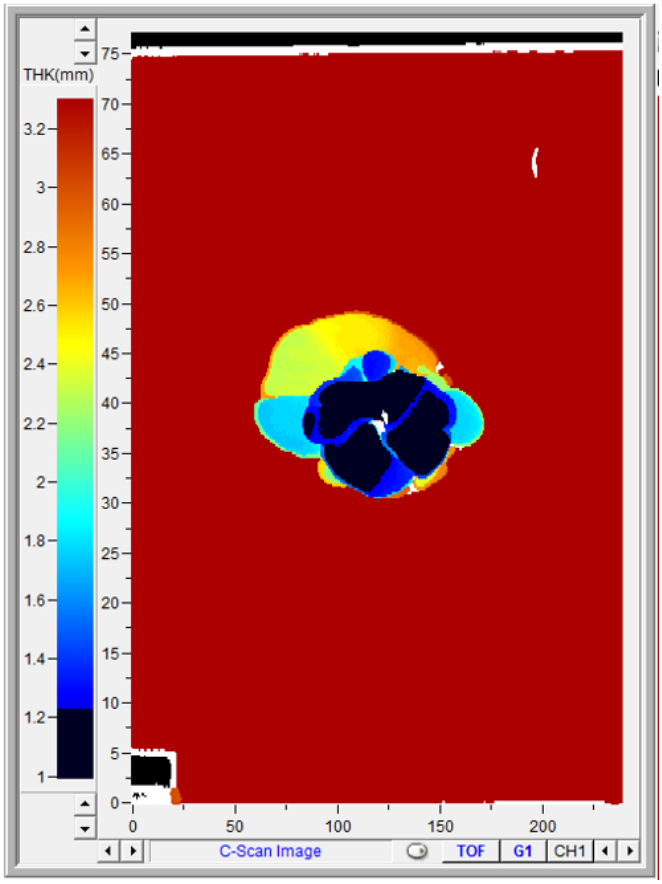
THK(mm)
C-Scan Image
TOF
G1
CH1

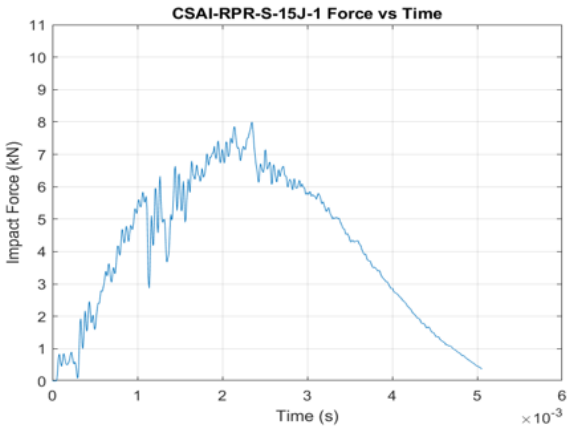
CSAI-RPR-S-15J-1 Force vs Time
Impact Force (kN)
Time (s)
×10^-3

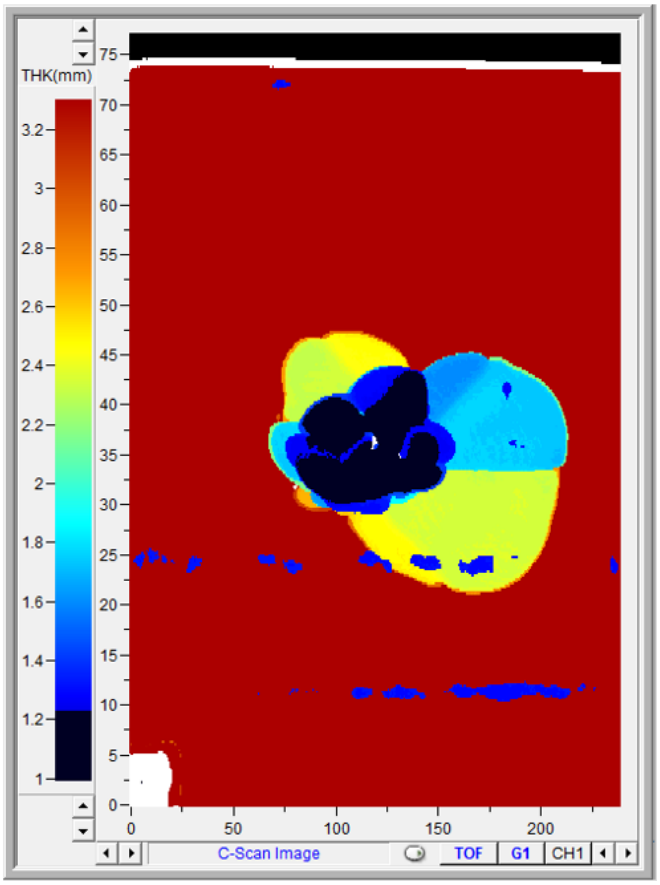
THK(mm)
C-Scan Image
TOF
G1
CH1

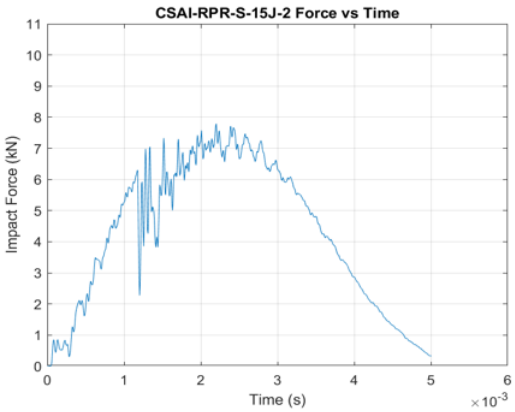

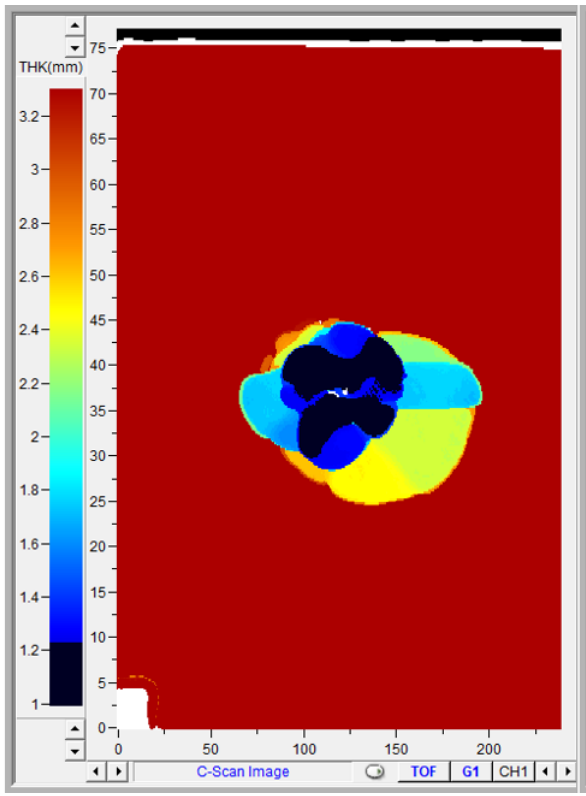

Frontside

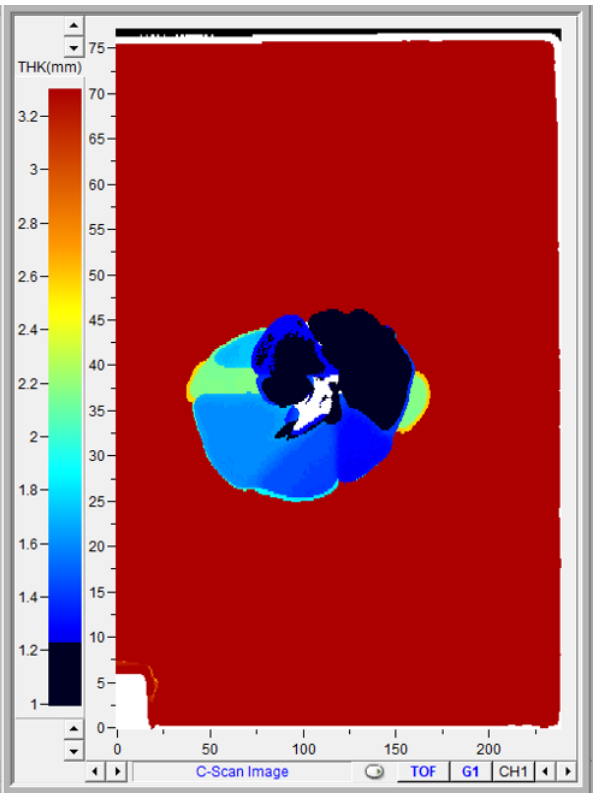

Backside

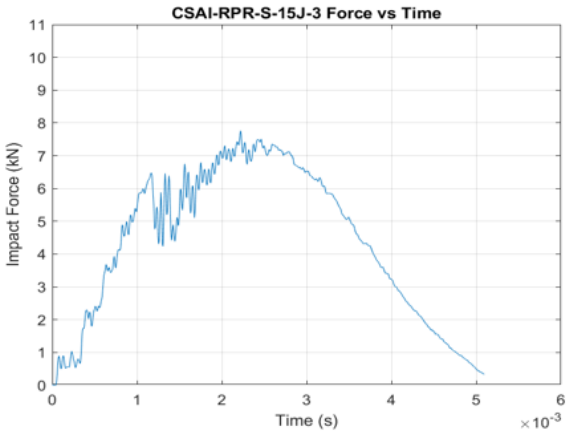
CSAI-RPR-S-15J-3 Force vs Time
Impact Force (kN)
Time (s)
×10^-3

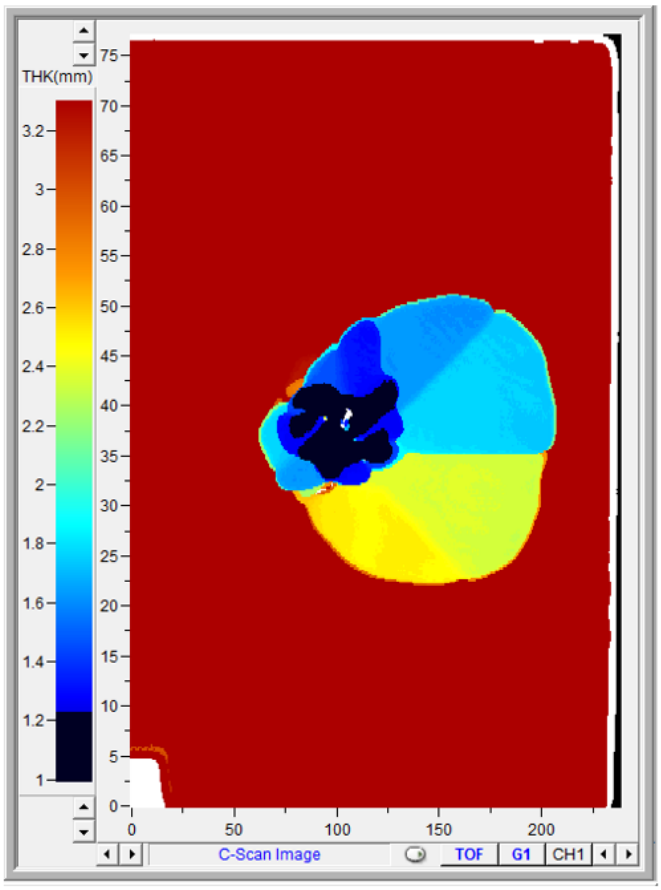
THK(mm)
C-Scan Image
TOF
G1
CH1

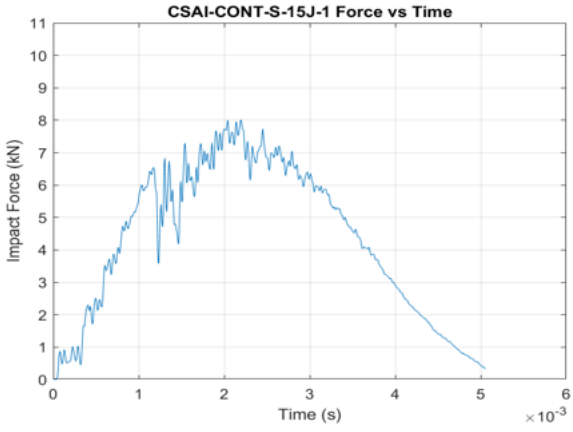
CSAI-CONT-S-15J-1 Force vs Time
Impact Force (kN)
Time (s)
×10^-3

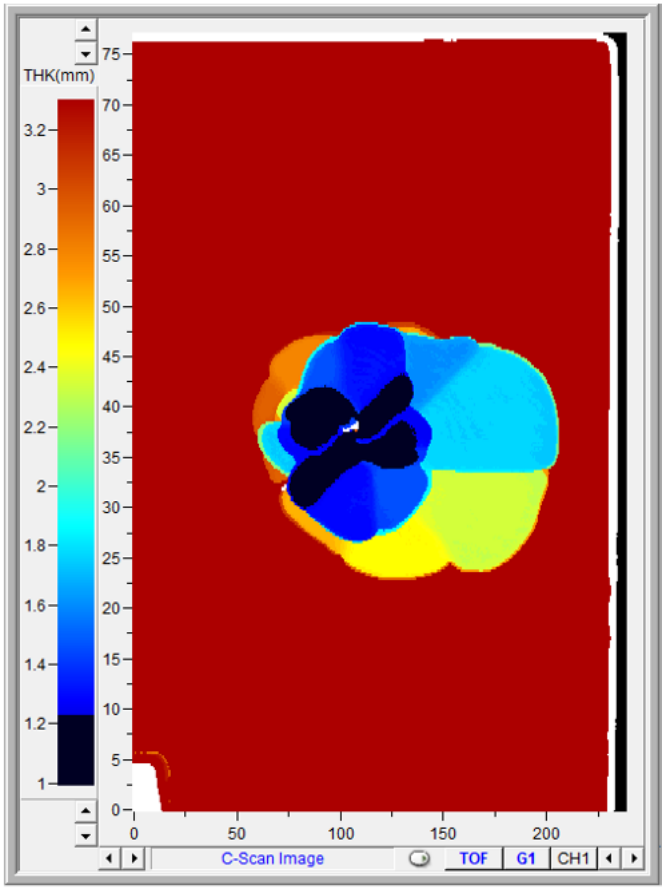
THK(mm)
C-Scan Image
TOF
G1
CH1

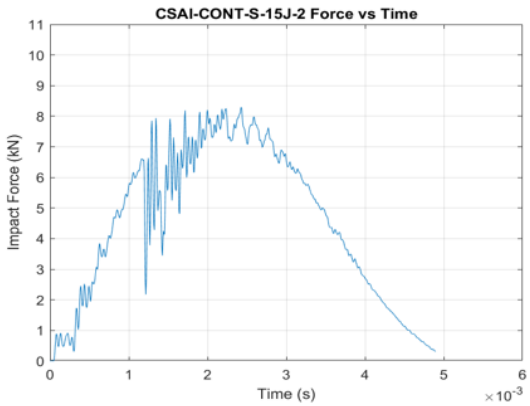

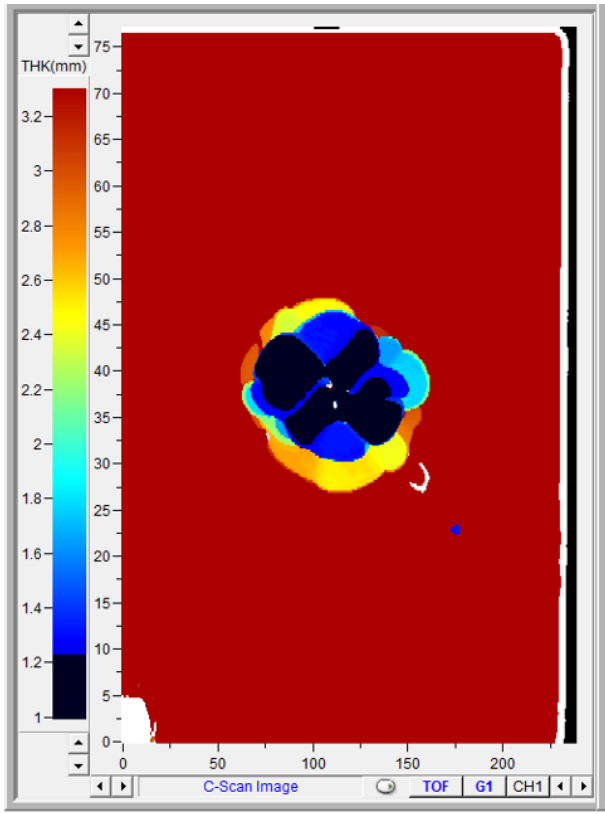

Frontside

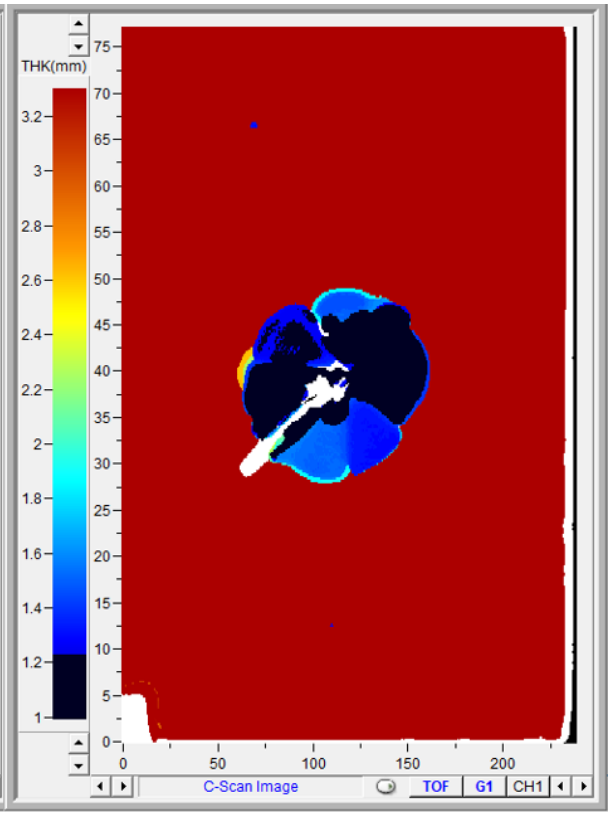

Backside

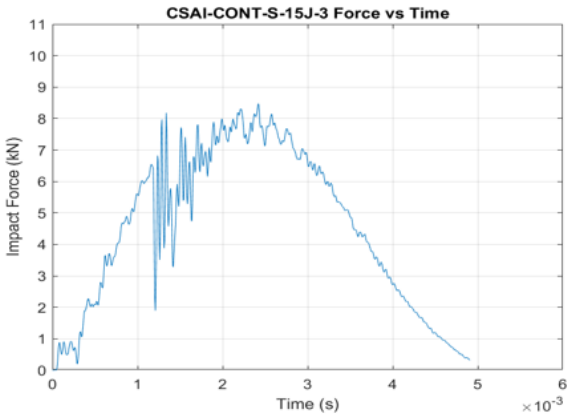
CSAI-CONT-S-15J-3 Force vs Time
Impact Force (kN)
Time (s)
×10^-3

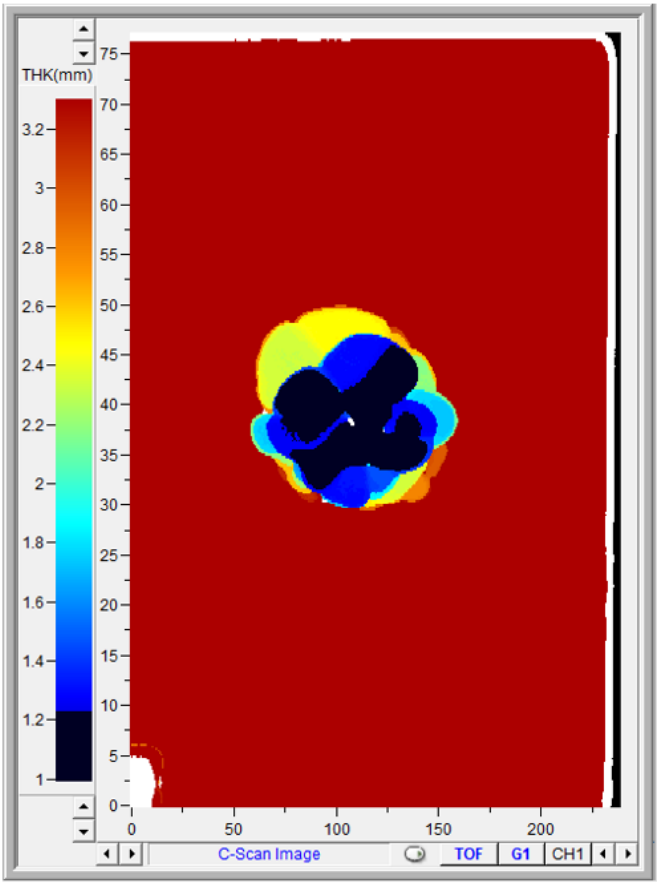
THK(mm)
C-Scan Image
TOF
G1
CH1

Panel H 20 J

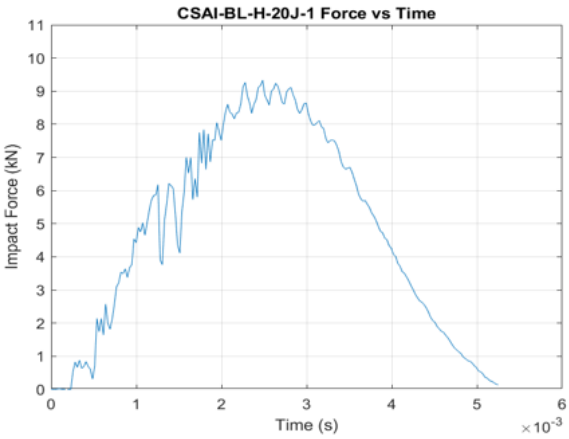
CSAI-BL-H-20J-1 Force vs Time
Impact Force (kN)
Time (s)
×10^-3

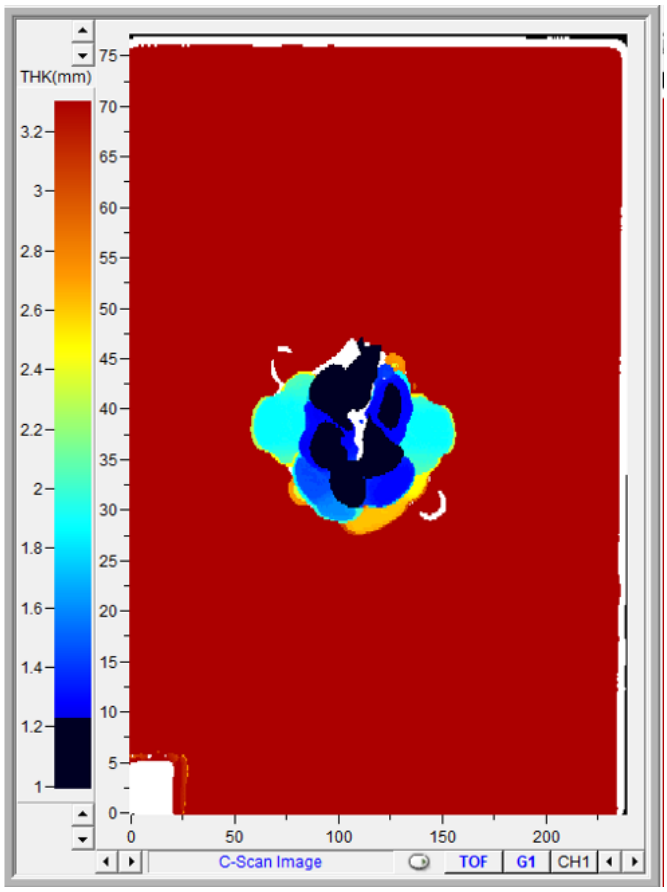
THK(mm)
C-Scan Image
TOF
G1
CH1

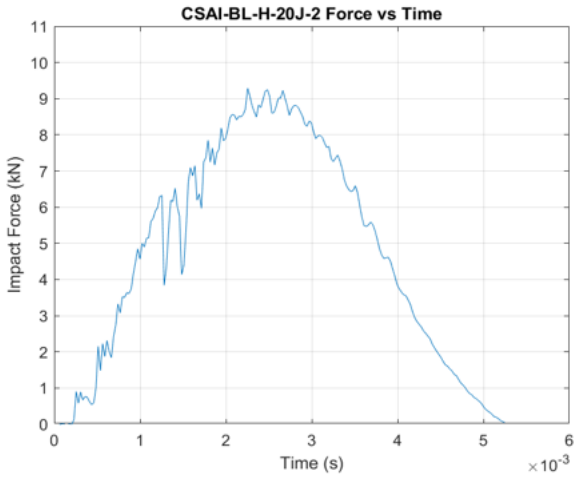
CSAI-BL-H-20J-2 Force vs Time
Impact Force (kN)
Time (s)
×10^-3

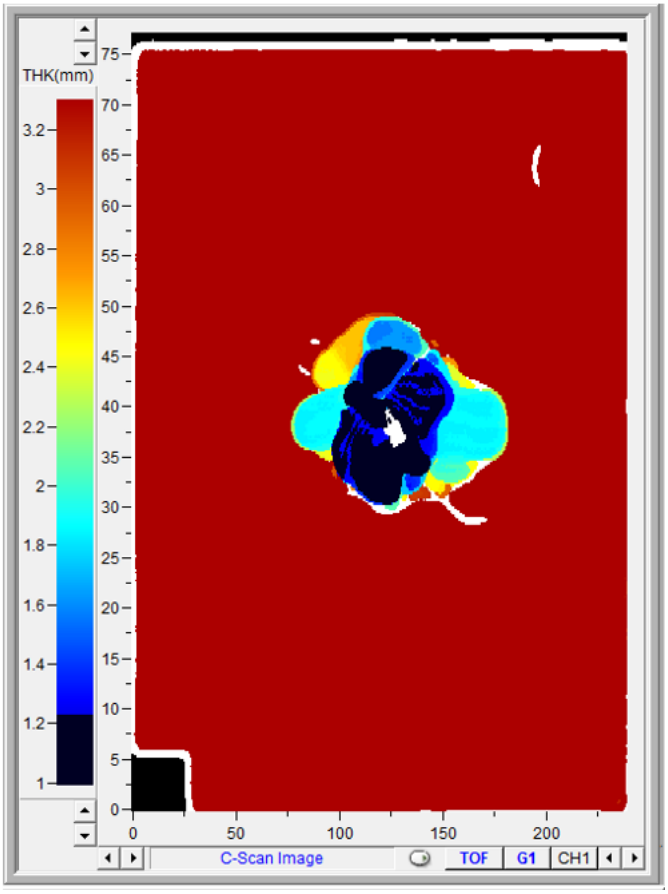
THK(mm)
C-Scan Image
TOF
G1
CH1

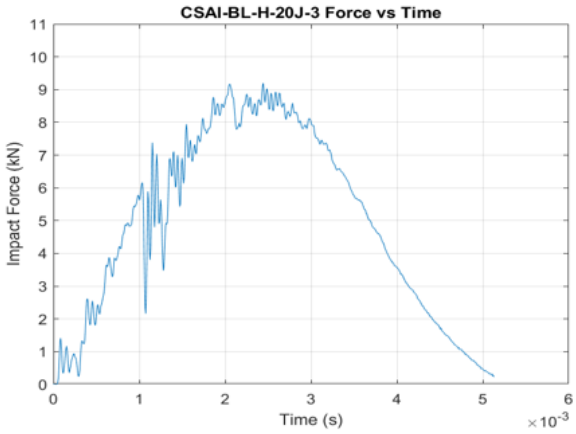
CSAI-BL-H-20J-3 Force vs Time
Impact Force (kN)
Time (s)
×10^-3

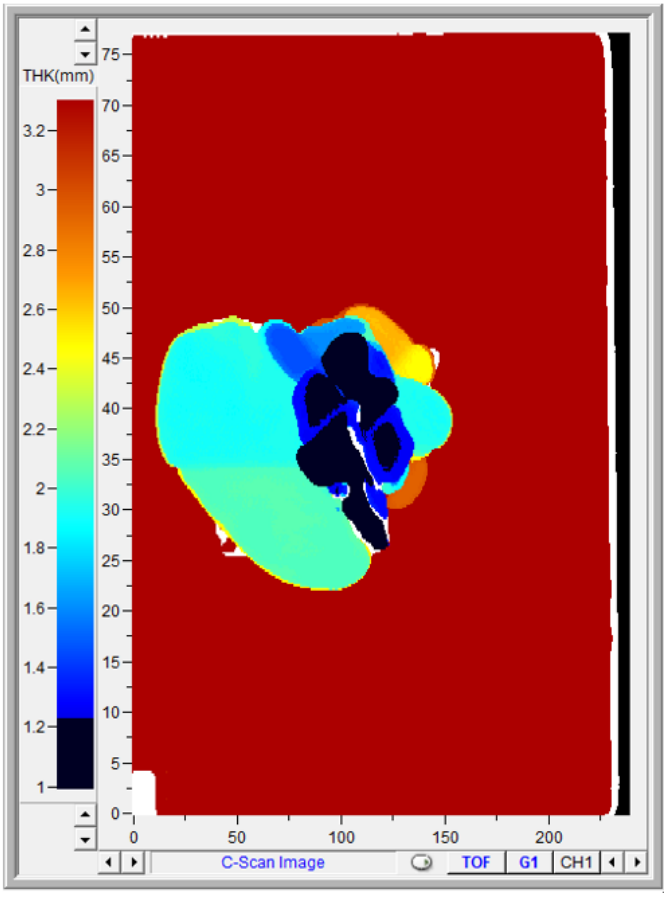
THK(mm)
C-Scan Image
TOF
G1
CH1

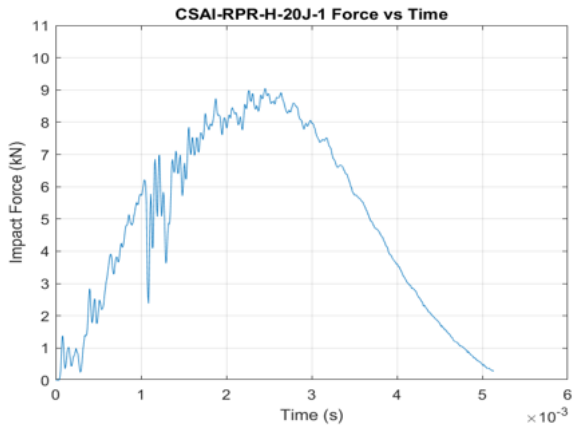
CSAI-RPR-H-20J-1 Force vs Time
Impact Force (kN)
Time (s)
×10^-3

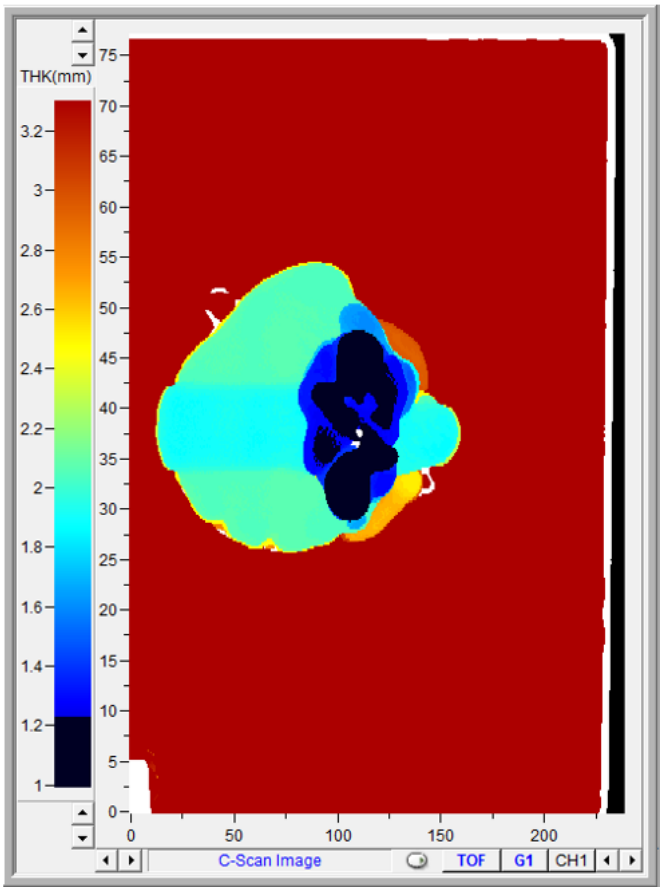
THK(mm)
C-Scan Image
TOF
G1
CH1

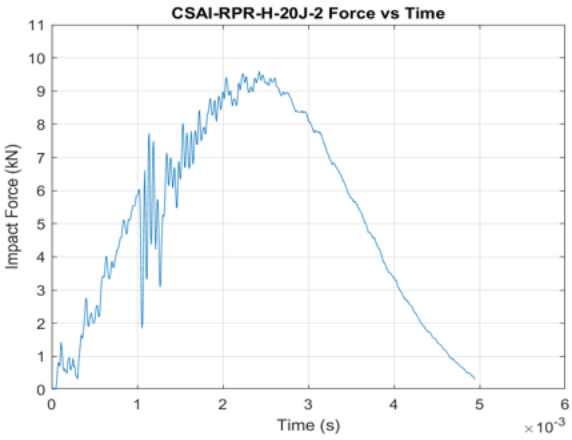
CSAI-RPR-H-20J-2 Force vs Time
Impact Force (kN)
Time (s)
×10^-3

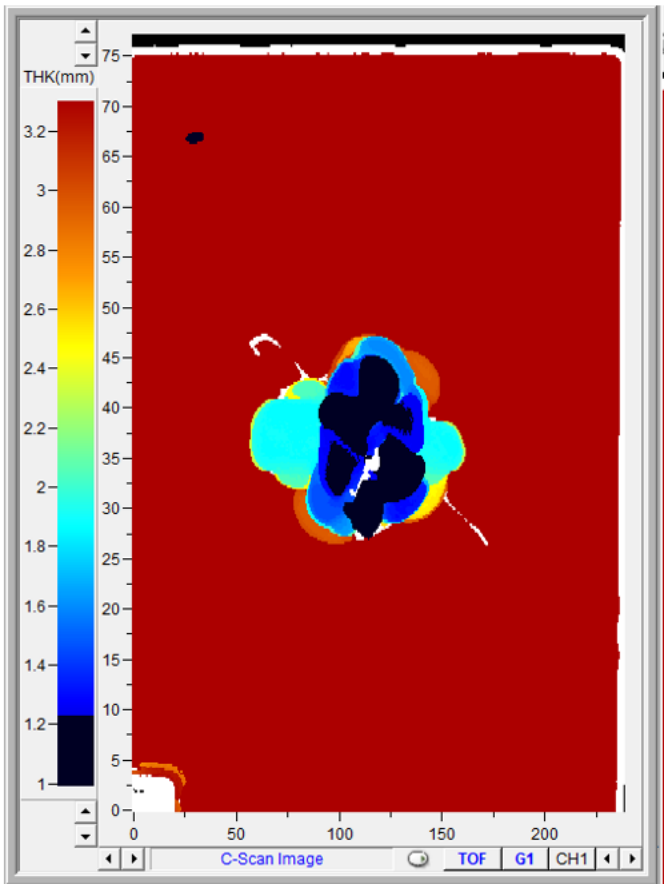
THK(mm)
C-Scan Image
TOF
G1
CH1

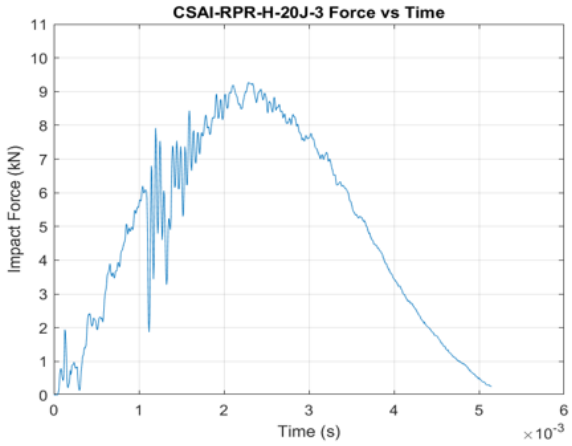
CSAI-RPR-H-20J-3 Force vs Time
Impact Force (kN)
Time (s)
×10^-3

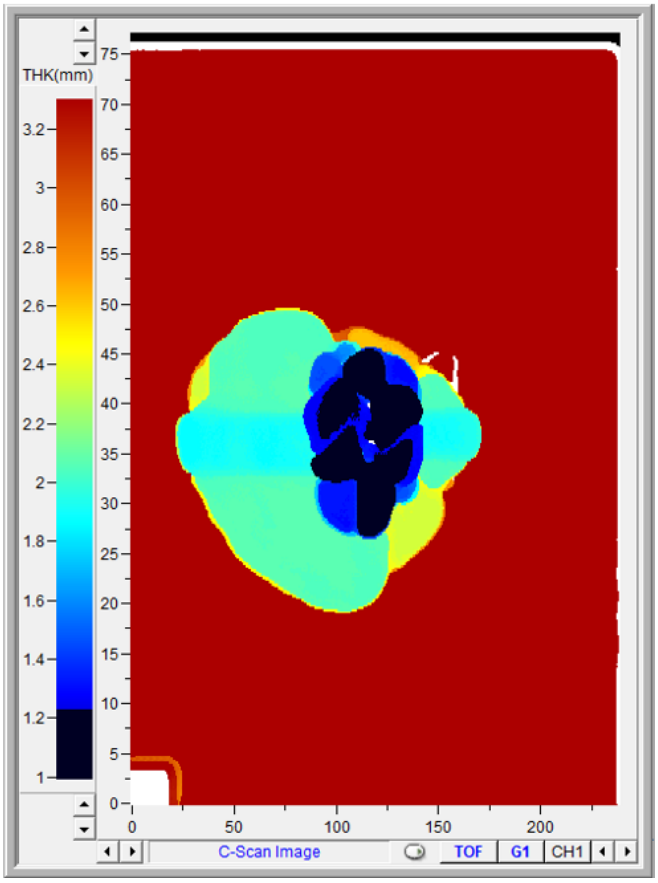
THK(mm)
C-Scan Image
TOF
G1
CH1

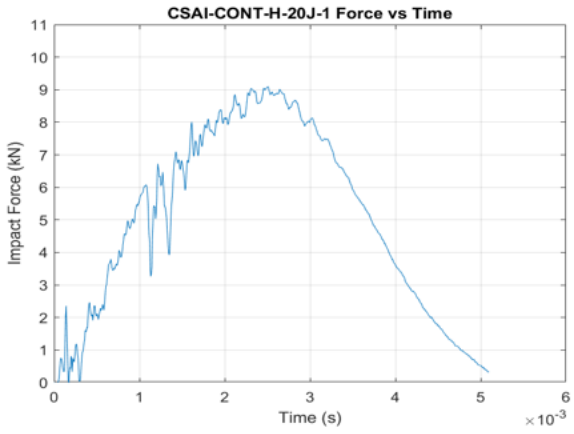
CSAI-CONT-H-20J-1 Force vs Time
Impact Force (kN)
Time (s)
×10^-3

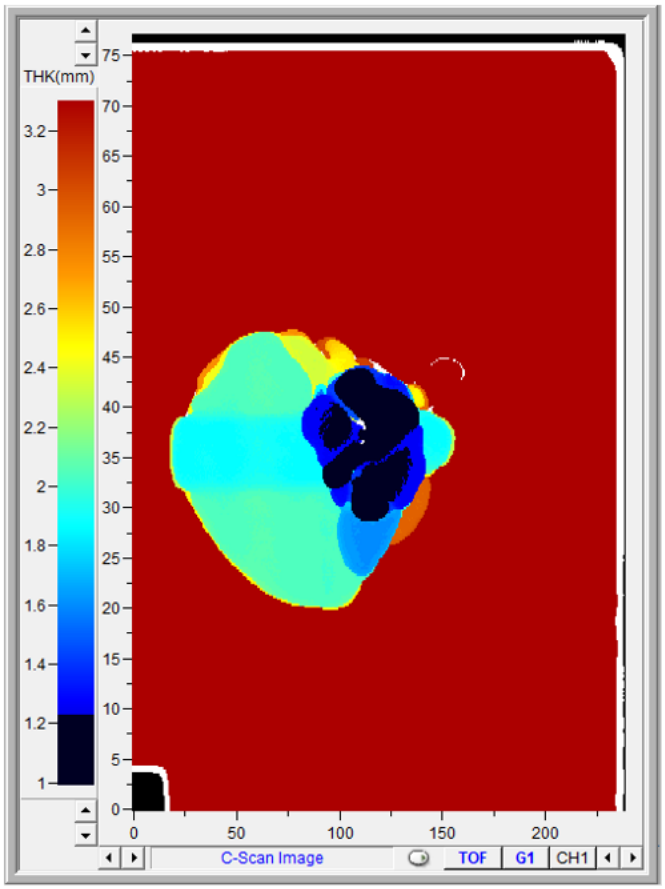
THK(mm)
C-Scan Image
TOF
G1
CH1

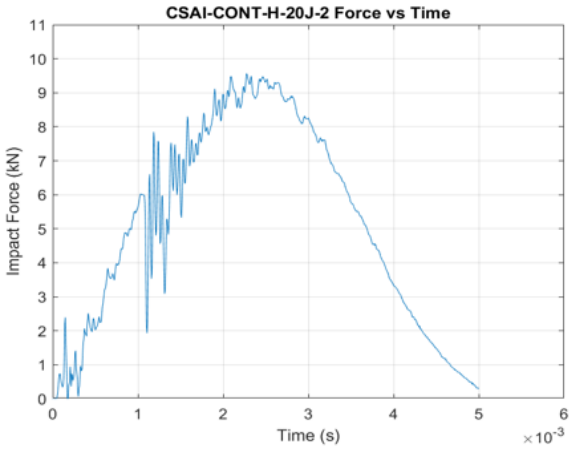
CSAI-CONT-H-20J-2 Force vs Time
Impact Force (kN)
Time (s)
×10^-3

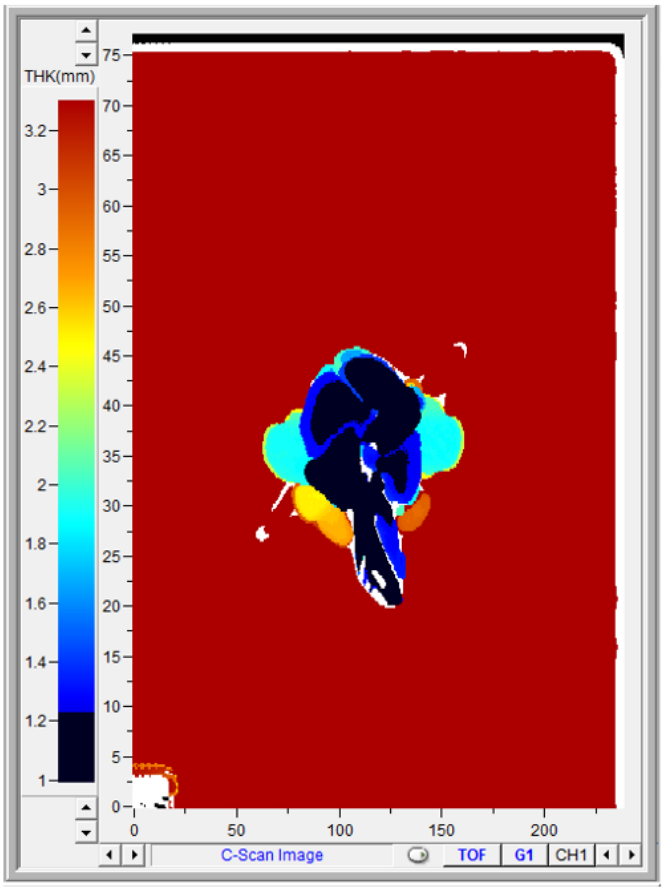
THK(mm)
C-Scan Image
TOF
G1
CH1

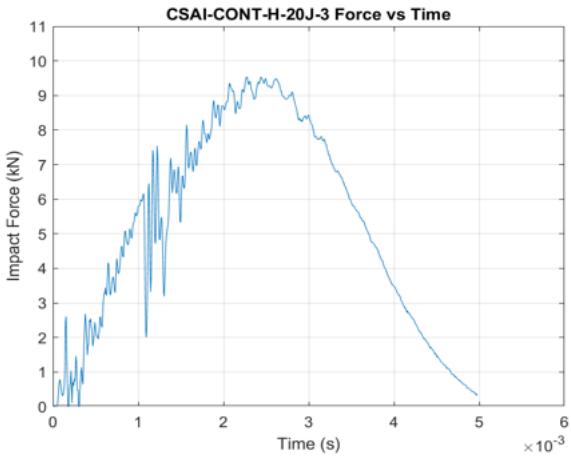
CSAI-CONT-H-20J-3 Force vs Time
Impact Force (kN)
Time (s)
×10^-3

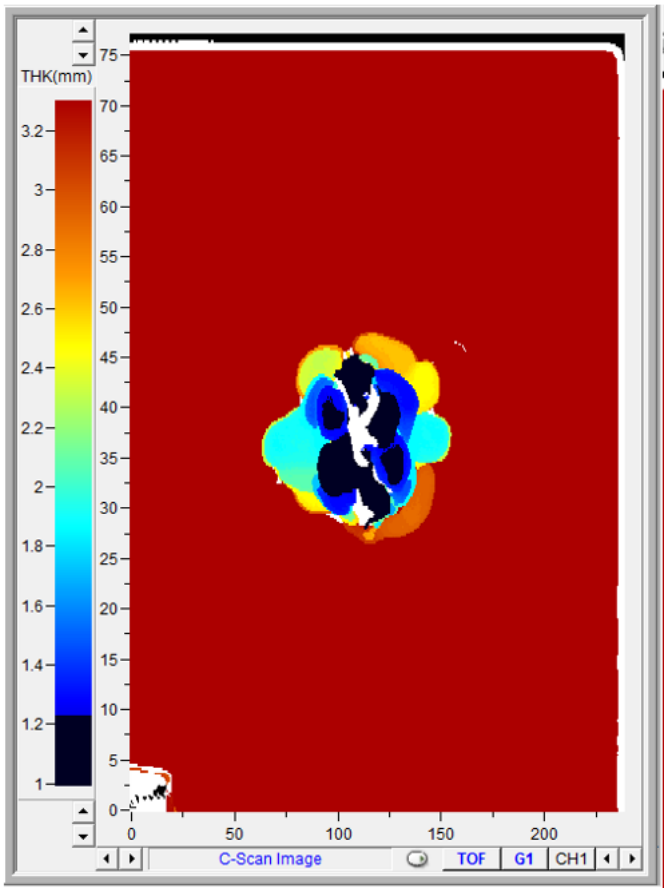
THK(mm)
C-Scan Image
TOF
G1
CH1

Panel M 20 J

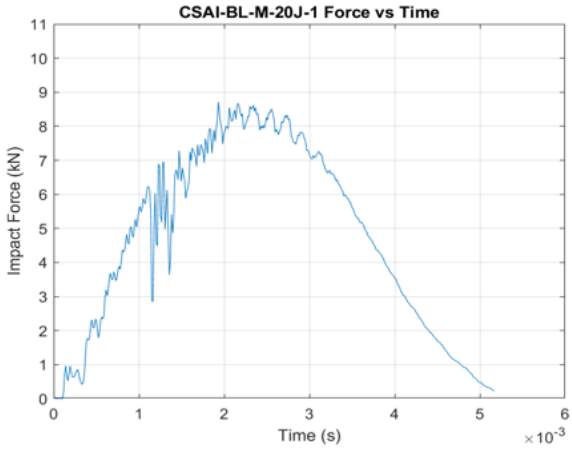
CSAI-BL-M-20J-1 Force vs Time
Impact Force (kN)
Time (s)
×10^-3

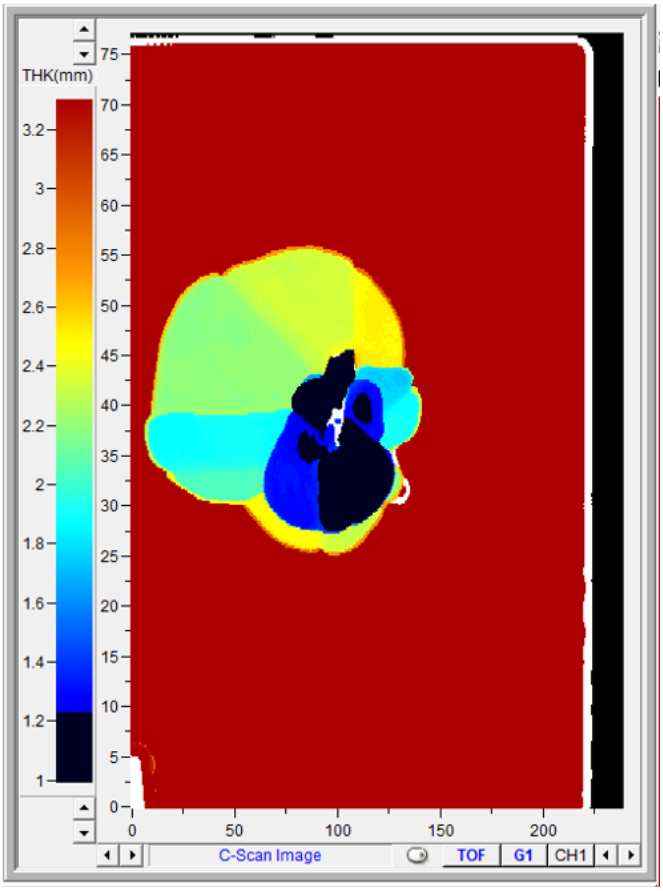
THK(mm)
C-Scan Image
TOF
G1
CH1

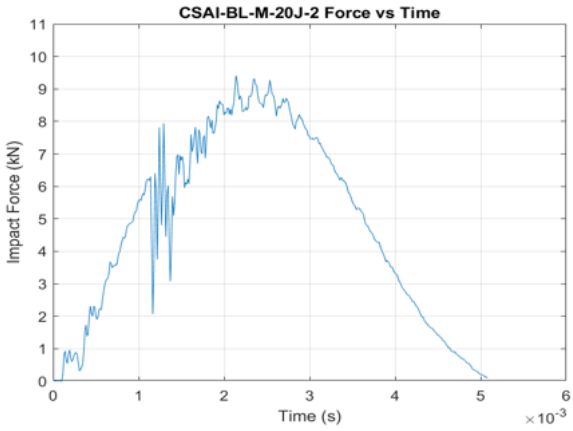
CSAI-BL-M-20J-2 Force vs Time
Impact Force (kN)
Time (s)
×10^-3

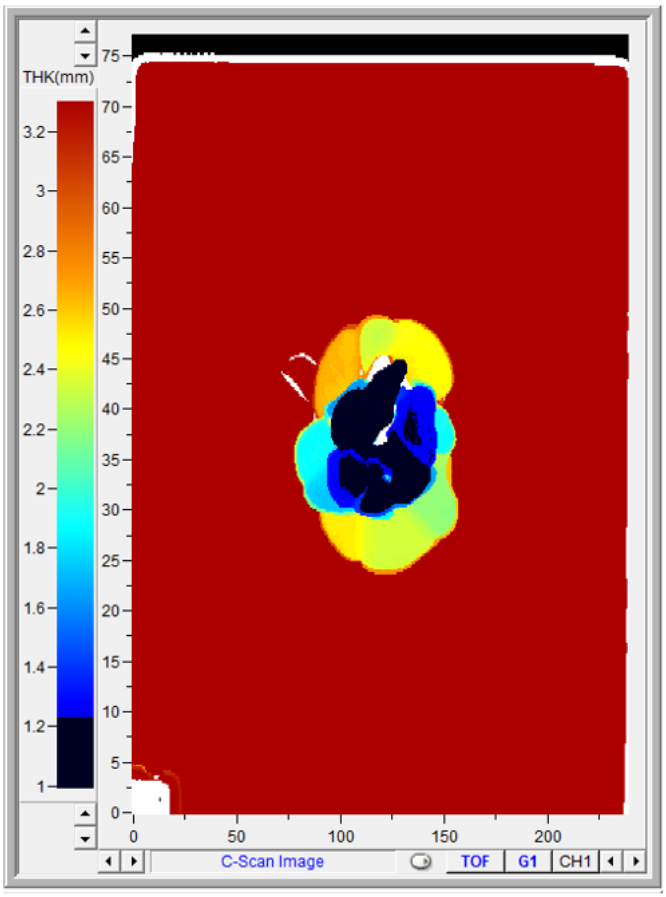
THK(mm)
C-Scan Image
TOF
G1
CH1

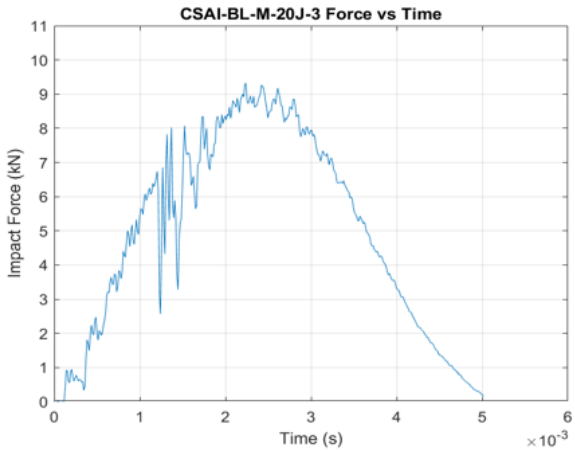
CSAI-BL-M-20J-3 Force vs Time
Impact Force (kN)
Time (s)
×10-3

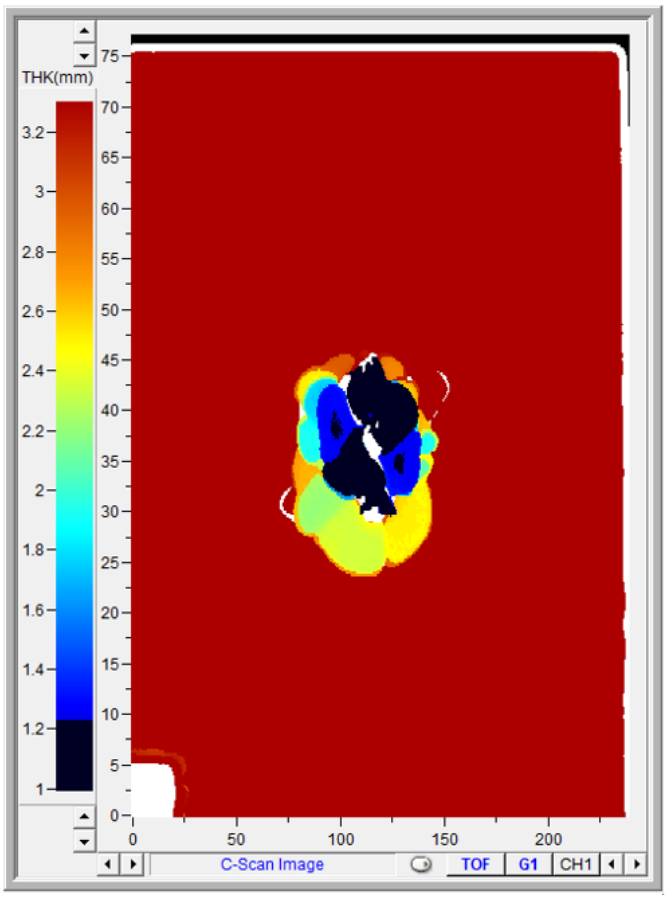
THK(mm)
C-Scan Image
TOF
G1
CH1

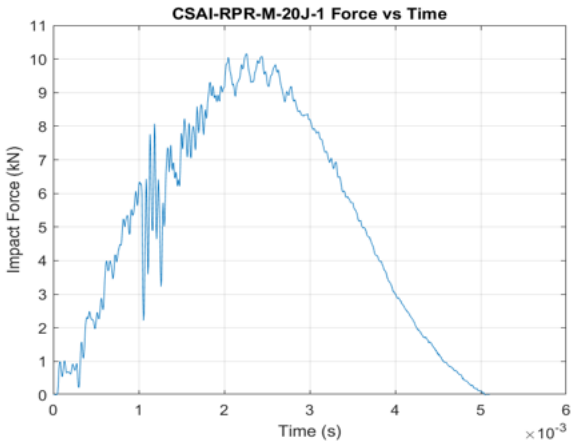
CSAI-RPR-M-20J-1 Force vs Time
Impact Force (kN)
Time (s)
×10^-3

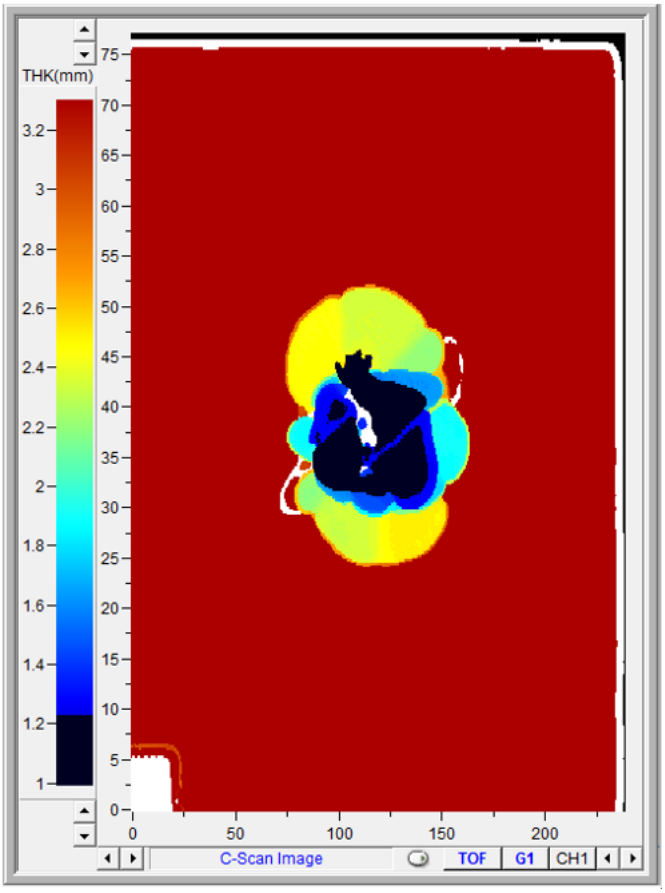
THK(mm)
C-Scan Image
TOF
G1
CH1

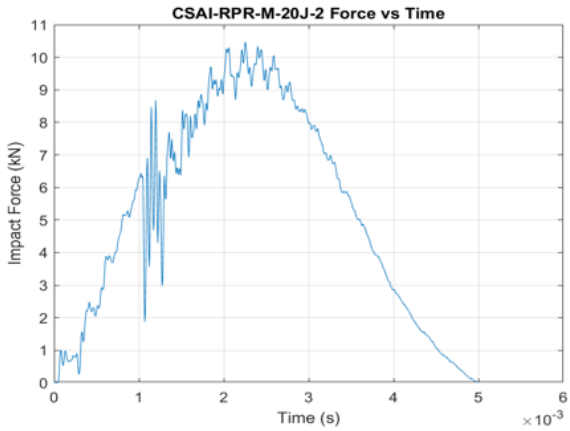
CSAI-RPR-M-20J-2 Force vs Time
Impact Force (kN)
Time (s)
×10^-3

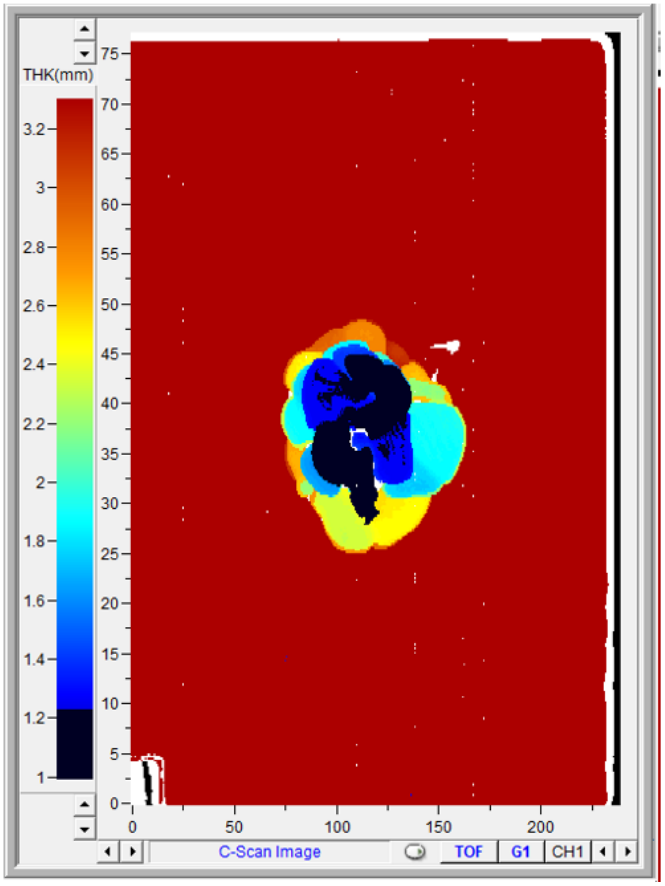
THK(mm)
C-Scan Image
TOF
G1
CH1

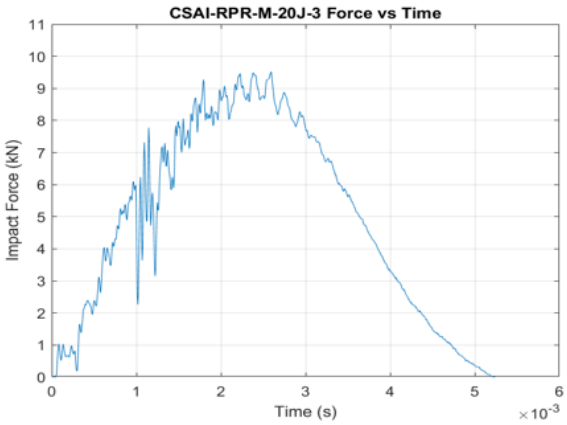
CSAI-RPR-M-20J-3 Force vs Time
Impact Force (kN)
Time (s)
×10^-3

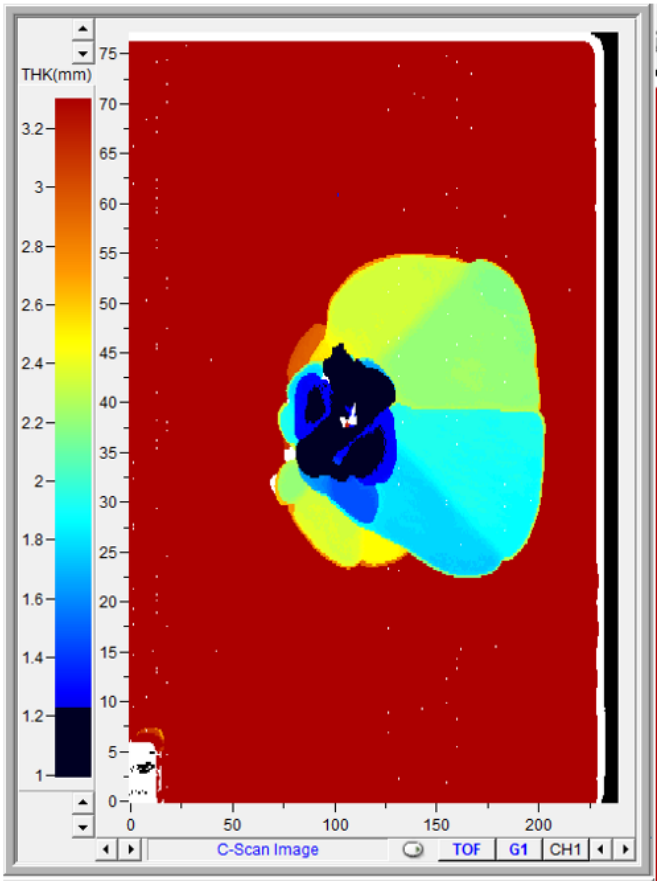
THK(mm)
C-Scan Image
TOF
G1
CH1

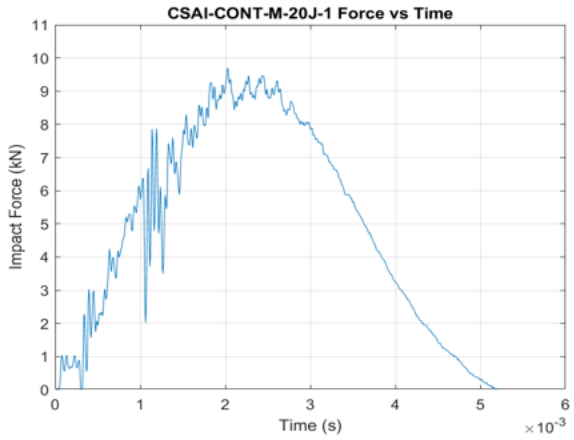
CSAI-CONT-M-20J-1 Force vs Time
Impact Force (kN)
Time (s)
×10-3

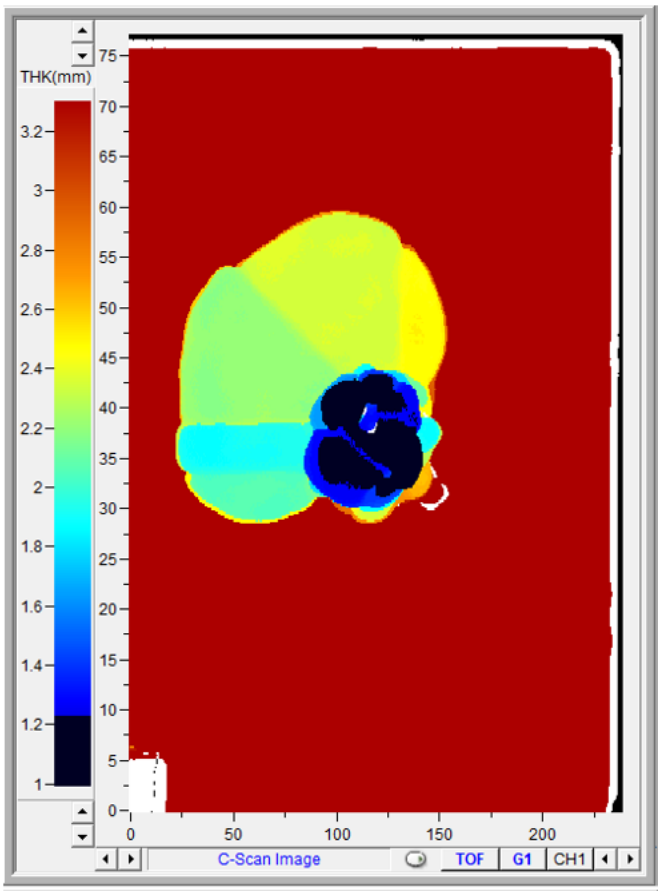
THK(mm)
C-Scan Image
TOF
G1
CH1

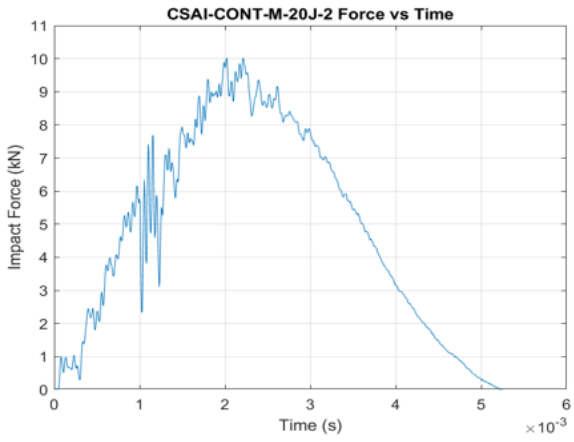
CSAI-CONT-M-20J-2 Force vs Time
Impact Force (kN)
Time (s)
×10-3

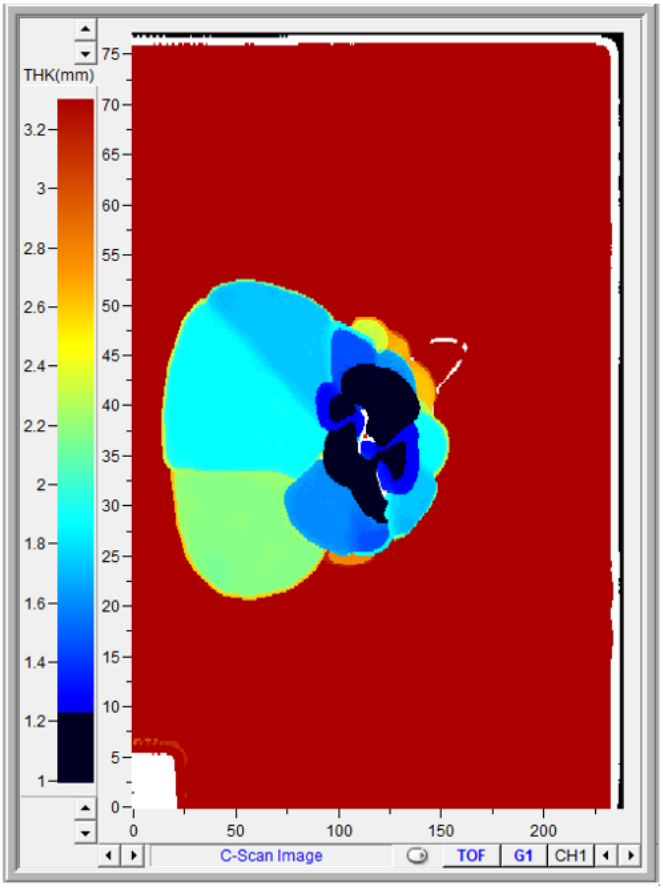
THK(mm)
C-Scan Image
TOF
G1
CH1

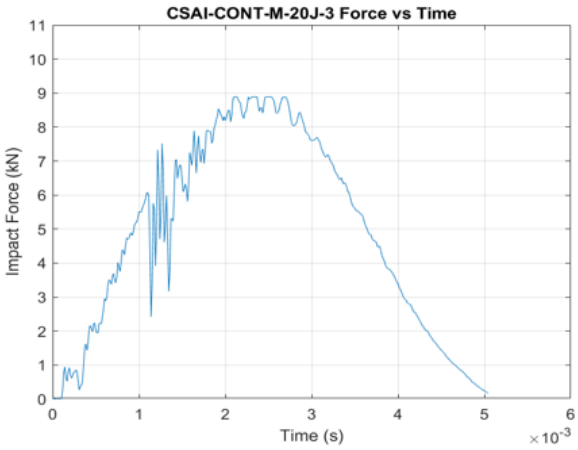
CSAI-CONT-M-20J-3 Force vs Time
Impact Force (kN)
Time (s)
×10^-3

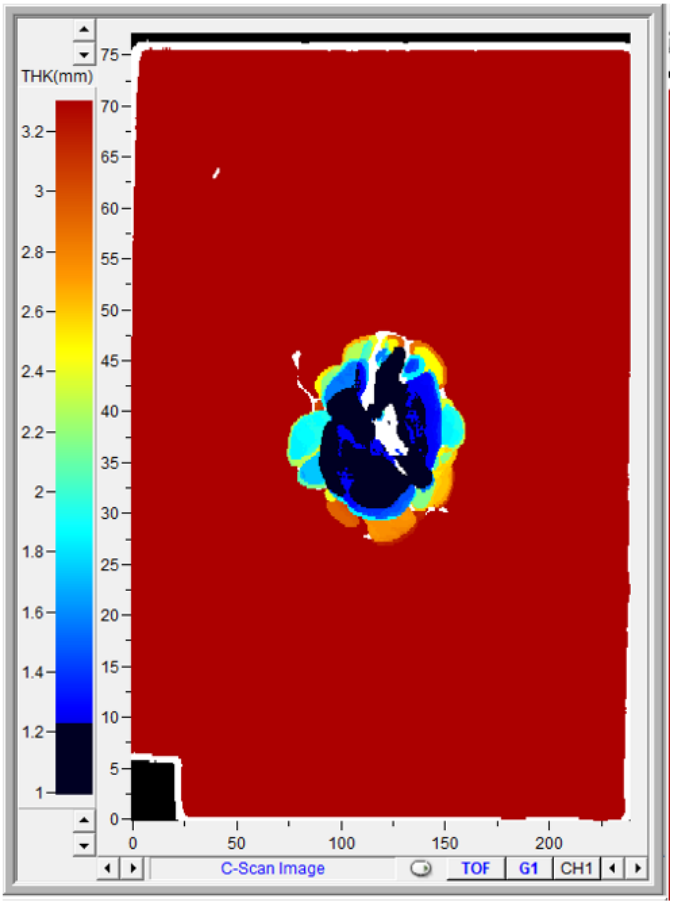
THK(mm)
C-Scan Image
TOF
G1
CH1

Panel S 20 J

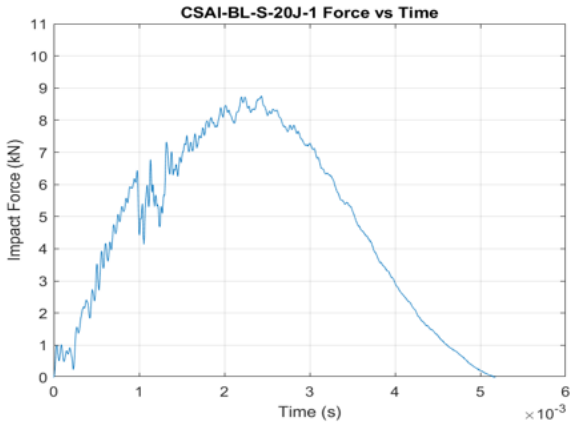
CSAI-BL-S-20J-1 Force vs Time
Impact Force (kN)
Time (s)
×10^-3

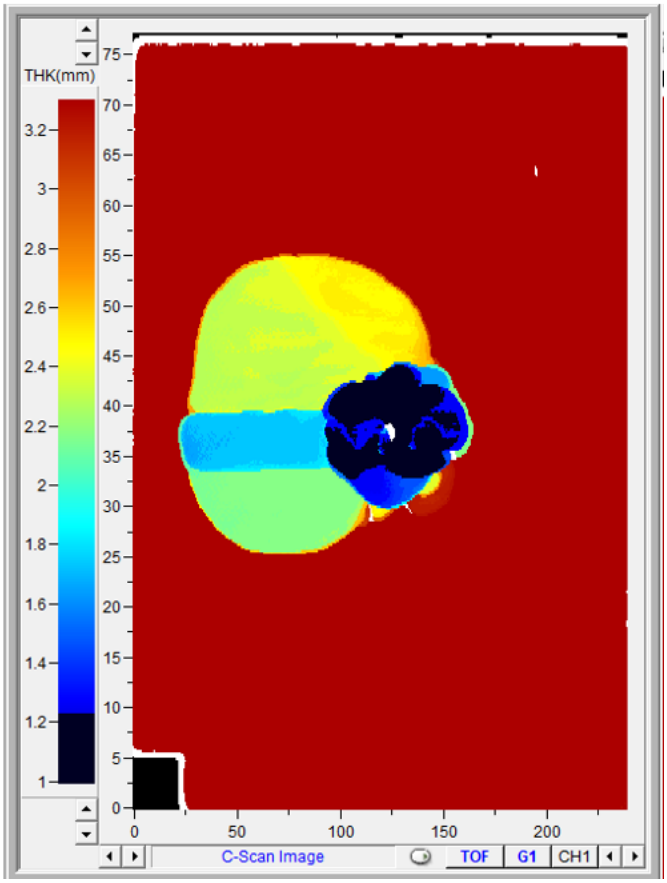
THK(mm)
C-Scan Image
TOF
G1
CH1

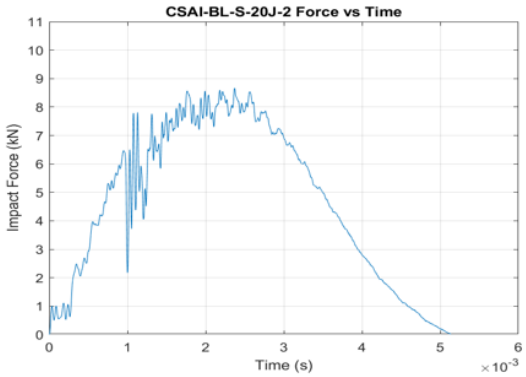

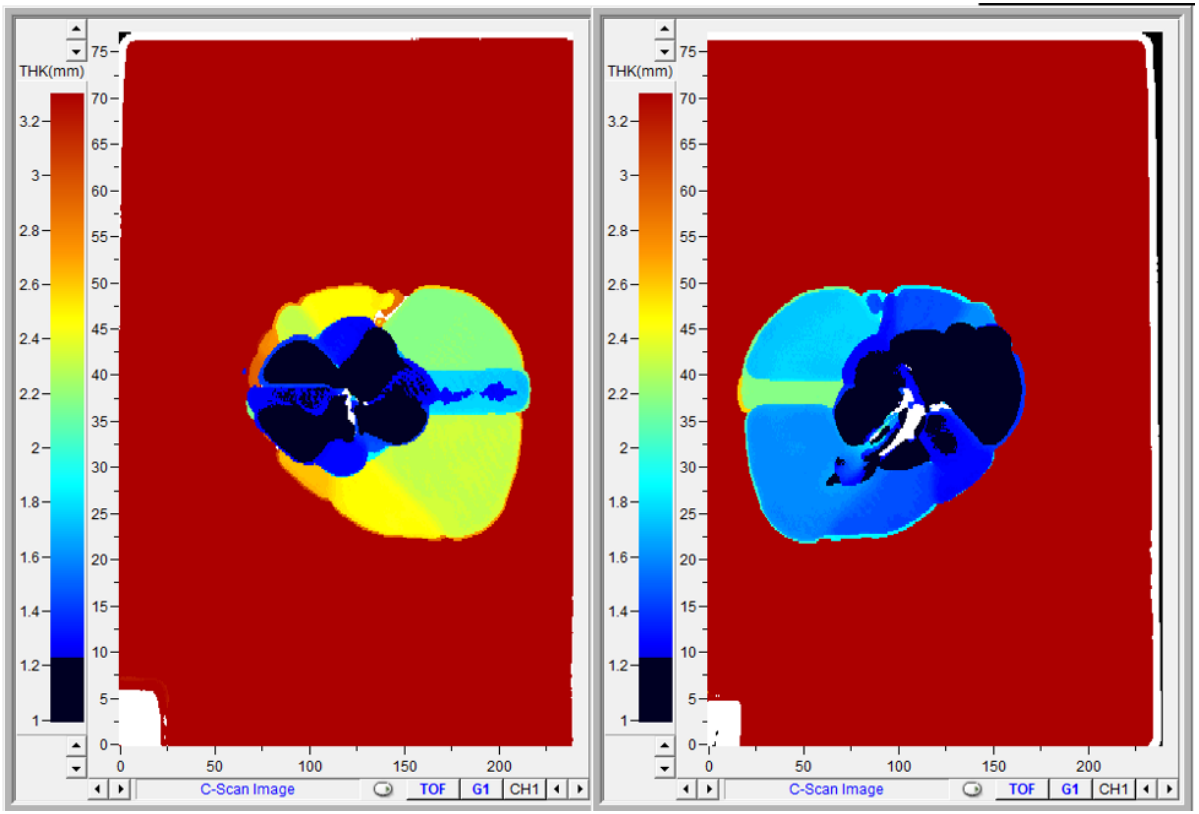

Frontside Backside

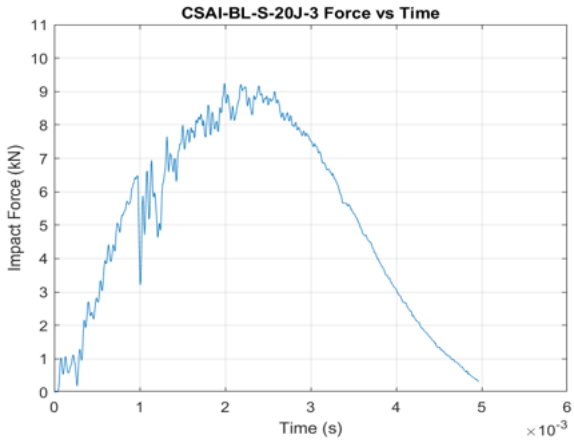
CSAI-BL-S-20J-3 Force vs Time
Impact Force (kN)
Time (s)
×10-3

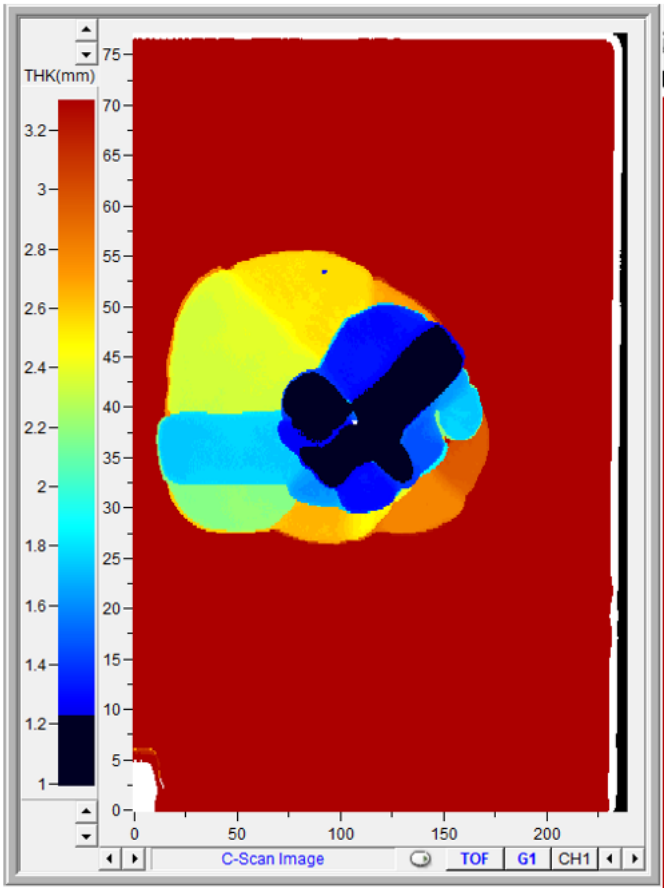
THK(mm)
C-Scan Image
TOF
G1
CH1

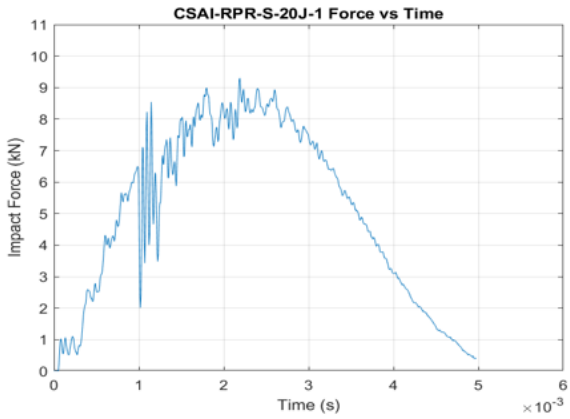
CSAI-RPR-S-20J-1 Force vs Time
Impact Force (kN)
Time (s)
×10^-3

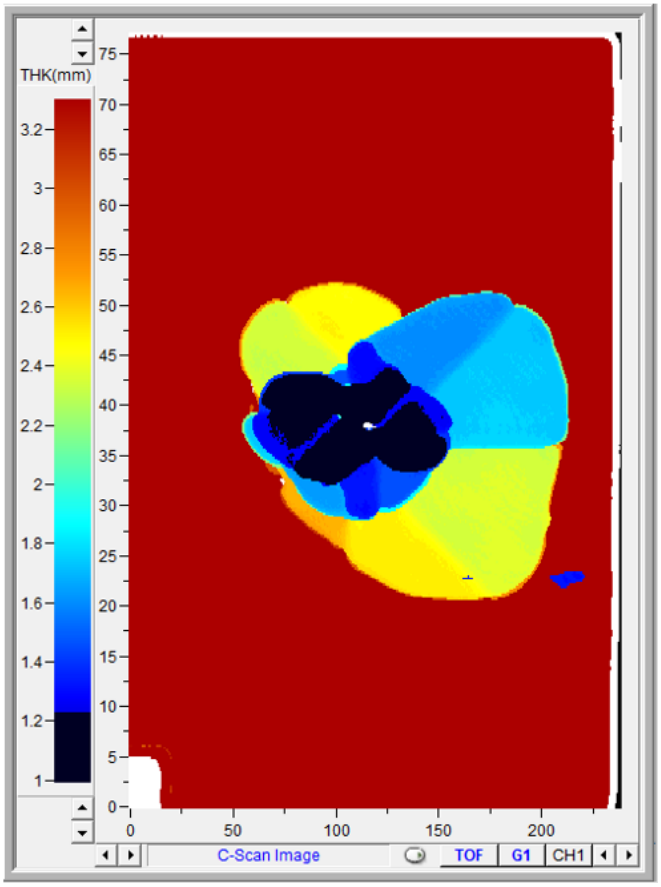
THK(mm)
C-Scan Image
TOF
G1
CH1

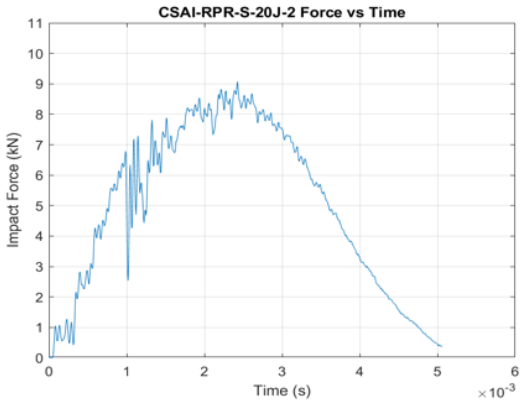

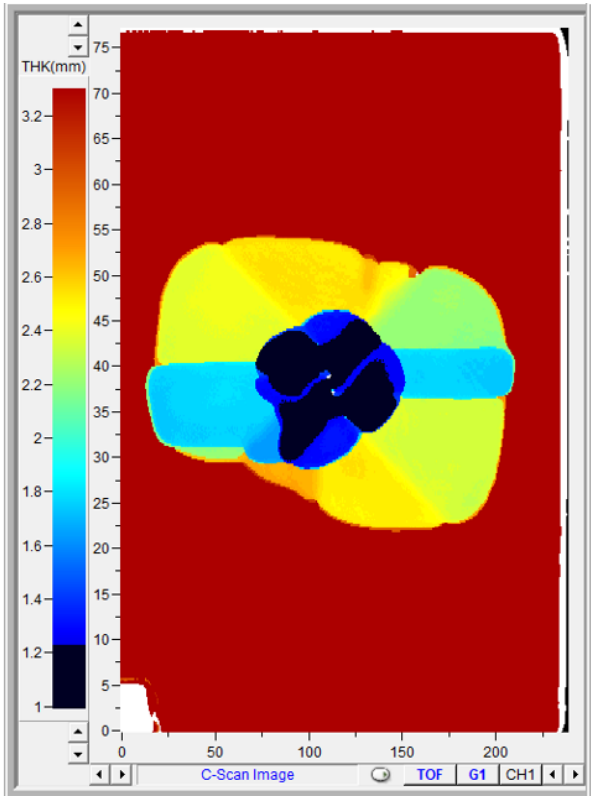

Frontside

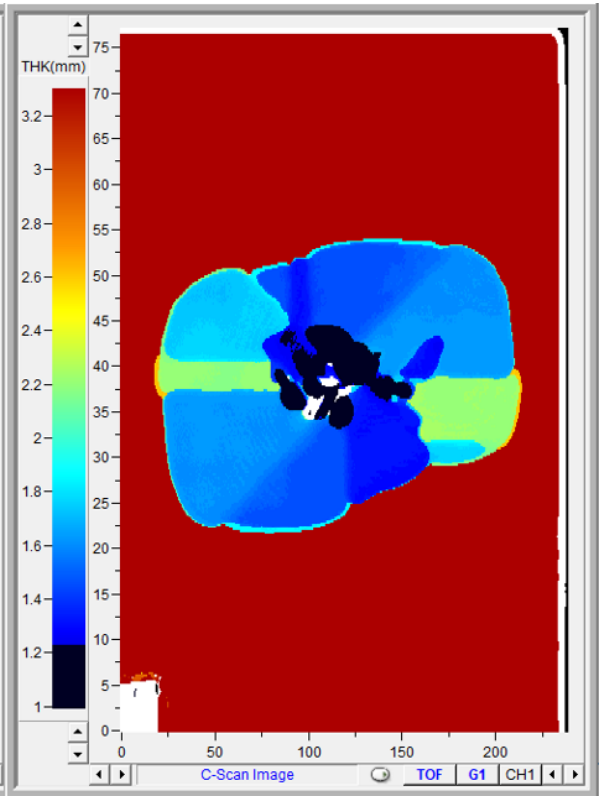

Backside

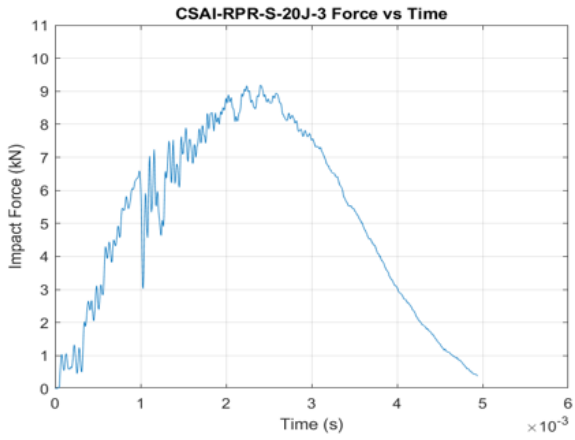
CSAI-RPR-S-20J-3 Force vs Time
Impact Force (kN)
Time (s)
×10^-3

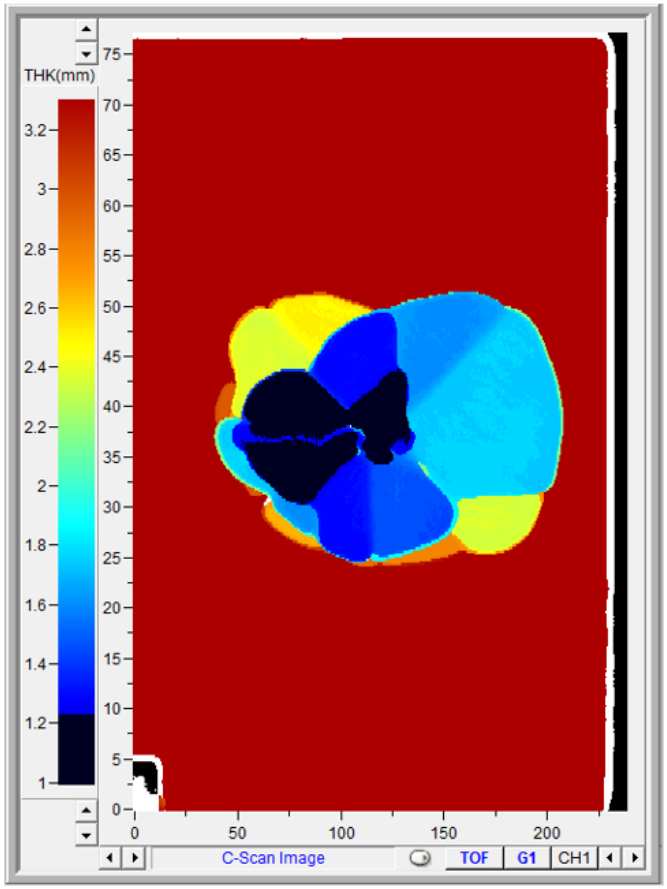
THK(mm)
C-Scan Image
TOF
G1
CH1

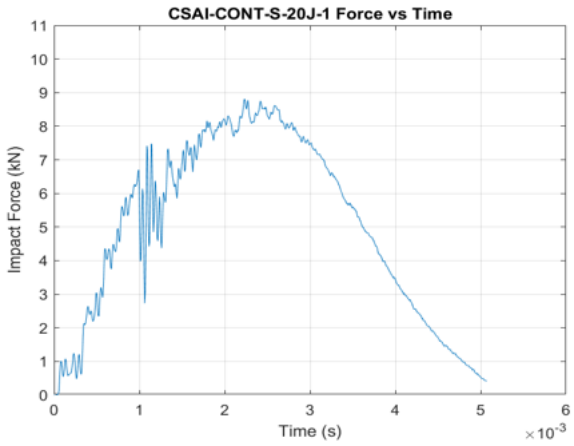
CSAI-CONT-S-20J-1 Force vs Time
Impact Force (kN)
Time (s)
×10^-3

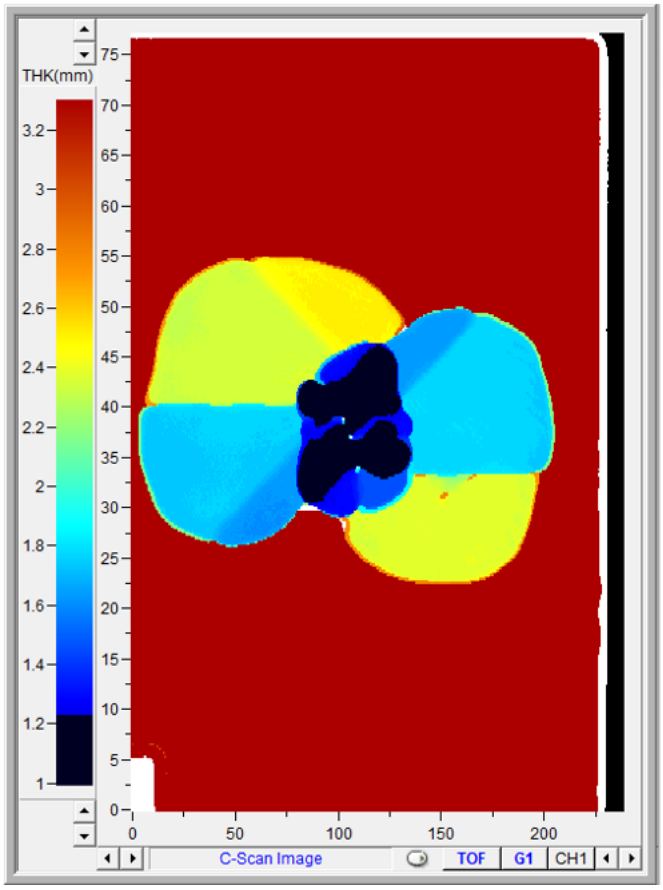
THK(mm)
C-Scan Image
TOF
G1
CH1

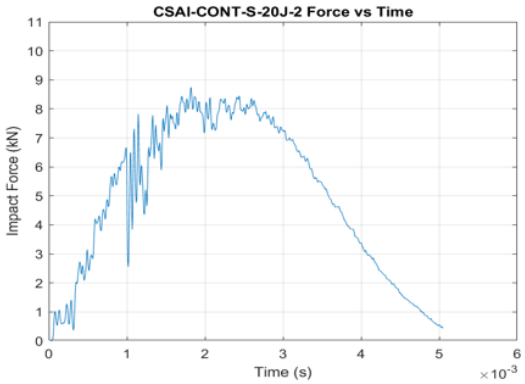

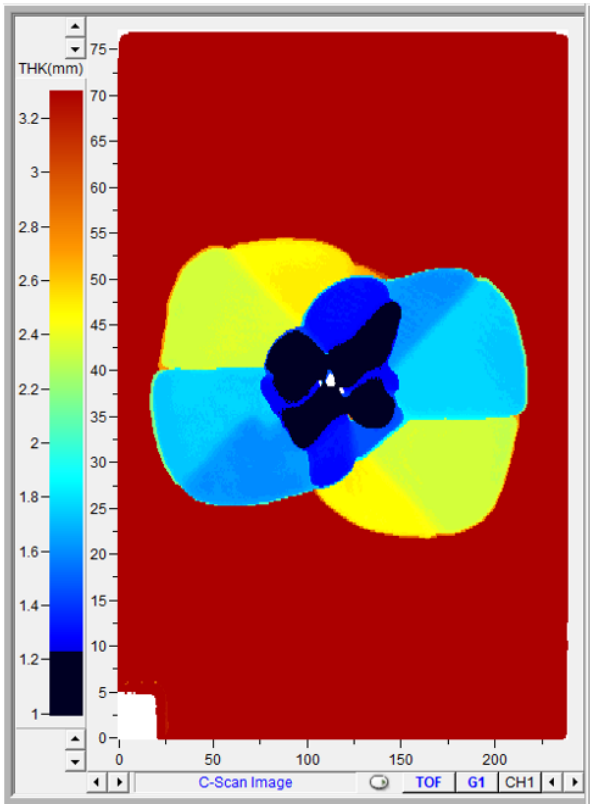

Frontside

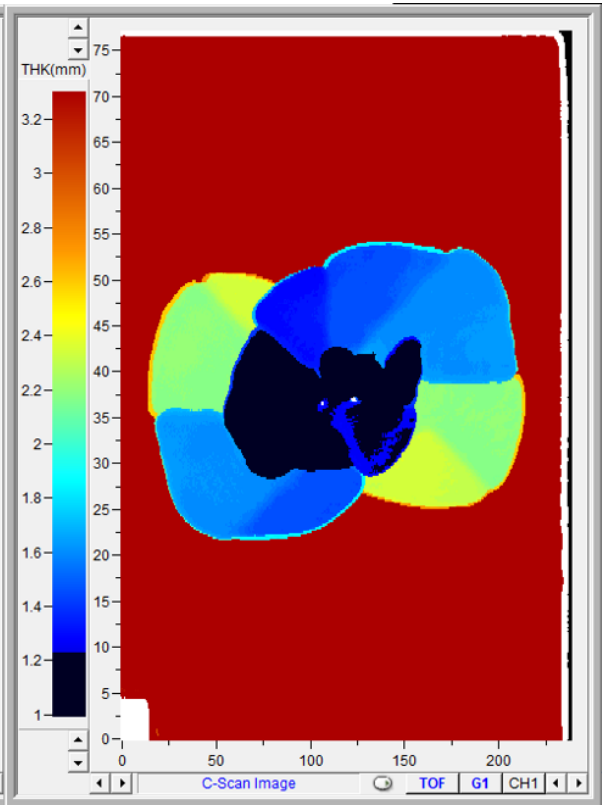

Backside

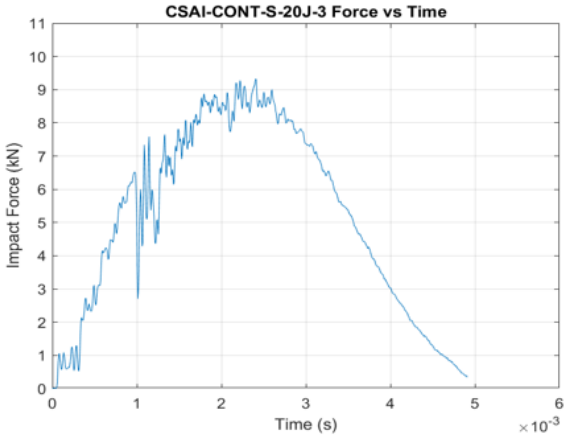
CSAI-CONT-S-20J-3 Force vs Time
Impact Force (kN)
Time (s)
×10^-3

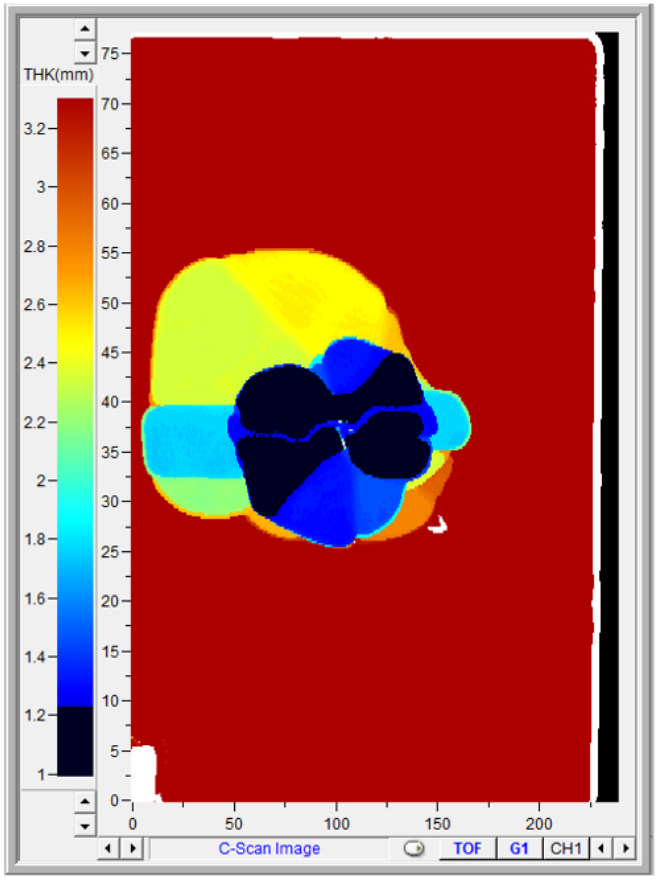
THK(mm)
C-Scan Image
TOF
G1
CH1